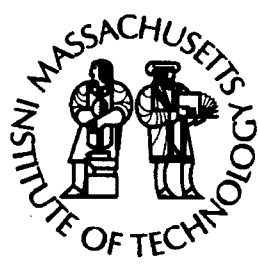
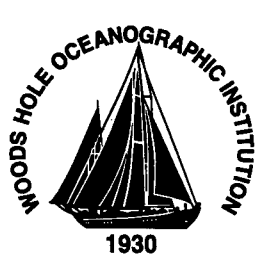


**Massachusetts Institute of Technology  
Woods Hole Oceanographic Institution**



**Joint Program  
in Oceanography/  
Applied Ocean Science  
and Engineering**



---

**DOCTORAL DISSERTATION**

*Tectonic Evolution and Midplate Volcanism  
in the South Pacific*

by

**Kelsey Allyn Jordahl**

**February 1999**

**DISTRIBUTION STATEMENT A**  
Approved for Public Release  
Distribution Unlimited

**20000424 237**

**MIT/WHOI**

**99-01**

**Tectonic Evolution and Midplate Volcanism  
in the South Pacific**

by

Kelsey Allyn Jordahl

Massachusetts Institute of Technology  
Cambridge, Massachusetts 02139

and

Woods Hole Oceanographic Institution  
Woods Hole, Massachusetts 02543

February 1999

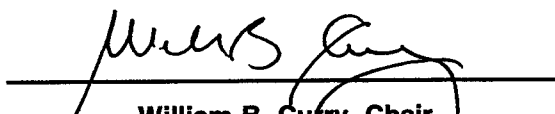
**DOCTORAL DISSERTATION**

Funding was provided by the National Science Foundation under grant numbers  
OCE-9012949, OCE-9012529 and OCE-9415930,

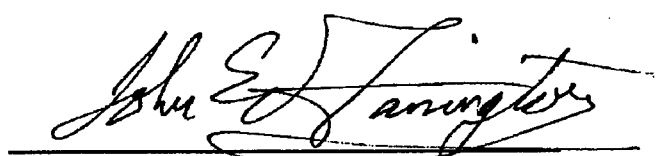
Reproduction in whole or in part is permitted for any purpose of the United States Government. This  
thesis should be cited as: Kelsey Allyn Jordahl, 1999. Tectonic Evolution and Midplate Volcanism in  
the South Pacific. Ph.D. Thesis. MIT/WHOI, 99-01.

Approved for publication; distribution unlimited.

**Approved for Distribution:**

  
\_\_\_\_\_  
**William B. Curry, Chair**  
Department of Geology and Geophysics

  
\_\_\_\_\_  
**Paola Malanotte-Rizzoli**  
MIT Director of Joint Program

  
\_\_\_\_\_  
**John W. Farrington**  
WHOI Dean of Graduate Studies

# Tectonic Evolution and Midplate Volcanism in the South Pacific

by

Kelsey Allyn Jordahl

B.S. Eckerd College, (1992)

Submitted to the Joint Program in Oceanography  
in partial fulfillment of the requirements for the degree of  
Doctor of Philosophy

at the

MASSACHUSETTS INSTITUTE OF TECHNOLOGY

and the

WOODS HOLE OCEANOGRAPHIC INSTITUTION

February 1999

© Kelsey Allyn Jordahl, 1999. All rights reserved.

The author hereby grants to MIT and to WHOI permission to reproduce and  
distribute publicly paper and electronic copies of this thesis document in whole or in  
part, and to grant others the right to do so.

Signature of Author .....

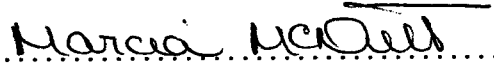


Joint Program in Oceanography

Massachusetts Institute of Technology

Woods Hole Oceanographic Institution

Certified by .....



Marcia McNutt

Thesis Supervisor

Accepted by .....



Deborah Smith

Chair, Joint Committee for Marine Geology and Geophysics

Massachusetts Institute of Technology

Woods Hole Oceanographic Institution

# Tectonic Evolution and Midplate Volcanism in the South Pacific

Kelsey Allyn Jordahl  
MIT/WHOI Joint Program in Oceanography

## Abstract

Changes in morphology of the Marquesas Fracture Zone are correlated with small changes in Pacific-Farallon relative motion. The simple flexural signal of a locked fracture zone may be obscured by tectonic effects, and there is no evidence for the release of shear stress on the fracture zone by vertical slip after leaving the active transform.

One such small change in plate motion is documented in the Southern Austral Island region of the South Pacific. A twelve degree clockwise change in Pacific-Farallon relative motion occurred around fifty million years ago. This Eocene change in spreading direction and rate is locally constrained with observations of magnetic anomalies and spreading fabric orientation.

At the southeastern end of the Cook-Austral Island chain, multiple episodes of volcanism have left a diverse population of seamounts. Volume estimates from geophysical data and modeling show that one-half to two-thirds of the volcanic material is over thirty million years old, while the remainder is less than five million years old.

Seismic and bathymetric data imply the presence of abyssal basalt flows in the flexural moat of the Austral Islands, probably associated with Austral Islands volcanism, which may contribute a significant amount of material to the archipelagic apron.

# **Tectonic Evolution and Midplate Volcanism in the South Pacific**

by

**Kelsey Allyn Jordahl**

Submitted in partial fulfillment of the requirements for the degree of  
Doctor of Philosophy at the Massachusetts Institute of Technology  
and the Woods Hole Oceanographic Institution

## **Abstract**

Changes in morphology of the Marquesas Fracture Zone are correlated with small changes in Pacific-Farallon relative motion. These relative plate motion changes had a strong effect on the active transform that lasted for millions of years. The simple flexural signal of a locked fracture zone may be obscured by tectonic effects, and there is no evidence for the release of shear stress on the fracture zone by vertical slip after leaving the active transform.

One such small change in plate motion is documented in the Southern Austral Island region of the South Pacific. A 12° clockwise change in Pacific-Farallon relative motion occurred around 50 Ma, and was accommodated by a large propagating rift which left an outer pseudofault on the Pacific plate, the 1200 km long Adventure Trough. This Eocene change in spreading direction and rate is locally constrained with observations of magnetic anomalies and spreading fabric orientation.

At the southeastern end of the Cook-Austral Island chain, in the vicinity of the currently active Macdonald Seamount, multiple episodes of volcanism have left a diverse population of seamounts. Multichannel seismic reflection and gravity data in conjunction with three-dimensional flexural modeling provide a more complete view of the volcanic history than radiometric dating and geochemical analysis of sparse dredge samples alone. Volume estimates of the different volcanic episodes show that one-half to two-thirds of the material added to the abyssal seafloor by midplate volcanic processes is due to older volcanism which erupted on young lithosphere, while the younger, higher seamounts contributed the remainder.

Seismic and bathymetric data imply the presence of lava flows in the flexural moat of the Austral Islands. Coincident multichannel seismic reflection and sonobuoy data indicate only a thin layer of sediments in a region of flat seafloor south of Marotiri. High seismic velocities directly beneath indicate that apron material is unlikely to consist of volcaniclastic sediments. I propose that the seafloor here has been paved over by abyssal basalt flows, probably associated with Austral Islands volcanism.

Thesis Supervisor: Marcia McNutt

## Acknowledgments

First I would like to thank my advisor, Marcia McNutt, for putting up with me for all of these years, giving me a great deal of freedom to work on what I was interested in, and providing me with many of the great opportunities I've had in the Joint Program.

The research presented in Chapter 2 was supported by National Science Foundation grants OCE-9012949 and OCE-9012529. Chapters 3, 4 and 5 were supported by National Science Foundation grant OCE-9415930. A National Science Foundation graduate fellowship supported my first three years of graduate study.

I thank the captain, crew and science parties of *R/V Maurice Ewing* on cruises EW9106 and EW9602, and of *R/V Roger Revelle* cruise KIWI03. I am grateful to Eric Moussat for providing, Peter Stoffers for permission to make use of, and Dave Caress for help in processing SeaBeam data collected by *F/S Sonne* cruise SO-47, funded by the German BMBF. Other data sources include EW9103, EW9204, *R/V Vema* and the satellite gravity map of *Sandwell and Smith* [1997]. Walter Smith, Cecily Wolfe, Dave Caress, Chris Gutmacher and others provided me with data at various times. Peter Buhl and Joyce Alsop provided seismic data processing and reproduction, and Jackie Graney was a great help in my visits to Lamont. Discussions with Dave Caress, Jennifer Reynolds, Dan Scheirer, Neal Driscoll, Paul Wessel, Dave Naar, Tony Watts and others helped to form some of the ideas in this thesis.

Credit should also go to many of my fellow students, from my four years on the 8th floor of the Green Building to my time in Woods Hole. Former officemates include Garrett Ito, Emilie Hooft, Gary Jaraslow, Javier Escartin, Mousumi Roy and Ben Brooks. Housemates Jay Austin and Jamie Pringle helped with good food and good martinis.

Free software programs written by Paul Wessel and Walter Smith [*Wessel and Smith, 1991*], Alistar Harding and Graham Kent, Dave Caress and Dale Chayes, and John Diebold were of great use to me for data processing and display, as were SIOSEIS and Matlab.

Chapters 2 benefitted from reviews by Paul Wessel and Marc Parmentier, Chapter 3 by reviews from Joann Stock and an anonymous reviewer. Many helpful comments on the manuscript were provided by Marcia, by my committee members, Bob Detrick, Stan Hart, Graham Kent, Uri ten Brink, and Rob van der Hilst, by Neal Driscoll, the chair of my defense, and by Allegra Hosford and Debbie Hassler.

Also thanks to Apsley Cherry-Garrard, Charles Darwin, T. E. Lawrence, Heinrich Harrer, Jon Krakauer and William Bligh, who took me far away from my thesis for a bit at a time this year.

And most of all to my parents, who never doubted I could do it.

Thanks.



# Contents

<b>Abstract</b>	<b>2</b>
<b>Acknowledgments</b>	<b>3</b>
<b>Contents</b>	<b>4</b>
<b>List of Figures</b>	<b>8</b>
<b>List of Tables</b>	<b>12</b>
<b>1 Introduction</b>	<b>15</b>
1.1 Relative plate motions . . . . .	15
1.2 The structure of propagating rifts . . . . .	17
1.3 Hotspots and midplate volcanism . . . . .	18
1.4 The Superswell . . . . .	19
1.5 Underplating . . . . .	20
1.6 Outline of dissertation . . . . .	21
<b>2 Why There Are No Earthquakes on the Marquesas Fracture Zone</b>	<b>25</b>
2.1 Introduction . . . . .	26
2.2 Data acquisition . . . . .	28
2.3 The model . . . . .	29
2.4 Stresses on the Marquesas Fracture Zone . . . . .	33
2.5 Discussion and conclusions . . . . .	45
<b>3 Pacific-Farallon Relative Motion 42-59 Ma Determined from Magnetic and Tectonic Data from the Southern Austral Islands</b>	<b>51</b>
3.1 Introduction . . . . .	52
3.2 New constraints on Pacific-Farallon spreading . . . . .	52
3.3 The structure of the Adventure Trough . . . . .	58
3.4 Discussion . . . . .	60

<b>4 History of Volcanic Loading of the Southern Austral Islands</b>	<b>63</b>
4.1 Introduction . . . . .	63
4.1.1 Morphology of the Cook-Austral chain . . . . .	64
4.1.2 Tectonic setting . . . . .	67
4.1.3 Elastic properties of the lithosphere . . . . .	68
4.2 Data collection and processing . . . . .	69
4.2.1 Multichannel seismic data . . . . .	69
4.3 Analytical flexure modeling . . . . .	71
4.3.1 Methods . . . . .	71
4.3.2 Modeling results . . . . .	76
4.4 Flexural modeling with observed topography . . . . .	78
4.4.1 Methods . . . . .	78
4.4.2 Results . . . . .	79
4.4.3 Reduced topography models . . . . .	80
4.4.4 Model results summary . . . . .	82
4.5 Discussion . . . . .	84
4.5.1 Elastic thickness . . . . .	84
4.5.2 Volcanic volumes and rates . . . . .	86
4.5.3 Causes for Austral volcanism . . . . .	86
4.6 Conclusion . . . . .	87
<b>5 Archipelagic Aprons: The Role of Mass Wasting and Volcanism</b>	<b>89</b>
5.1 Introduction . . . . .	89
5.2 Evidence for mass wasting . . . . .	89
5.3 Evidence for apron volcanism . . . . .	90
5.3.1 The “moat” . . . . .	92
5.3.2 Hummocky terrain . . . . .	96
5.4 Discussion . . . . .	101
5.5 Conclusion . . . . .	108
<b>6 Discussion and Conclusion</b>	<b>109</b>
6.1 Relative and absolute plate motions . . . . .	109
6.2 Midplate volcanism, lithospheric cracks and hotspots . . . . .	111
6.3 Flood basalts in archipelagic aprons . . . . .	112

<b>A Analytical Solutions to the Elastic Plate Equation</b>	<b>115</b>
A.1 The 2-D case . . . . .	116
A.2 The axisymmetric case . . . . .	120
<b>B Seismic Reflection Data</b>	<b>121</b>
<i>R/V Vema</i> single-channel seismic profiles . . . . .	123
<i>R/V Ewing</i> multi-channel seismic profiles . . . . .	125
<b>Bibliography</b>	<b>130</b>



# List of Figures

1-1 Gravity and tectonic maps of the South Pacific . . . . .	16
2-1 Geosat gravity map of the Marquesas Fracture Zone . . . . .	27
2-2 Schematic cross-sections of a Pacific fracture zone . . . . .	31
2-3 Shaded relief map and tectonic interpretation of Area 4 . . . . .	35
2-3 (continued) . . . . .	36
2-4 Observed and modeled gravity and bathymetry profiles for Area 4 . . . . .	37
2-5 Shaded relief map and tectonic interpretation of Area 3 . . . . .	40
2-6 Observed and modeled gravity and bathymetry profiles for Area 3 . . . . .	41
2-7 Shaded relief map and tectonic interpretation of Area 2 . . . . .	43
2-8 Observed and modeled gravity and bathymetry profiles for Area 2 . . . . .	44
2-9 Shaded relief map and tectonic interpretation of Area 1 . . . . .	46
2-10 Observed and modeled gravity and bathymetry profiles for Area 1 . . . . .	47
3-1 Simplified tectonic map of the South Pacific . . . . .	54
3-2 Tectonic map and magnetic anomalies of study region . . . . .	55
3-3 Seafloor fabric orientation in the South Austral region . . . . .	56
3-4 Bathymetry, gravity and seismic Moho profiles across the Adventure Trough . . . . .	59
4-1 The Cook-Austral chain . . . . .	65
4-2 Bathymetry of the study area . . . . .	66
4-3 Locations of multichannel seismic reflection lines and digitized Moho picks . . . . .	71
4-4 Seismic section from line A5 . . . . .	72
4-5 Observed crustal thickness across chain . . . . .	72
4-6 Three different geophysical estimates of crustal thickness for line A5 . . . . .	73
4-7 Gridded data and model output in oblique Mercator projection . . . . .	74
4-8 Contour plot of misfit between seismic Moho observations and Moho deflection in analytical loading model . . . . .	77
4-9 Contour plot of misfit between shipboard gravity data and gravity anomaly predicted by analytical loading model . . . . .	77
4-10 Topography and model Moho deflection on line A5 for northern and total load . . . . .	79

4-11	Contour plot of misfit between shipboard gravity observations and FAA in dual loading topography model with $T_1 = 1$ km . . . . .	80
4-12	Contour plot of misfit between seismic Moho observations and Moho deflection in dual loading topography model . . . . .	81
4-13	Contour plot of misfit between shipboard gravity observations and predicted FAA in dual loading topography model . . . . .	81
4-14	Contour plot of misfit between satellite gravity observations and predicted FAA in dual loading topography model . . . . .	82
4-15	Contour plot of misfit between seismic Moho observations and Moho deflection in dual loading reduced topography model . . . . .	83
4-16	Contour plot of misfit between shipboard gravity observations and predicted FAA in dual loading reduced topography model . . . . .	83
4-17	Contour plot of misfit between satellite gravity observations and predicted FAA in dual loading reduced topography model . . . . .	84
5-1	Location map for Chapter 5 . . . . .	91
5-2	Volcaniclastic sediments derived from Macdonald Seamount . . . . .	92
5-3	Shaded relief contour map of gridded hydrosweep bathymetry on the flanks of Rapa . . . . .	93
5-4	Enlarged view of Hydrosweep amplitudes on the south flank of Rapa	94
5-5	MCS image from line A9, in the “moat.” . . . . .	95
5-6	Sonobuoy 22 data . . . . .	97
5-7	Velocity profiles from 1-D forward models of arrivals from three sonobuoys on line A9 . . . . .	97
5-8	Bathymetry of line A9, along the moat south of Rapa and Marotiri .	98
5-9	Shaded relief Hydrosweep bathymetry of line A9 . . . . .	99
5-10	Grey shaded Hydrosweep amplitude data of line A9 . . . . .	100
5-11	Bathymetric profiles of four Pacific island chains . . . . .	102
5-12	EW9103 multichannel seismic profile 1162 across the Marquesas Islands	103
5-12	(continued) . . . . .	104
5-13	EW9103 multichannel seismic profile 1164 across the Society Islands .	105
5-14	KIWI03 single channel seismic reflection profile across the Hawaiian Islands . . . . .	106
5-15	EW9602 MCS reflection profile A13 across the Austral Islands . .	106
6-1	Schematic map of flexural arches of islands and large seamounts of the Southern Australs . . . . .	113
A-1	The solution to the elastic plate equation for a finite width line load .	118
A-2	The effect of varying the width $A$ of a distributed load on a 2-D elastic plate . . . . .	119
B-1	Location map for seismic profiles presented in Appendix B . . . . .	122

B-2	<i>R/V Vema</i> single-channel seismic profile V1 across Austral Islands . .	123
B-3	<i>R/V Vema</i> single-channel seismic profile V2 across Austral Islands . .	124
B-4	EW9602 multichannel seismic profile A5 . . . . .	125
B-5	EW9602 multichannel seismic profile A7 . . . . .	126
B-6	EW9602 multichannel seismic profile A9 . . . . .	127
B-7	EW9602 multichannel seismic profile A11 . . . . .	128
B-8	EW9602 multichannel seismic profile A13 . . . . .	129



# List of Tables

3.1	Predicted and observed spreading rates and azimuths in study region	57
4.1	Approximated seamount dimensions used in analytical plate loading models . . . . .	75
4.2	Values of constants used in flexural and gravity modeling . . . . .	75
4.3	Summary of flexure modeling results . . . . .	85



# Chapter 1

## Introduction

There was a special attraction in beginnings, which drove me into everlasting endeavor to free my personality from accretions and project it on a fresh medium, that my curiosity to see its naked shadow might be fed. The invisible self appeared to be reflected clearest in the still water of another man's yet incurious mind. Considered judgements, which had in them of the past and the future, were worthless compared with the revealing first sight, the instinctive opening or closing of a man as he met the stranger.

T. E. Lawrence, *The Seven Pillars of Wisdom*

Although this thesis deals with several disparate topics, they can be broadly divided into two major themes. Chapters 2 and 3 are largely concerned with small changes in relative motions between the Pacific and Farallon plates, the former investigating in detail the tectonic effect of small plate motion changes on a great Pacific fracture zone, and the latter documenting the direction and rate of one such relative motion change. Chapters 4 and 5 are about mid-plate volcanism in the South Pacific, and particularly in the southern Austral Island region. The following discussion refers to tectonic and volcanic features shown in Figure 1-1.

### 1.1 Relative plate motions

Pacific-Farallon relative motion was relatively constant for tens of millions of years, from the Cretaceous to the breakup of the Farallon plate about 25 Ma. Nonetheless,

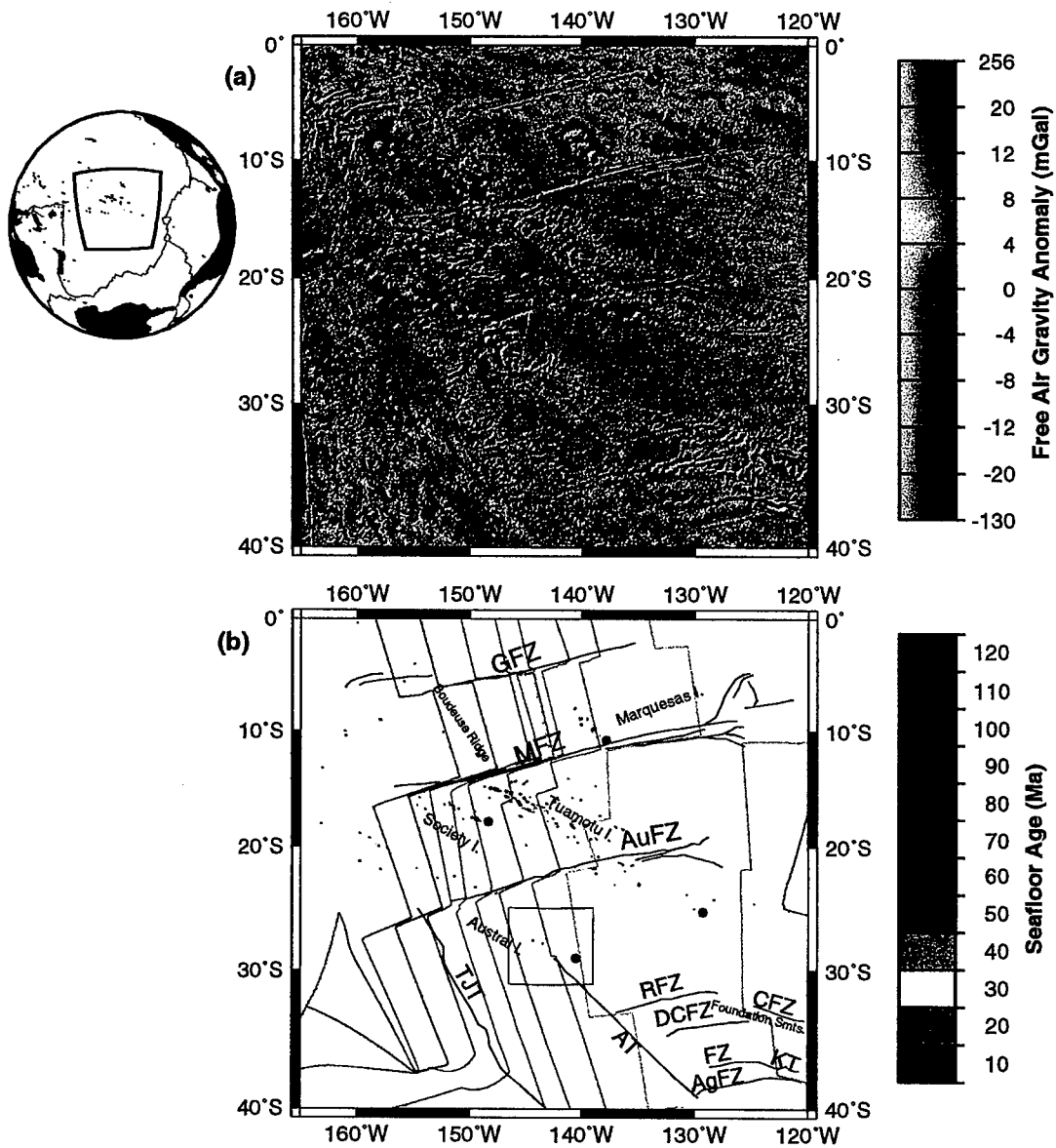


Figure 1-1: (a) Free air gravity anomaly map of the South Pacific from declassified Geosat geodetic mission and ERS-1 altimetry data (Smith and Sandwell [1995]). (b) Simplified tectonic map of the region shown in (a). Color contours indicate age of seafloor, from digital age map of Müller *et al.* (1993). Locations of labeled features are digitized from gravity map: GFZ=Galapagos Fracture Zone, MFZ=Marquesas FZ, AuFZ=Austral FZ, RFZ=Resolution FZ, DCFZ=Del Cano Fracture Zone, FZ=unnamed fracture zone, AgFZ=Agassiz FZ, CFZ=Chile FZ, AT=Adventure Trough (Cande and Haxby, 1991), KT=Kurchatov Trough, TJT=Pacific-Aluk-Farallon triple junction trace. Red circles indicate the locations of Marquesas, Society, Pitcairn and Macdonald hotspots, from north to south, respectively. The Southern Austral Island study area of Chapters 3, 4 and 5, shown in more detail in Figures 3-2 and 4-2, is indicated by a box.

many small changes in plate motion occurred during that time [e.g., *Caress et al.*, 1988; *Kuykendall et al.*, 1994]. These small changes are often accommodated by propagating rifts [Chapter 3; *Hey et al.*, 1988] and can have a large effect on the tectonics of transforms faults [Chapter 2; *Fornari et al.*, 1989].

## 1.2 The structure of propagating rifts

The most prominent tectonic feature in the Austral Islands study area of Chapters 3, 4 and 5 is the Adventure Trough (AT), the trace of an Eocene propagating rift [*Cande and Haxby*, 1991]. The AT may be traced for 1200 km in satellite gravity maps, from the Austral Islands at 29°S to the Agassiz Fracture Zone at 38°S, apparently having accommodated a 12° clockwise change in Pacific-Farallon relative motion [*Jordahl et al.*, 1998]. The southward-propagating AT must have originated in the region of the Austral Islands, as no trace of it is detectable to the north. The AT transferred about 200 km of Pacific lithosphere to the Farallon plate (much of which has since been subducted beneath South America), so it must have been propagating through  $\sim$ 10 Ma lithosphere.

*R/V Maurice Ewing* cruise EW9602 provides a unique set of data for investigating the structure of the AT. These data include crossings of the AT on four profiles near the Austral Islands with multichannel seismic (MCS), Hydrosweep, magnetic and shipboard gravity data. The bathymetry data show that the AT is not a trough in this region at all, but consists of a set of parallel topographic scarps and ridges in a zone about 75 km wide. These scarps may be due to normal faulting associated with the rifting [*Mammerickx and Sandwell*, 1986], or they may be sites of multiple rifting events as suggested by *Cande and Haxby* [1991]. Preliminary analysis of the MCS data across the AT indicates that there is a zone of thinned crust at the AT, and suggest that there may be a discontinuity of crustal thickness across the AT, with thinner crust to the southwest (prior to chron 21, about 41 Ma), and thicker crust

thereafter. A similar discontinuity of crustal thickness across the Molokai Fracture Zone is observed by *ten Brink and Brocher* [1988].

### 1.3 Hotspots and midplate volcanism

Three different models for the formation of midplate island and seamount chains include buoyant plumes from the deep mantle [Morgan, 1971], lithospheric cracking [Jackson and Shaw, 1975; Sandwell *et al.*, 1995], and a “plum pudding” model of upper mantle heterogeneities leading to localized pockets of melting [Sleep, 1984; Zindler *et al.*, 1984; McNutt *et al.*, 1997]. These models are not necessarily mutually exclusive, as it is conceivable (and even seems likely) that some volcanic chains may result from one of these processes while others are the product of another, or even that multiple processes contribute to the formation of a single volcanic chain (e.g., cracks in the lithosphere allowing the escape of pockets of melt from the upper mantle into the crust). Also, the model of a stationary hotspot [Wilson, 1963] need not be equated with a plume model [Morgan, 1971], for especially short-lived and/or irregular chains may result from more local upwelling of the upper mantle (rather than deep mantle plumes), which may be nearly stationary compared with a fast-moving plate such as the Pacific.

The Cook-Austral chain, which has long been problematic to the hotspot model [Turner and Jarrard, 1982; Okal and Batiza, 1987], may be one of the most fruitful regions to investigate the aforementioned models. The most direct test of the hotspot model lies in its prediction of the linear progression of age with along-chain distance. In the spatial distribution of radiometrically dated samples, the Cook-Austral chain dramatically fails this test of a single hotspot. One possibility is the chance alignment of multiple hotspots—at least four (at Macdonald Seamount, Rurutu, Rarotonga and the current East Pacific Rise) are required. Even this multiplication of the number of hotspots in the region, however, fails upon closer inspection of the South Australs in

the vicinity of Macdonald Seamount. From dated dredge samples, older (25–35 Ma) volcanics are found in a broad distribution, with only a weak progression of increasing age to the northwest [McNutt *et al.*, 1997]. Further, at least two volcanoes (Ra and Marotiri) that were known to contain young (< 5 Ma) volcanics thought to belong to the Macdonald hotspot have been found to have been built on much older edifices (> 20 Ma) and seem to be related to the other volcanics of the same age in the region. With the young volcanoes stretching from the Foundation Seamounts [Mammerickx, 1992], near the East Pacific Rise, to Samoa near the Tonga Trench, the Cook-Austral chain seems to resemble more closely the “hot lines” of *Bonatti and Harrison* [1976] than the “hot spots” of *Wilson* [1963].

Only a limited number of samples from the submarine portion of the chain have been dated, and a few more may yet provide constraints. Further geochemical work on these samples will address such questions as the depth of melting and the isotopic source composition of the rocks. For seamounts which are unsampled, geophysical proxies for age, based on the morphology and flexural signature, may provide a useful extension of our knowledge of volcanism in the region.

## 1.4 The Superswell

The Superswell was defined by *McNutt and Fischer* [1987] as a large region of the South Pacific which is abnormally shallow (by as much as 1 km) and is associated with other geophysical anomalies, such as a geoid low [*McNutt and Judge*, 1990], reduced elastic plate thickness [*Calmant and Cazenave*, 1986, 1987], reduced P-wave velocities in the upper mantle [*McNutt and Judge*, 1990], and an unusually high number of volcanic islands and seamounts [*Bemis and Smith*, 1993]. More recent estimates of elastic plate thickness in the region made from more complete bathymetry data show no evidence of a thinned plate, however [*Goodwillie and Watts*, 1993; *Filmer et al.*, 1993], and magnetotelluric data provide no evidence for a large thermal anomaly in

the South Pacific [*Nolasco et al.*, 1998, *in press*]. In addition, the existence of the Superswell depth anomaly itself has been challenged [*Levitt and Sandwell*, 1996] and reiterated [*McNutt et al.*, 1996]. *McNutt* [1998] provides an up-to-date review of Superswell phenomena.

Preliminary results from 1-D elastic plate modeling of the EW9602 profiles across the southern Austral volcanics [*McNutt et al.*, 1997] indicated that the young volcanic rocks of the Macdonald line are loading a 15 km elastic plate, about what is expected for 40 Ma lithosphere. However, analysis of the 2-D bathymetry and gravity data [Chapter 4] has shown that the profile modeling does not provide an accurate estimate of the size of the volcanic loads in the region. Further 2-D flexural modeling of the volcanic loading of the elastic plate discussed in Chapter 4 will provide more accurate plate thickness estimates and will shed light on more recent results [*Goodwillie and Watts*, 1993; *Filmer et al.*, 1993] that showed no systematic difference in elastic plate thickness between the Superswell and oceanic lithosphere elsewhere.

## 1.5 Underplating

Seismic refraction data has shown evidence for the existence of a dense crustal root at the base of the pre-existing ocean crust beneath the volcanic chains of Hawaii [*ten Brink and Brocher*, 1987] and the Marquesas [*Caress et al.*, 1995]. A seismic refraction experiment planned for EW9602 was crippled by the loss of 11 of 13 ocean bottom hydrophones, so direct seismic detection in the Austral Islands is not possible with the available data. There is no evidence in the seismic reflection data obtained by EW9602 for a deep crustal reflector that could be interpreted as the top of an underplating body, as observed in the Hawaiian Islands by *ten Brink and Brocher* [1987]. Gravity and flexural studies cannot provide a definitive test of the presence of underplating, but they can be used to place bounds on the size of such a body if it exists.

## 1.6 Outline of dissertation

This section briefly describes the contents and goals of each of the chapters which follow.

### Chapter 2

This chapter, entitled “Why There Are No Earthquakes on the Marquesas Fracture Zone”, was published in JGR [*Jordahl et al.*, 1995]. It deals with observations of the morphology of the Marquesas Fracture Zone and comparisons with flexural models of the thermomechanical evolution of the fracture zone. The main conclusion of this work is that the simple flexural signal of a great Pacific fracture zone [e.g. *Sandwell and Schubert*, 1982; *Sandwell*, 1984] may be masked by tectonic effects. The chief tectonic features of the Marquesas Fracture Zone are related to small changes in relative motion [*Kuykendall et al.*, 1994] that strongly affect the state of stress in the active transform region and give rise to transpressional ridges and the multiple strands of a “leaky” transform fault [*Fornari et al.*, 1989].

This chapter has undergone minor reformatting and restructuring to make it conform with the thesis. My co-authors contributed greatly to this work. The figures that were not prepared by me are credited in the figure captions, but no such attempt has been made to attribute the text.

### Chapter 3

This chapter, “Pacific-Farallon Relative Motion 42-59 Ma Determined from Magnetic and Tectonic Data from the Southern Austral Islands”, was published in GRL [*Jordahl et al.*, 1998], with the exception of Section 3.3, which was added for this dissertation and in the future may be expanded to a separate paper in itself.

This paper quantitatively treats an Eocene change in Pacific-Farallon plate motion with local observations of abyssal spreading fabric direction and magnetic anomalies.

This relative plate motion change was apparently accommodated by a large propagating rift, the outer pseudofault of which is left on the Pacific plate as the Adventure Trough [*Cande and Haxby, 1991*]. The structure of the Adventure Trough in this region is described in Section 3.3. Multichannel seismic reflection data shows crustal thinning at the pseudofault, as well as thinning of the crust on the older side of the propagating rift. I felt that these observations were important enough to include, as they bring a unique dataset to bear on the question of the structure of propagating rifts.

## **Chapter 4**

Chapter 4, "History of Volcanic Loading of the Southern Austral Islands", investigates the crustal structure and volcanic history of the Southern Austral Island region. Seismic reflection data, shipboard gravity and multibeam bathymetry data are used to constrain the crustal thickness and flexural response of the lithosphere to volcanic loading. Analytical and Fourier domain methods are used to model the elastic deformation and estimate the volume of volcanic material.

## **Chapter 5**

Chapter 5. "Archipelagic Aprons: The Role of Mass Wasting and Volcanism", discusses the morphology and origin of some features in the Southern Austral region. Of special interest are the smooth basement topography of the south moat and a large hummocky terrain south of Marotiri. I propose that the simplest hypothesis for the origin of both terrains is midplate volcanism related to the seamount chains in the area. Mass wasting in the study area is also discussed, as well as seismic data and observations from other Pacific island chains.

## **Chapter 6**

This chapter presents the final discussion and concluding remarks for the dissertation.

## **Appendix A**

This appendix simply includes a number of analytical solutions to the elastic plate equation that were used in Chapter 4, and a brief discussion about the behavior of the solutions.

## **Appendix B**

This appendix presents a number of seismic reflection lines from the Austral Islands, including two single channel lines collected by *R/V Vema* in 1965 and the MCS profiles collected by *R/V Ewing* in 1996.



## Chapter 2

# Why There Are No Earthquakes on the Marquesas Fracture Zone

Exploration is the physical expression of the Intellectual Passion. And I tell you, if you have the desire for knowledge and the power to give it physical expression, go out and explore.

Apsley Cherry-Garrard, *The Worst Journey in the World*

### Abstract

Although the plate tectonic paradigm does not predict relative horizontal motion between lithosphere on opposing sides of a fracture zone, the fact that younger, more rapidly subsiding seafloor lies adjacent to older seafloor implies relative vertical motion. The observation that fracture zones are notably aseismic has led to the proposition of high strength along fracture zones, such that the differential subsidence is accommodated by flexure across a locked fault. This model predicts that a ridge develops on the young side of the fracture zone flanked by a foredeep trough on the old side, with parallel warping of the Moho and large associated gravity anomalies. Previous analyses of satellite altimetric passes over Pacific fracture zones have shown that the amplitude and shape of the gravity anomalies frequently do not conform to the predictions of this simple model. One of the most notable departures has been the Marquesas Fracture Zone (MFZ), where only one limited section was determined to be “high strength”. Curiously, the only earthquake to rupture the MFZ in the last 35 years is located in this locked region. Elsewhere, where we would predict vertical slip must be occurring, the fault is aseismic. To better understand the history of vertical motion on this fault we have analyzed geophysical data obtained during the recent survey EW9106 aboard the R/V *Maurice Ewing*. Our detailed Hydrosweep, gravity, and seismic data resolve this paradox by showing no evidence for vertical slip along the fault. Shear stresses caused by differential thermal subsidence do not exceed the strength of this fault. Rather, the failure of the altimetry signal to conform

to the predictions of the high-strength model along much of the MFZ is caused by changes in the Pacific-Farallon pole of rotation. Reorientation of the plate boundary was accommodated by propagating rifts, intra-transform tension or compression, and changes in transform offset that complicated the signal from differential subsidence across a locked fault. For example, a counterclockwise rotation of the transform in the Cretaceous caused overthrusting in the transform and thus compensation of the depth differential by flexural loading of a very young plate. A clockwise rotation of this right-stepping transform fault at about 35 Ma led temporarily to a crenulated plate boundary and later to the development of intra-transform spreading centers. After accounting for these complications, the fracture zone appears capable of sustaining at least 20 MPa of shear stress and remains locked along the entire length of the fault except perhaps locally where it passed over the Tuamotu and Society hot spots.

## 2.1 Introduction

The Marquesas Fracture Zone (MFZ) spans the central Equatorial Pacific from approximately 9°S, 239°E to 15°S, 202°E and marks a right-lateral offset in the former Pacific-Farallon ridge system which created the sea floor in the Pacific Ocean from the Cretaceous until the Miocene (Figure 2-1). The age offset along the fault, where well constrained by magnetic lineations, is between 9 and 12 My [Kruse, 1988; Cande *et al.*, 1989; Sandwell *et al.*, 1995], which is fairly typical of the other great Pacific fracture zones (FZs). On a bathymetric map, however, the Marquesas is exceptionally prominent on account of the presence of a large depth anomaly on its southern side (the “South Pacific Superswell”) that amplifies the depth differential across the fault [McNutt and Fischer, 1987].

In September-October, 1991, we conducted the first-ever marine geophysical survey entirely devoted to a great Pacific FZ, following the MFZ along almost its entire length using a Hydrosweep swath-mapping system, single-channel seismic, gravity and magnetic profiling, and occasional dredging. Our observations of the MFZ have now led us to revise many previous beliefs concerning this great Pacific fracture zone.

To begin with, our tracing of the FZ extends its western terminus by more than

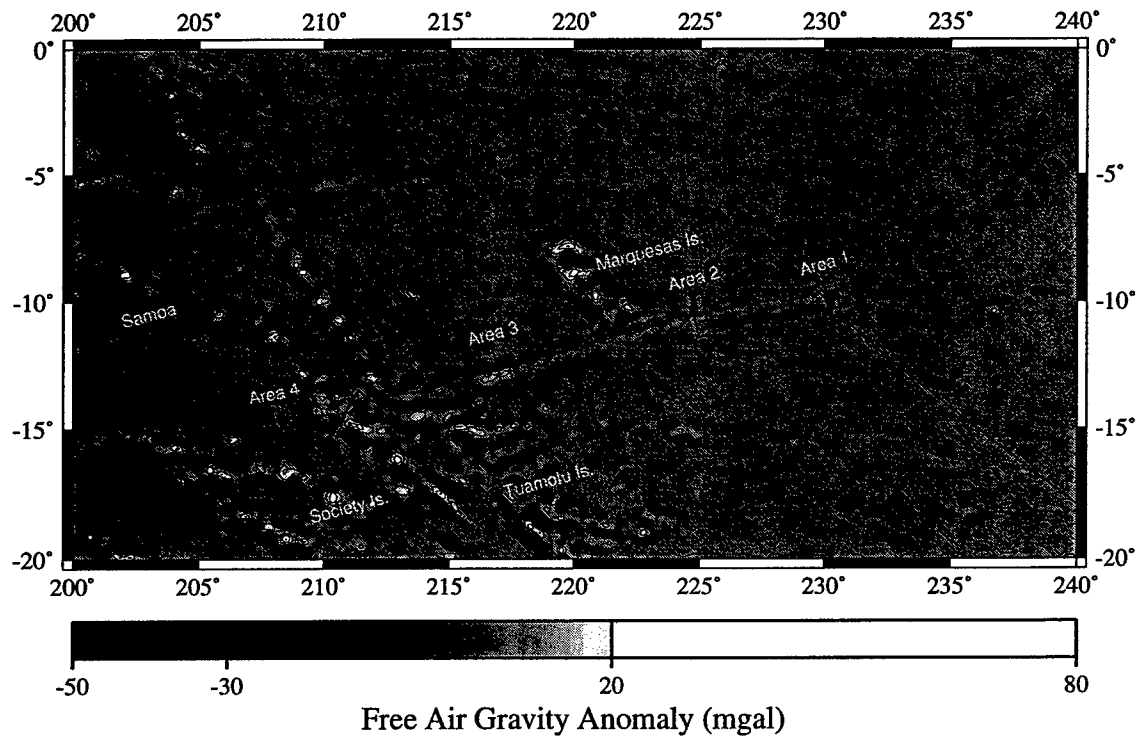


Figure 2-1: Geosat gravity map showing the location of the survey track of the R/V *Ewing* along the Marquesas Fracture Zone (MFZ). Data are high-pass filtered ( $l < 500$  km) to show only features with wavelengths less than a few hundred kilometers. Geosat data courtesy of David Sandwell.

800 km beyond its previously mapped limit, and places its origin more than 1500 km west of the end of the Cretaceous Superchron. This information provides an important constraint on the timing of the plate reorganization which led to the establishment of the Pacific-Farallon spreading system that dominated Pacific tectonics until the Miocene and on the poles of rotation which describe Pacific-Farallon spreading [Kuykendall *et al.*, 1995]. Here we report the analysis of longer survey lines oriented perpendicular to the fracture zone in order to study the evolution of its morphology and deep structure as it ages from east to west.

## 2.2 Data acquisition

The main tool we used to follow the trace of the Marquesas Fracture Zone was the Krupp Atlas Hydrosweep system. Sixty narrow-beam echo sounders provided swath coverage with a total width of two times the water depth. In the deep sea, the swath width is 8 to 10 km, making it fairly easy to follow the trace of the MFZ to the west. Subbottom penetration to locate volcanic basement beneath volcaniclastic and pelagic sediment was achieved by a single-channel seismic streamer and a water-gun sound source.

Two gravimeters were available on the *Ewing*: a Bell Aerospace BGM-3 marine gravimeter and a Boogenwerk KSS-30 gravimeter. The Bell meter provided noisier gravity data than the KSS-30, and therefore we relied entirely on data from the KSS-30. The KSS-30 gravity data consists of 6-s averages. After merging with the navigation, the Eötvös correction was applied and the 1980 theoretical gravity formula subtracted to yield free air gravity anomalies.

The primary source of navigational information was a Magnavox T-set Global Positioning System receiver, logging at 2-s intervals. A Magnavox MX-1107RS dual frequency Transit satellite receiver was used for backup. Typically, GPS positions were available for more than 23 hours per day.

Most of the survey consisted of a series of lines crossing the fracture zone at low angle so as to maximize coverage without losing the trace of the fracture zone (Figure 2-1). At four locations along the fracture zone we ran pairs of geophysical profiles perpendicular to the trace of the fracture zone out to a distance of 60–100 km on either side. For Area 1 (Figure 2-1), we also ran a number of shorter contiguous profiles parallel to the fracture zone. The long swaths perpendicular to the fracture zone allow 2-D modeling of crustal and lithospheric features, while the shorter profiles parallel to the fracture zone define its detailed morphology. Unfortunately, time constraints prevented us from running fracture-zone-parallel lines in the other survey areas. The locations of these detailed study areas were chosen such that a region midway between hot spot intersections was sampled. At the fracture zone-hot spot intersections, we surveyed and dredged the volcanoes lying along the trace of the fracture zone. Several dredges also sampled the fracture zone scarp itself. Analysis of the geophysical and petrological data from the fracture zone-hot spot intersections is the subject of a separate study.

## 2.3 The model

We begin by assuming that the fracture zone should evolve following the model of *Sandwell and Schubert [1982]*. Initially, at the ridge-transform intersection (RTI), a bathymetric step across the fault is locally compensated by deep temperature differences in the lithosphere (Figure 2-2). Later, as the two sides of the fracture zone approach thermal equilibrium through vertical and horizontal (i.e., across the fault) conduction of heat, the scarp is increasingly supported by vertical shear stresses on the fracture zone if the fault is locked, preventing the vertical slip necessary to maintain local isostasy. As the regions far from the fracture zone asymptotically approach the same depth, the step is modified by elastic stresses in the lithosphere to produce a ridge on the young plate flanked by a trough on the old plate. Gradual thicken-

ing of the elastic plate with increasing age causes the wavelength of the flexure to become progressively longer for each new increment of subsidence. We assume that the thickness of the region of the tectonic plate that behaves elastically is controlled by the depth to the 600°C isotherm as predicted by one-dimensional cooling of a half space. Thus elastic thickness varies with age on either side of the fault, but we ignore perturbations to strength that might be caused by lateral conduction of heat across the fault or preexisting thermal stress [e.g., *Wessel*, 1992]. We do include the bending of the lithosphere caused by thermal stress accumulating along the active portion of the transform fault and becoming locked in at the RTI [*Parmentier and Haxby*, 1986; *Wessel and Haxby*, 1990]. This component of the relief principally effects the depth of the basement beneath the sediments in the foredeep and is difficult to discern in our single-channel seismic data. We will refer to the combination of these two effects as the “locked fault” model. Our formulation of the problem follows exactly that of *Christeson and McNutt* [1992] (hereafter referred to as C&M), which in turn is a simplification of the methodology of *Wessel and Haxby* [1990]; therefore, the details are not repeated here.

Given lithospheric ages and the fault’s age offset based on magnetic lineations [*Kruse*, 1988; *Cande et al.*, 1989], we can compute the relief on the sea floor, parallel warping on the Moho, and the gravity from undulations of these two density interfaces as predicted by this high-stress model and simple variations on it. The locked fault model predicts large relief ( $\sim 1.5$  km for the age offset of the MFZ) of ridges and troughs paralleling the fracture zone. In addition, because both the sea floor and the Moho are warped in the same sense without intracrustal deformation according to this model, the gravity anomalies over these features are very large compared to what one would calculate on the assumption of local isostasy (i.e., crustal thickening under the ridges and crustal thinning beneath the troughs), and thus easily discernible in satellite altimetry data. If the stress required to support this topography exceeds the shear strength of the fault, the lithosphere may fail, thus removing the ridge and

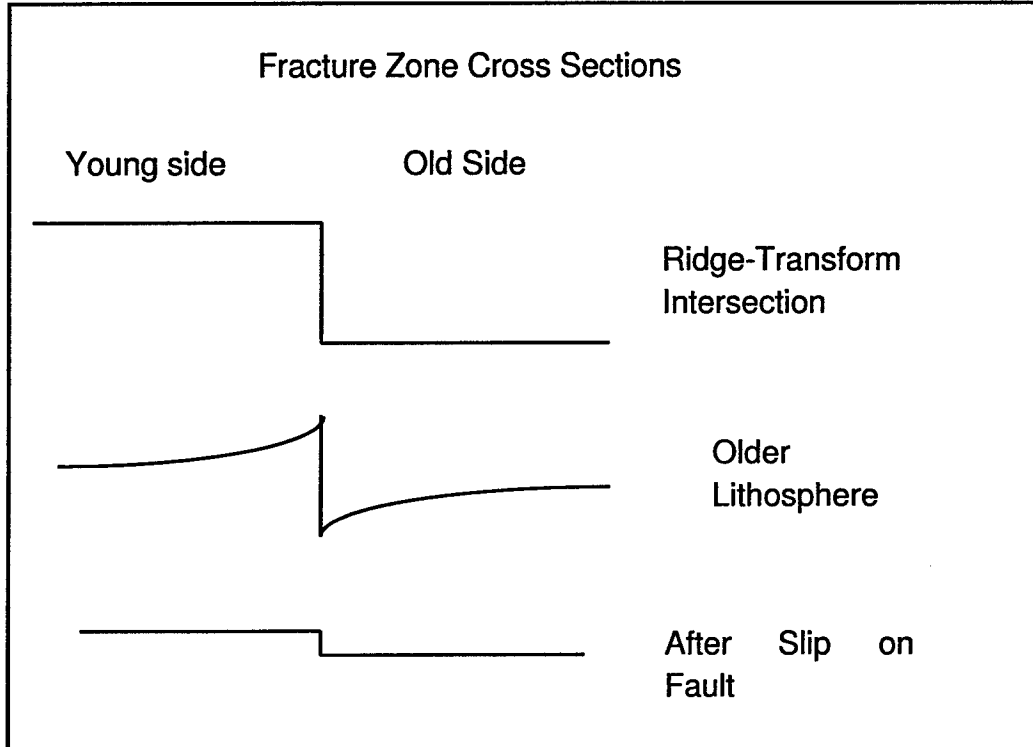


Figure 2-2: Schematic cross-sections of a Pacific fracture zone showing flexural modification of the bathymetric scarp across a locked fault as the lithosphere ages past the ridge-transform intersection (RTI). Relief on the scarp is typically 1 km or more for the large-offset Pacific fracture zones. The final stage would slip along the fracture zone if the vertical shear stress needed to maintain the flexural topography exceeds the strength of the fault. [Figure by MKM]

trough and leaving only whatever bathymetric step might be predicted from the ages of the plates on either side of the fracture zone (Figure 2-2) and the bending from accumulated thermal stress.

Before displaying the data from the cross-sections and the predictions from the models, the depth offset caused by the different ages of the lithosphere on either side of the fracture zone is removed by fitting a smoothed step to the bathymetry data following the method of C&M. The shape of the step includes the effect of lateral heat conduction across the fault which is determined by the ages of the opposing plates, but its amplitude is scaled for each individual profile in order to obtain a best fit to the regional depths to the north and south well away from the fracture zone. The amplitude of the step was further fine-tuned using the Bouguer gravity data, in that choice of an inappropriate reference depth leads to obvious steps across fault in the gravity field. Only in Area 1 near the eastern end of the MFZ are the regional depths similar to the predictions of the standard depth-age relation [Parsons and Sclater, 1977]. Further west, the depth anomalies consistently increase from 400 m (Area 2) to 1000 m (Area 4) on account of the excessively shallow seafloor associated with the Marquesas swell [Fischer et al., 1986] and the South Pacific Superswell [McNutt and Fischer, 1987]. Step heights are 200–440 m, as predicted by the thermal plate model of Parsons and Sclater [1977], indicating that the regional depth anomalies are affecting the lithosphere on both sides of the fault in the vicinity of the MFZ.

After removing this step, the predicted relief on the seafloor is compared to the bathymetry along 8 long lines perpendicular to the fracture zone in 4 widely separated study areas. The predicted relief on the Moho is next compared to the “observed” relief on the Moho calculated from the Bouguer gravity anomaly (free air gravity minus the attraction of the seafloor topography) downward continued to the oceanic Moho and converted to equivalent Moho undulations. Finally, the gravity field from the seafloor relief and our preferred model for the Moho structure is compared to the measured free air gravity anomaly along each of the 8 profiles. In calculating all

gravity anomalies, we used *Parker's* [1973] method taking all structures to be two dimensional. Densities of 1000, 2200, 2650, and 3300 kg/m<sup>3</sup> are assumed for water, sediment, volcanic basement, and mantle, respectively.

## 2.4 Stresses on the Marquesas Fracture Zone

In a previous analysis of satellite altimetry and limited shipboard crossings, C&M found that the topography and gravity signal of the MFZ resemble the predictions of this locked-fault model only in a limited region near 217°E. Elsewhere, the relief as observed in the bathymetry data or inferred from the altimetry data is simply too small to be consistent with this model of flexure across a locked fault. C&M interpreted this observation as evidence for a weak fault unable to maintain the stresses from differential subsidence. The obvious corollary to their conclusion is that the fault should be slipping vertically, especially along the younger sections east of the Tuamotu Islands, as the Pacific plate continues to age. A simple calculation shows that the total seismic moment  $M_0$  that would be released along the MFZ by 1 over its 3000-km length is  $\sim 6.6 \times 10^{23}$  N m. If the elastic energy is released at a constant rate over the age of the MFZ, we would expect about one earthquake of magnitude 5.3 per year. However, the ISC catalog of earthquakes from 1964–1989 records only one event (of magnitude 4.3, no focal mechanism available) along the MFZ (Figure 2-1), and that one epicenter is along the only section of the fault that is not predicted to be slipping, according to the study by C&M. Either the past  $\sim 35$  years is not representative of the seismicity of this fracture zone, its slip is virtually aseismic, or the satellite gravity field has been incorrectly interpreted as indicating a weak fault.

After we acquired the shipboard gravity, multibeam bathymetry, and single-channel seismic data, it became clear that the last explanation is the correct one. Along our survey route, the MFZ exhibited a wide variety of morphological forms, which on random crossings or with low-resolution satellite data might not even have been rec-

ognized as the same tectonic feature, much less a locked fault.

An example from our westernmost survey, Area 4 (Figure 2-3), serves to illustrate the complications that would not be detected in satellite data. In this region just a few degrees west of the Tuamotu Islands, the flexural foredeep north of the fracture zone is completely buried beneath a smooth sediment plane and produces no bathymetric relief. The flexural scarp is replaced by a sinuous, symmetric ridge between 208° and 209°E. Further west the existence of the fracture zone can only be inferred from the curved tips of abyssal hills on the south side (Figure 2-3) that spilled over into the transform trough when the lithosphere was created [Lonsdale, 1986]. Neither the bathymetry (solid line, Figure 2-4c) nor the Moho geometry inferred from the downward-continued Bouguer gravity (solid line, Figure 2-4d) conform to the predictions of the high-stress model (dotted lines, Figures 4c,d). In fact, the Bouguer gravity anomaly implies crustal thickening beneath the sinuous ridge, just the opposite of the crustal thinning beneath elevated regions predicted by thermal stress and flexure across a locked fault. This is the region where C&M proposed complete unlocking of the fracture zone.

However, the departures of the signal in Area 4 from the predictions of the high-stress model can be explained easily by tectonic events early in the history of this seafloor without invoking vertical slip along the fracture zone. Area 4 coincides with a change in the orientation of the fracture zone which *Kuykendall et al.* [1995] attribute to a counterclockwise rotation of the active plate boundary during the Cretaceous. We see evidence for this reorientation of the plate boundary in the oblique trends just south of the ridge (Figure 2-3a,b), which we interpret as outer pseudofaults [Caress *et al.*, 1988] from propagating ridges that accomplished the counterclockwise reorientation of the spreading system (Figure 2-3c). A counterclockwise rotation of a right-stepping offset would lead to compression within the active transform. Indeed, the Bouguer gravity data can be reasonably fit with a model that assumes the Moho north of the fracture zone is flexed as a young, weak elastic plate beneath the weight

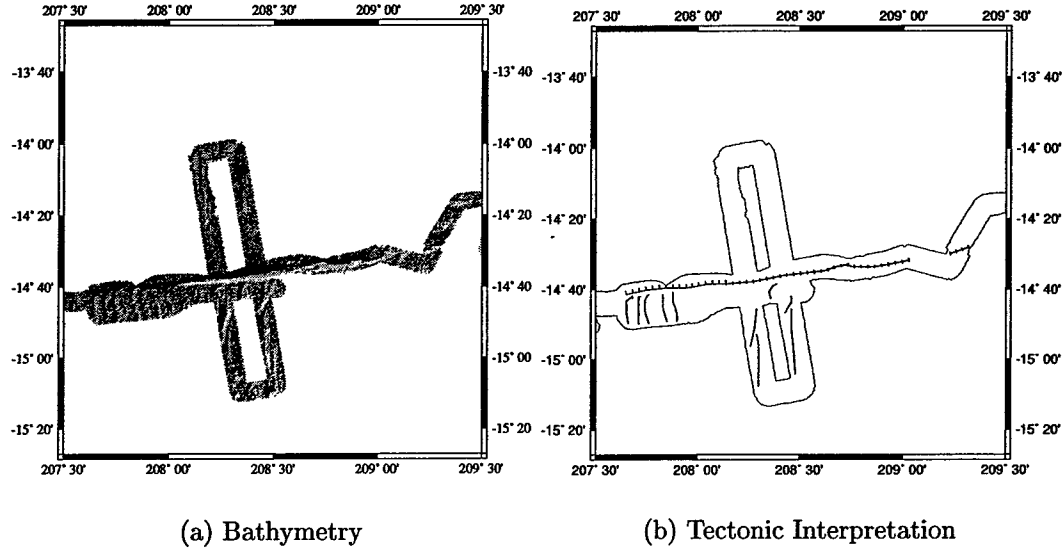


Figure 2-3: (a) Shaded relief map from Hydrosweep data showing sea floor fabric in Area 4. Image is illuminated from the southeast. (b) Line drawing showing tectonic interpretation of features in the Hydrosweep data. Outline shows area of hydrosweep coverage. The western portion of the fracture zone displays the sharply curved relief of the abyssal hills produced at the ridge-transform intersection prior to the shift in pole position. The stippled portion of the fracture zone trace indicates a scarp facing in the direction of the stippling (double stippling indicates a ridge). We interpret the large, roughly east-west median ridge to be a compressional feature caused by a counterclockwise (CCW) rotation of the plate boundary. The oblique ridges just south of the median ridge are interpreted as outer pseudofaults of northwest propagating ridges that realigned the spreading center to be orthogonal to the new direction of spreading.

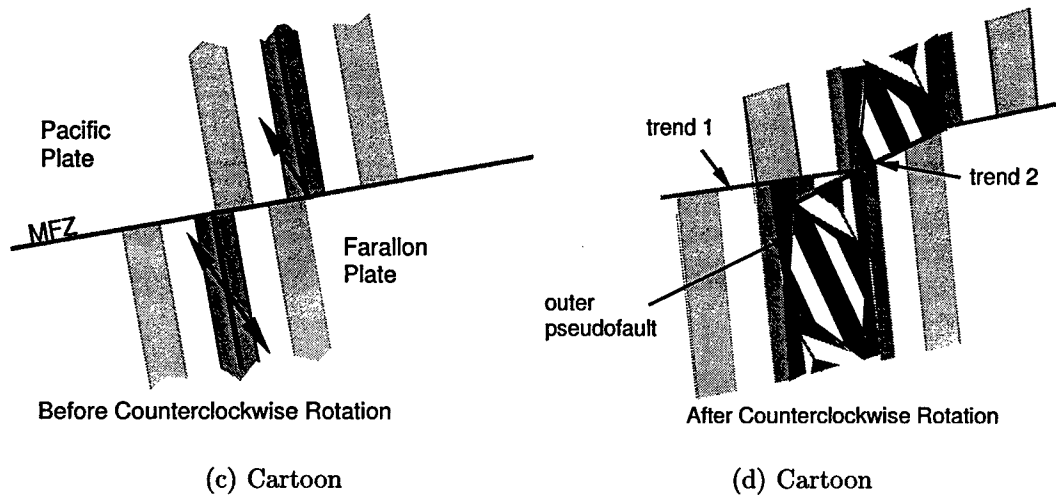


Figure 2-3: (continued) (c & d) Cartoons illustrating how the change in direction of motion might have occurred. Thick black stripes represent the ridge segments, dashed lines the fracture zones, and grey stripes the orientation of sea floor fabric. As the pole begins to shift, arrows indicate the location and propagation direction of propagating ridges. The right-hand cartoon shows the sea floor fabric produced after propagation has realigned much of the spreading center orthogonal to the new direction of spreading. Of course, only the fabric produced on the Pacific plate is observable in the Hydrosweep data. The fact that at least two pseudofaults are seen in the data indicates that the reorientation of the ridge was accomplished by a series of at least two northwestward propagation events. The trend of the pseudofaults is controlled by the rate of propagation relative to the spreading rate. The fact that the eastern pseudofault is more east-west than the western one indicates that the second event propagated more slowly, assuming no change in spreading rate. [Cartoons by MKM]

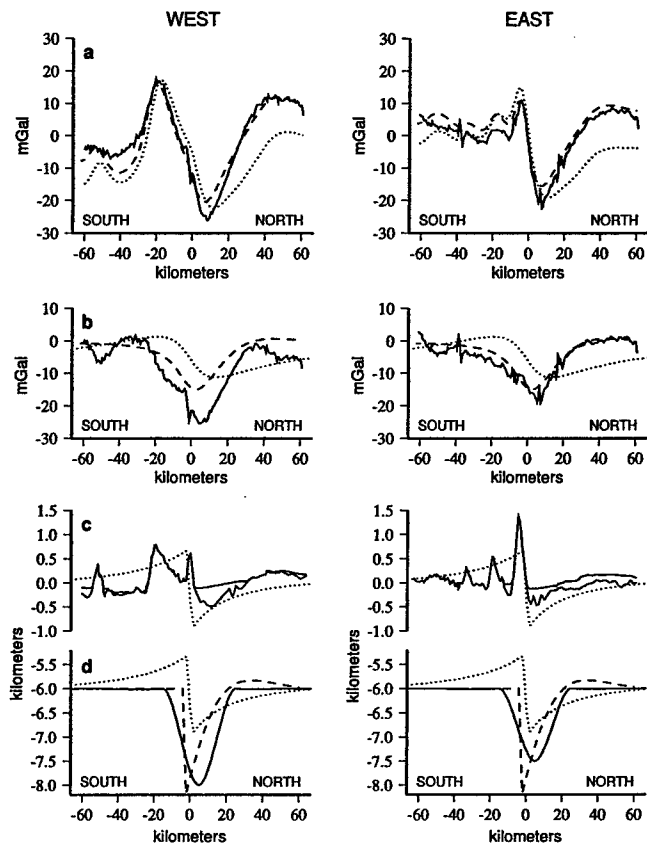


Figure 2-4: Gravity and bathymetry data from Area 4 measured along the two long north-northwest-south-southeast profiles shown in Figure 2-3. Solid lines in each panel correspond to (a) free-air gravity anomaly, (b) Bouguer gravity anomaly, (c) bathymetry, and (d) predicted Moho geometry obtained from downward continuation of the Bouguer gravity. For the bathymetry, both the bottom reflection (sediment surface) and the basement depth are plotted. The Bouguer gravity is calculated from the free-air gravity by subtracting the attraction of the rock-water interface assuming that structures are two-dimensional. The dotted lines in (a)-(d) are the predicted free-air gravity, Bouguer gravity, topography, and Moho geometry from the simple locked-fault model. The age of the northern plate and age offset along the transform are assumed to be 85 Ma and 15 My, respectively. Because no magnetic lineations exist in this area, the age difference was estimated from the magnitude of the scarp; for old sea floor, the depth offset is not very sensitive to small variations in age offset across the fracture zone. The dashed lines in (a)-(d) are the free-air gravity, Bouguer gravity, bathymetry, and Moho geometry predicted by assuming that the southern scarp overthrust the northern plate by a few kilometers. The best-fitting model assumes an elastic plate thickness of 4 km and an end-plate load of  $20 \text{ km}^2$  of excess crust (consistent with the area of the overthrust crust). The actual basement relief and sediment thickness rather than the theoretical bathymetry was used in calculating the free-air anomalies. [Figure by HFW]

of southern scarp which overthrusts the northern plate by a few kilometers (dashed line, Figure 2-4d). This model provides a reasonable fit to the Bouguer and free-air gravity data, especially along the eastern crossing (Figure 2-4a,b). Misfit to the western profile is likely caused by breakdown of our assumption that the structures are two-dimensional.

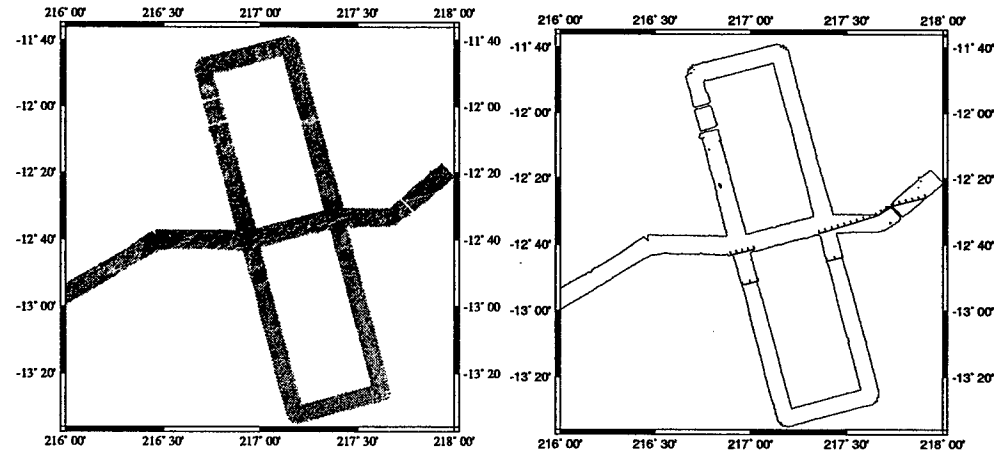
According to this model, the mass excess of the southern ridge is supported by vertical normal stresses applied to the northern plate after the southern scarp physically overthrust the northern plate in a compressional transform regime. The extremely small elastic plate thickness  $T_e$  required to match the gravity signal, 4 km, supports the conclusion that the entire loading took place near a midocean ridge [Watts *et al.*, 1980]. This small effective  $T_e$  in Area 4, in addition to the superposition of the southern ridge (with its gravity high) over the northern trough (with its gravity low), causes a reduction in amplitude and wavelength of the gravity signal, and thus explains why the satellite gravity data examined by C&M failed to resolve the expected ridge-trough signature. In Area 4, the ridge-trough morphology is not, and was never, maintained by shear stresses on a vertical fault plane. Because this overthrust geometry prevents us from calibrating the present shear strength of the fracture zone in the region, there is no evidence here for either a weak or a strong fault.

The gravity data in Area 4 could be equally well fit by a model that assumes the sinuous ridge to be a volcanic rather than a tectonic feature that erupted through a weak, unlocked fracture zone early in its history (in order to explain the low value for  $T_e$ ) while it simultaneously accumulated thermal stress. There are several reasons why we prefer the tectonic explanation. First, we see no evidence in the bathymetry data that this ridge is a coalesced group of volcanic cones (Figure 2-3). Second, there is evidence for a flexural foredeep buried beneath sediment only on the north side of the fracture zone; clearly it is a one-sided flexural foredeep. Finally, the counterclockwise rotation of the spreading system at this time put the transform under compression. There is no less likely spot along the MFZ system for early unlocking or crustal

extension leading to ascent of magma.

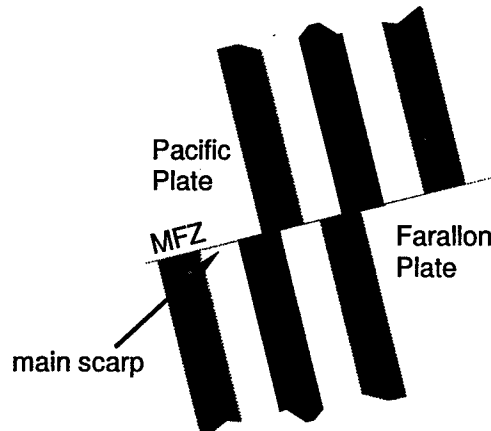
Midway between the Marquesas and Tuamotu Islands (Area 3, Figure 2-5a), the fracture zone is a classical example of the locked-fault model (Figure 2-6). This is the only section of the fault where C&M found evidence for a strong fracture zone. In contrast to Area 4, here the loading occurs over tens of millions of years as the thermal support for the scarp cools, and the flexure is accommodated by a gradually thickening elastic plate with an effective  $T_e$  exceeding 10 km. Deviations from the modeled bathymetry (Figure 2-6c) provide evidence for mass wasting of the southern scarp and down-slope movement of large blocks into the flexural trough. While the scarp height in the bathymetry (1.7 km) matches the value predicted from the age contrast across the fault in this area, the inferred amount of relief on the Moho is closer to 2.4 km (Figure 2-6d). This may be evidence for some tectonic unroofing (*i.e.*, removal of surficial rock layers by tectonic processes) of the younger plate within the transform environment that led to crustal thinning on the south side and thickening on the north side of the fault.

Just east of the Marquesas Islands (Area 2, Figure 2-7) is another region that lay within the active transform during a second change in the Pacific-Farallon pole of rotation, this time involving a  $\sim 6^\circ$  clockwise rotation of the spreading system at 35 Ma [Kuykendall *et al.*, 1995]. In this region, the Hydrosweep data show a smaller south-facing scarp (Figure 2-7a,b) just south of the large north-facing scarp which marks the main trace of the fracture zone. This south-facing scarp has the more easterly trend characteristic of the fracture zone after the clockwise rotation of the plate boundary. Profiles of bathymetry are better fit by a model with 2 offsets in the fracture zone, one right stepping and one left stepping (Figure 2-8d). On account of the existence of the left-stepping offset just 40 km to the south of the main fracture zone, the age offset on the northern, right-stepping ridge offset is greater than that predicted from magnetic lineations which have only been mapped well north and south of the fracture zone. Our tectonic modeling (Figure 2-7c) suggests that the



(a) Bathymetry

(b) Tectonic Interpretation



(c) Cartoon

Figure 2-5: As in Figure 2-3, showing (a) shaded relief map of Hydrosweep bathymetry from Area 3, illuminated from the southeast; (b) interpreted tectonic features; (c) cartoon of simple plate geometry that existed when this sea floor was created. [Cartoon by MKM]

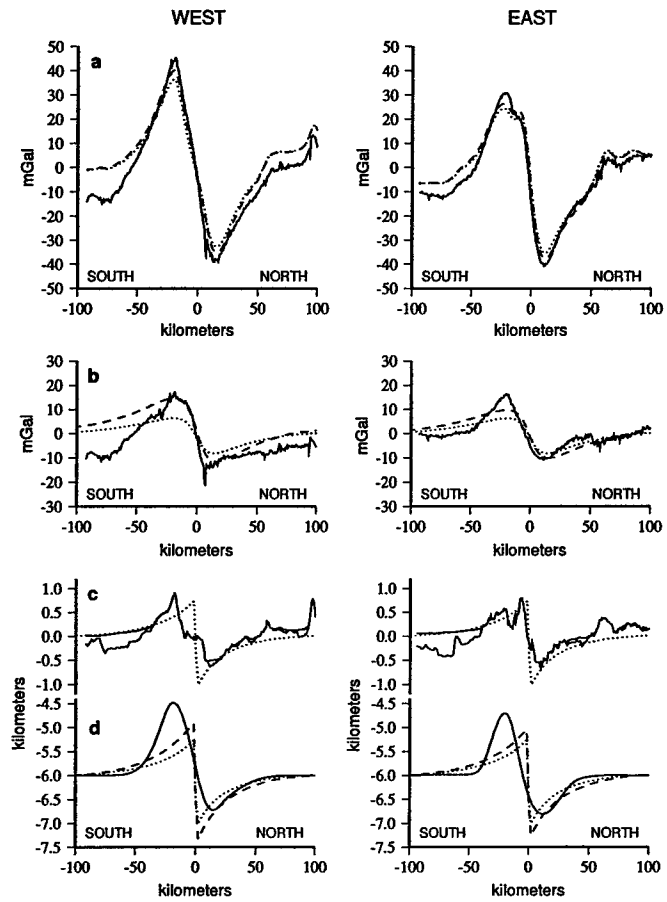
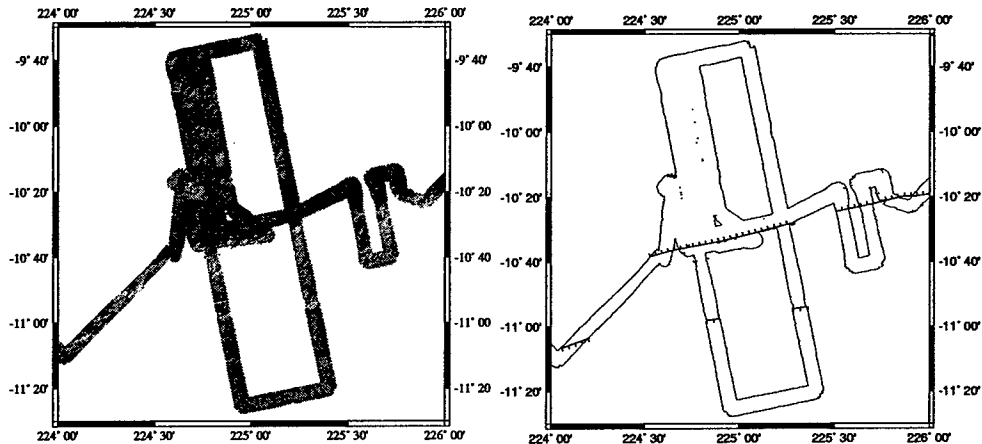


Figure 2-6: As in Figure 2-4, heavy solid lines show (a) free-air gravity anomaly, (b) Bouguer gravity anomaly, (c) bathymetry, and (d) predicted Moho geometry obtained from downward continuation of the Bouguer gravity along the two long north-northwest-south-southeast profiles shown in Figure 2-5. The dotted lines show the predictions from the locked-fault model. Age of the northern plate and age offset along the fault are 65 Ma and 15 My, respectively. The dashed lines shows a slightly better fit to the Moho geometry and gravity anomalies for a model with extra relief on the Moho as might be caused by transfer of crust from the younger plate to the older plate while within the active transform. The misfit of the predicted gravity to the observed gravity along the southern section of the profile may indicate that we have overestimated the density of the sediment. [Figure by HFW]

change in the pole of rotation was accomplished by propagating ridges that created a temporary crenulate ridge system. Unlike the case for Area 4, the trace of the propagating rifts is not obvious in our swath coverage; thus we cannot rule out the possibility that discrete ridge jumps created the crenulate pattern.

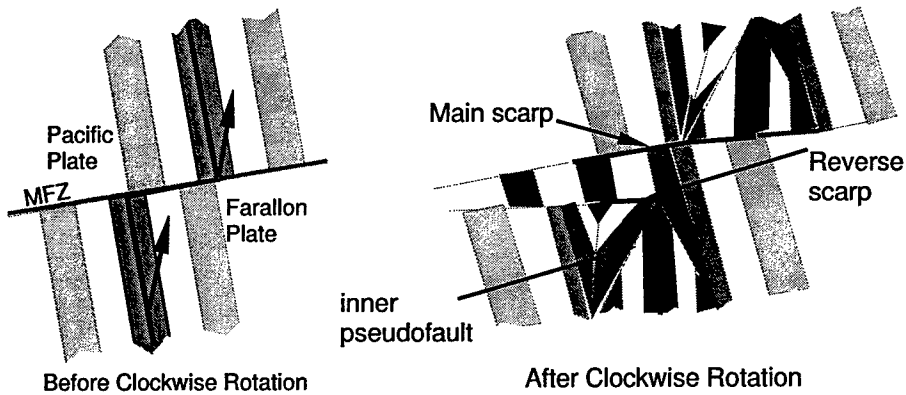
Our initial examination of the Bouguer gravity (Figure 2-8b), however, did not reveal the expected 10-mGal gravity high beneath the ridge at distance of -50 to 0 km. Instead, the Bouguer gravity is a long-wavelength gravity low with amplitude of 20 mGals and wavelength of 200 km. Attempts to model this gravity low as conventional isostatic compensation of a surface load (e.g., as we did in Area 4) failed; any mass deficit compensating the observed topographic relief is completely insufficient to produce a gravity low of this magnitude, which suggests that the gravity low is unrelated to the relief of the fracture zone. Furthermore, the wavelength of this gravity feature is too long to be associated with the FZ's crustal structure. An examination of the Geosat gravity field in this region [Sandwell and Smith, 1994] indicates that one of the "crossgrain" gravity rolls characteristic of the central Pacific intersects the MFZ at approximately this position (Figure 2-1). Various explanations have been proposed for these anomalies, including small-scale convection [Haxby and Weissel, 1986], the passage of mini-hot spots [Fleitout and Moriceau, 1992], and stretching of the Pacific plate [Sandwell *et al.*, 1995]. These gravity rolls typically have a wavelength of 150 km and an amplitude of 20 mGals. If we remove a sinusoid with this amplitude and wavelength from the data, the residual Bouguer gravity (Figure 2-8c) is now relatively well fit by the model with a northern right-stepping and a southern left-stepping fracture zone.

Further east in Area 1 (Figure 2-9a,b) we see that this system of a right-stepping and left-stepping fracture zone system later evolved, presumably via spreading center jumps or propagating ridges, to a series of right-stepping transforms separated by short intra-transform spreading centers, similar to those observed by *Fornari et al.* [1989] at the Siqueiros transform. Each individual fault trace is parallel to the Pacific-



(a) Bathymetry

(b) Tectonic Interpretation



(c) Cartoon

(d) Cartoon

Figure 2-7: (a) Shaded relief map of Hydrosweep bathymetry from Area 2, illuminated from the southeast. (b) Interpreted tectonic features. The main trace of the MFZ follows the northern scarp with an azimuth of N75°E west of 225°40' and N82°E east of that point, indicating a change in the pole of rotation during this time. The location of an oblique linear feature tentatively identified with an inner pseudofault is indicated. The southern scarp has the N82°E direction. (c) Cartoons of what the area would have looked like when an active plate boundary just before and after the change in pole of rotation. In the left-hand cartoon, as the pole begins to shift arrows indicate the location and propagation direction of propagating ridges. The right-hand cartoon shows the sea floor fabric produced after propagation has formed a crenulate ridge (thick black stripe) with two transforms with different senses of offset. Of course, only the fabric produced on the Pacific plate is observable in the Hydrosweep data. [Cartoons by MKM]

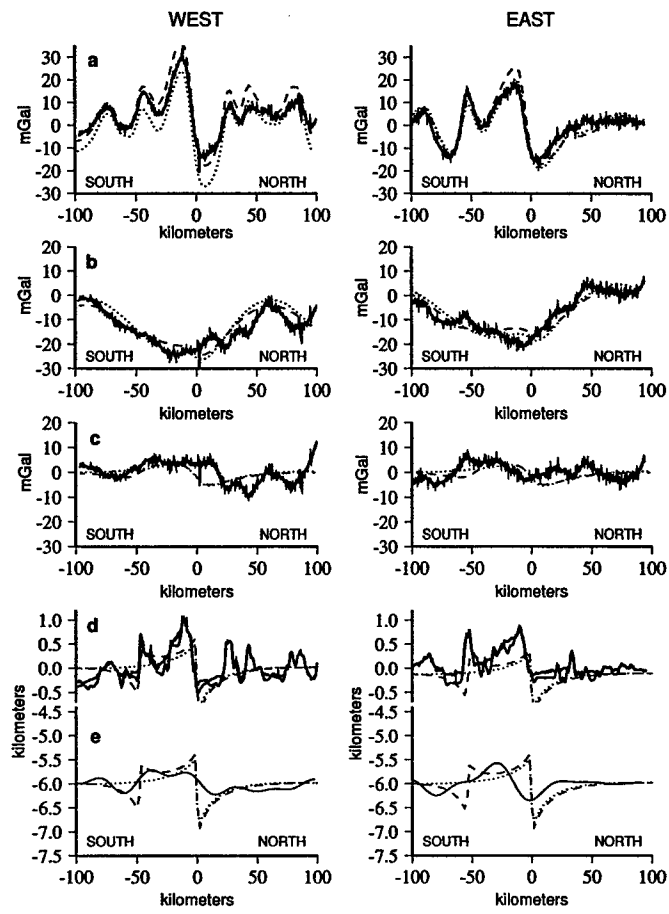


Figure 2-8: Gravity and bathmetry data from Area 2 measured along the two long north-northwest-south-southeast profiles shown in Figure 2-7. Solid lines in each panel correspond to (a) free-air gravity anomaly, (b) Bouguer gravity anomaly, (c) Bouguer gravity anomaly with a 150-km (west) or 190 (east) wavelength, 24-mGal amplitude (peak-to-trough) sinusoid subtracted from the data, (d) bathymetry, and (e) predicted Moho geometry obtained from downward continuation of the gravity in (c). For the bathymetry, both the bottom reflection (sediment surface) and the basement depth are plotted. The Bouguer gravity is calculated from the free-air gravity by subtracting the attraction of the rock-water interface assuming that structures are two-dimensional. The dotted lines in (a)–(e) are the predicted free-air gravity, Bouguer gravity (with and without the sinusoids), topography, and Moho geometry from the simple locked-fault model for an 11 My age offset. The dashed lines in (a)–(e) are the free-air gravity, Bouguer gravity (with and without sinusoids), bathymetry, and Moho geometry predicted by assuming that a second fracture zone with a left-lateral offset is located approximately 50 km south of the northernmost scarp. Age offsets of 16 and 5 My are assumed for the northern and southern scarps, respectively, and the age of the northern plate is 47 Ma. The actual bathymetry rather than the theoretical bathymetry was used in calculating the free-air anomalies.

Farallon relative motion vector at the time of crustal formation at 27 to 35 Ma, but the overall trend of the entire system of transforms is a relict from the former direction of relative motion before the clockwise rotation at 35 Ma (Figure 2-9c). Based on the magnetic lineations north and south of the fracture zone, the age offset across the entire fault system is 11 My, but no single scarp shows the predicted 1.2 km of relief for that age offset. Rather, our Hydrosweep bathymetry data indicate that here the fracture zone is split into 3 right-lateral offsets within a distance of 70 km, and three flexural scarps now accommodate the relative vertical motion (Figure 2-10c). The Bouguer gravity data shows the gravity high expected from the locked-fault model for 2 of the 3 north-facing scarps (Figure 2-10b), but the expected amplitude is only a few mGals for offsets this small and close together.

Of the 4 regions examined, only in Area 2 was it necessary to remove the long-wavelength signal from the crossgrain gravity rolls despite the fact that these features also intersect the fracture zone further east in Area 1 and further west in Area 3. Although it is not clear in Figure 2-1 exactly what the expected signal from the crossgrain lineations would be in Areas 1 and 3 on account of superposition of noise from seamounts and other topographic features, as long as the gravity rolls intersect the fracture zone near a node in the oscillation, this unwanted signal is removed when the Bouguer gravity data are used to fine-tune the step.

## 2.5 Discussion and conclusions

Along each of the eight geophysical cross-sections of the MFZ sampled during our expedition, we observed at least some vestige of the ridge-trough morphology that is the hallmark of compensation for the relief produced at the RTI via flexure across a locked fracture zone [Sandwell and Schubert, 1982]. However, in three of the four areas we surveyed, modest changes in the pole of rotation between the Pacific and Farallon plates caused complications in the morphology of the fracture zone that

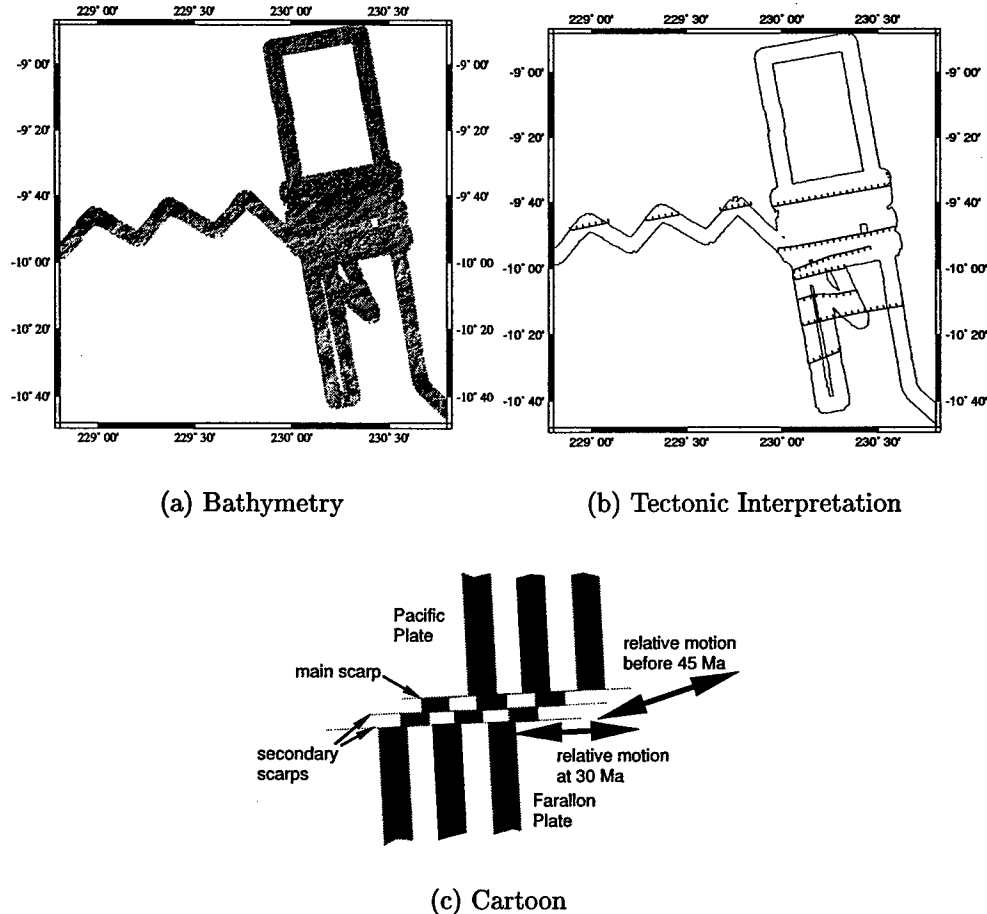


Figure 2-9: (a) Shaded relief map of Hydrosweep bathymetry from Area 1, illuminated from the southeast. (b) Interpreted tectonic features. Uplifted blocks trending N82°E represent the flexural scarps of the MFZ, here split into at least 3 strands over a distance of 70 km. The heavy stippled lines indicate the proposed locations of major right-stepping fracture zones. The thin stippled lines indicate the position of other coherent linear features visible in the Hydrosweep data. The direction of stippling indicates the scarp facing direction. The zig-zag track follows the northern scarp. (c) Cartoon of how this area presumably looked in plan view when it was an active plate boundary. The heavy double arrows show an exaggerated view of how the directions of relative motion of the Pacific plate relative to the Farallon plate both before and after the change in pole of rotation at 35 Ma relate to the trend of the individual transforms and the overall trend of the strike-slip region. [Cartoon by MKM]

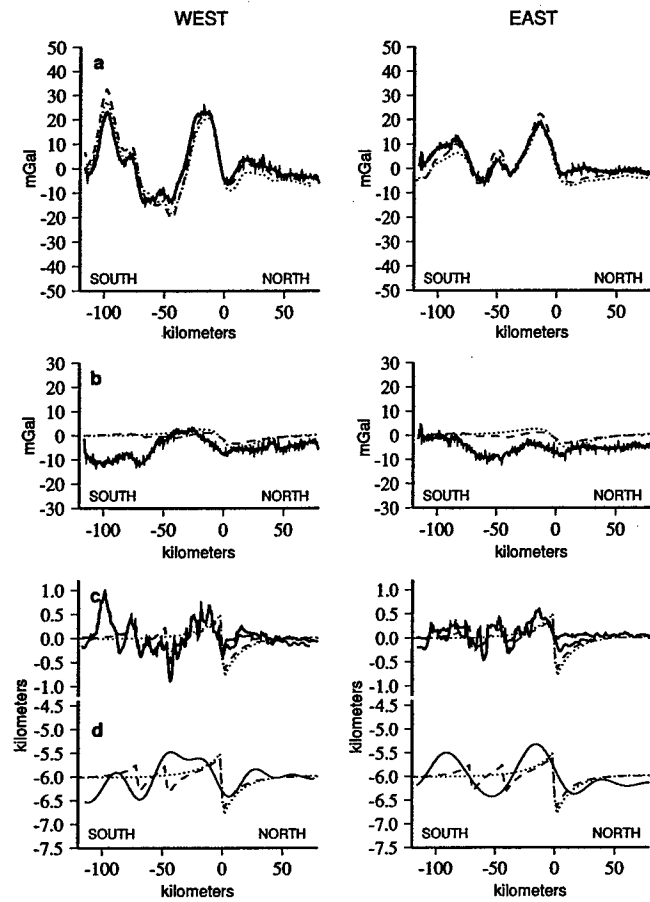


Figure 2-10: As in Figure 2-4, heavy solid lines show (a) free-air gravity anomaly, (b) Bouguer gravity anomaly, (c) bathymetry, and (d) predicted Moho geometry obtained from downward continuation of the Bouguer gravity along the two long north-northwest-south-southeast profiles shown in Figure 2-9. The dotted lines show the predictions from the locked-fault model. The dashed lines show the predictions assuming that there are three fracture zones spaced at 45 km and 70 km south of the northernmost scarp. The northern side of the FZ is 37.5 Ma. The northernmost scarp has an age offset of 7 My while the southern 2 scarps have age offsets of only 2 My each.

obscured the flexural signal by creating multiple offsets from tension or overthrusting from compression within the transform regime. High-resolution bathymetry, gravity, and seismic data are required to sort out these plate-tectonic complications, and thus it is no wonder that only about half of the satellite altimetry passes over Pacific fracture zones show a signature consistent with flexure across a single locked fracture zone [D.T. Sandwell, pers. commun.]. Furthermore, we note that right-stepping fracture zones respond differently than left-stepping fracture zones to the same change in pole of rotation, with counterclockwise rotations of right-stepping transforms or clockwise rotations of left-stepping transforms being most effective in producing small gravity anomalies that might be interpreted as evidence for a weak fault. This aspect may explain why *Bonneville and McNutt* [1992] found that the left-stepping Molokai fracture zone appears anomalously weak compared with its right-stepping neighbors, the Murray, Clarion, and Clipperton fracture zones. One unfortunate corollary of our conclusion that changes in rotation poles can obscure the signal from flexure across fracture zones is that those fracture zones with large age offsets, and thus the ones predicted to have the largest flexural signal, are also least likely to contain sections of the fault that never were subjected to a change in rotation pole while the plates were within the active transform. The only section of the MFZ to preserve an unambiguous flexural signal (apparent even in the satellite data), Area 3, was created in the Paleocene during a time of no change in the location of the Pacific-Farallon pole. This aspect may explain why the *Sandwell and Schubert* [1982] model has not been successfully applied to the large-age-offset Atlantic fracture zones, where the morphology is dominated by the record of shifts in relative plate motion [*Tucholke and Schouten*, 1988].

Geophysical modeling indicates that the MFZ maintains the vertical shear stresses necessary to support the topographic offset created at the RTI for at least 60 Ma. In Area 3, the vertical shear stress reaches 20 MPa, a stress value much higher than the stress drop of a typical earthquake but much smaller than the integrated strength of

intact lithosphere based on modeling with yield strength envelopes. The fact that we find no evidence for release of the shear stress along the fault is consistent with the recording of only one small earthquake along the fracture zone.

Our geophysical cross sections were located midway between hot spot crossings of the fracture zone to avoid as much as possible influence from the heating of the hot spot on the strength of the fracture zone. We find abundant evidence for hot spot volcanism along the fracture zone, in the form of volcanic cones erupted along the intersection of the MFZ with the hot spots that created the Tuamotu and Society hot spots. The Marquesas hot spot presently lies directly beneath the fracture zone, but clearly the heat from the Marquesas hot spot has not yet weakened the fault to release the shear stress where they intersect. Whether it is likely to do so in the future awaits analysis of gravity and seismic data from the older intersection of the fault with the Society hot spot to determine if a flexural scarp is buried beneath its archipelagic apron.



## Chapter 3

# Pacific-Farallon Relative Motion 42-59 Ma Determined from Magnetic and Tectonic Data from the Southern Austral Islands

I quickly outgrew ideas. So I distrusted experts, who were often intelligences confined within high walls, knowing indeed every paving-stone of their prison courts: while I might know from what quarry the stones were hewn and what wages the mason earned. I gainsaid them out of carelessness, for I had found materials always apt to serve a purpose, and Will a sure guide to some one of the many roads leading from purpose to achievement. There was no flesh.

T. E. Lawrence, *The Seven Pillars of Wisdom*

### Abstract

We have used recently collected magnetic profiles and high resolution multibeam bathymetry data near the southern Austral Islands in French Polynesia to constrain the relative motion of the Pacific and Farallon plates between chron 25 and chron 18 (42–59 Ma). A change in plate motion at about chron 21 (50 Ma), which reoriented spreading direction in the area by 10–12° clockwise was apparently accommodated by a southward propagating rift which transferred 160 km of Pacific crust to the Farallon plate, the outer pseudofault of which is preserved as the Adventure Trough. These new constraints significantly revise previous estimates of Pacific-Farallon relative motion at the crucial time period encompassing the bend in the Hawaiian-Emperor chain, believed to represent an abrupt change in the absolute motion of the Pacific plate. Disrupted lithosphere at the Adventure Trough has apparently been a preferred site for later midplate volcanic activity.

### 3.1 Introduction

Many of the principal tectonic features of the South Pacific were first identified by *Handschrumer* [1976]. *Engebretson et al.* [1984], *Pardo-Casas and Molnar* [1987] and *Rosa and Molnar* [1988] compiled magnetic anomaly identifications and fracture zone locations available at the time to produce histories of relative plate motions in the Pacific. *Mayes et al.* [1990] developed a self-consistent model for South Pacific plate motions (Pacific-Farallon/Nazca, Pacific-Antarctic/Bellinghausen, etc.) with the aid of Geosat exact repeat data to identify tectonic features. After these compilations had appeared, *Cande and Haxby* [1991] identified the Adventure Trough as the trace of a propagating rift extending 1200 km through Eocene Pacific crust. *Cande and Haxby* [1991] also compiled magnetic anomaly data for the conjugate portion of the Nazca plate, and concluded that *Mayes et al.* [1990] and *Cande et al.* [1989] had both overestimated the age of Nazca crust currently entering the Chile Trench by as much as 30 m.y. by assuming symmetrical spreading at the Pacific-Farallon spreading center (and no ridge jumps or propagating rifts).

This study addresses the Eocene change in Pacific-Farallon relative plate motion [*Caress et al.*, 1988] with data from a study region flanking the southern Austral Islands, a midplate volcanic chain in French Polynesia.

### 3.2 New constraints on Pacific-Farallon spreading

The seafloor in the region of the southern Austral Islands was formed at the Pacific-Farallon spreading center from about 40-60 Ma. The Pacific-Aluk-Farallon triple junction trace (TJT) marks the westward boundary of Pacific-Farallon crust, and most of the Austral Islands lie on the spreading segment between the Austral Fracture Zone to the north and the Resolution Fracture Zone to the south (see Figure 3-1). However, this segment was disrupted at about chron 21 (50 Ma), apparently by a propagating rift which transferred some hundreds of kilometers of lithosphere from

the Pacific plate to the Farallon plate, leaving behind the long oblique scar that is the Adventure Trough (hereafter referred to as AT) [Cande and Haxby, 1991]. In the study area (Figure 3-2), the AT is a zone approximately 50 km wide with multiple scarps.

We have used the orientation of the abyssal seafloor fabric as a proxy for spreading direction in two subregions, one on seafloor of age chron 22-24, the other of seafloor younger than chron 19. The mean and mode of the direction of the maximum topographic gradient were computed [Mardia, 1972] in the following manner. A topography grid was constructed from multibeam bathymetry of the area shown in Figure 3-2(a), collected by *R/V Maurice Ewing* (Hydrosweep) and *F/S Sonne* (SeaBeam). Seafloor with depths less than 4000 meters has been omitted, as it is likely to consist of constructional volcanic features not reflecting original spreading direction. Only slopes greater than the mean seafloor slope in the region (0.10) are included, excluding 65% of the data with low slopes. Additionally, the highest 5% of slope values were omitted to reduce noise from spurious high slope values. Resulting slope distributions are shown by rose diagrams in Figure 3-3a & b. In the southeastern box in shown in Figure 3-2, the mean and mode of the maximum gradient were both N75°E. In the northeastern box, on seafloor formed subsequent to the AT propagation, the modal direction was N87°E and the mean was N89°E. Examples of the spreading fabric are shown in Figure 3-3b & c. The spreading direction obtained by this method is similar to the orientation of the Austral Fracture Zone located 500 km to the north, as well as very close to relative plate motions of *Rosa and Molnar* [1988], as discussed later.

Half spreading rates for the study region were computed for chron 25-22 and for chron 20-18 by projecting our magnetic anomaly picks onto the azimuths calculated from the abyssal seafloor direction. For consistency, following *Mayes et al.* [1990] we have used the time scale of *Berggren et al.* [1985] for the ages of all magnetic anomalies used in calculating spreading rate. Predicted spreading direction calculated from the

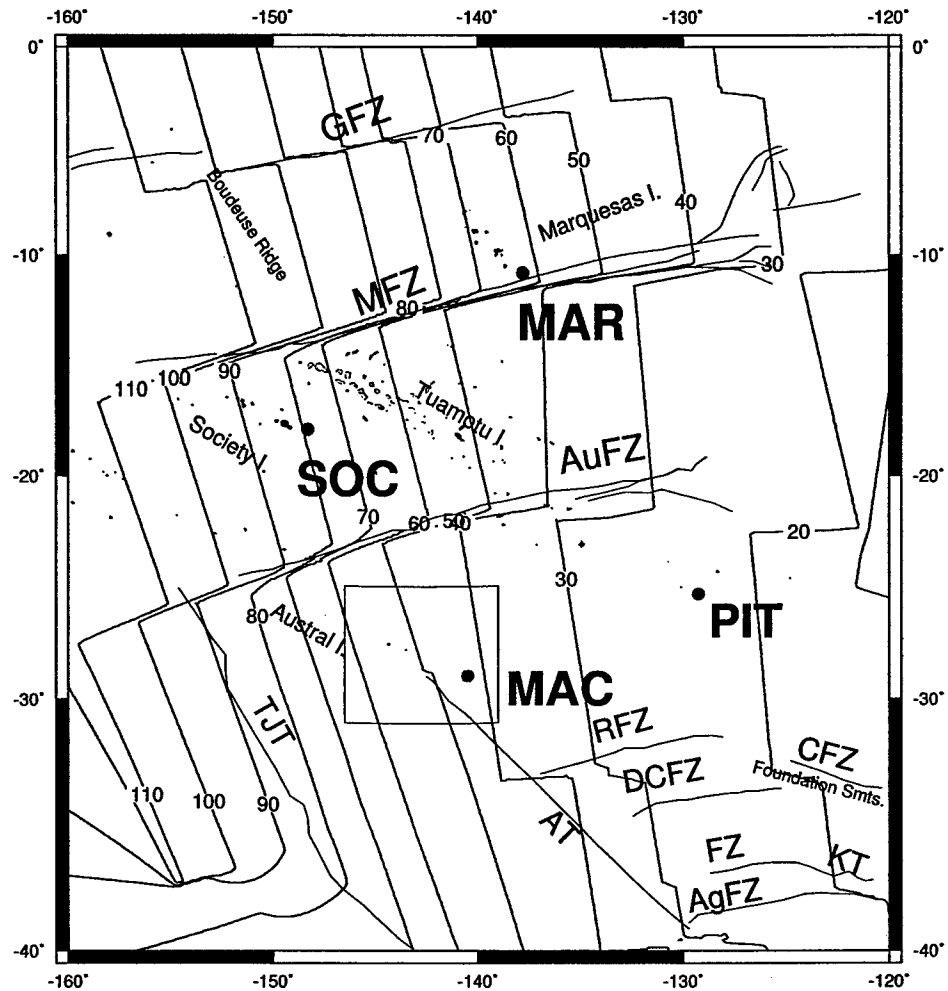


Figure 3-1: Simplified tectonic map of the South Pacific. Numbered contours indicate age of seafloor in Ma, from digital age map of Müller *et al.* [1997]. Locations of labelled features are digitized from satellite gravity map: GFZ=Galapagos Fracture Zone, MFZ=Marquesas FZ, AuFZ=Austral FZ, RFZ=Resolution FZ, DCFZ=Del Cano Fracture Zone, FZ=unnamed fracture zone, AgFZ=Agassiz FZ, CFZ=Chile FZ, AT=Adventure Trough [Cande and Haxby, 1991], KT=Kurchatov Trough, TJT=Pacific-Aluk-Farallon triple junction trace. Grey circles indicate the locations of Marquesas (MAR), Society (SOC), Pitcairn (PIT) and Macdonald (MAC) hotspots, from north to south, respectively. The study area shown in Figure 3-2 is indicated by a box.

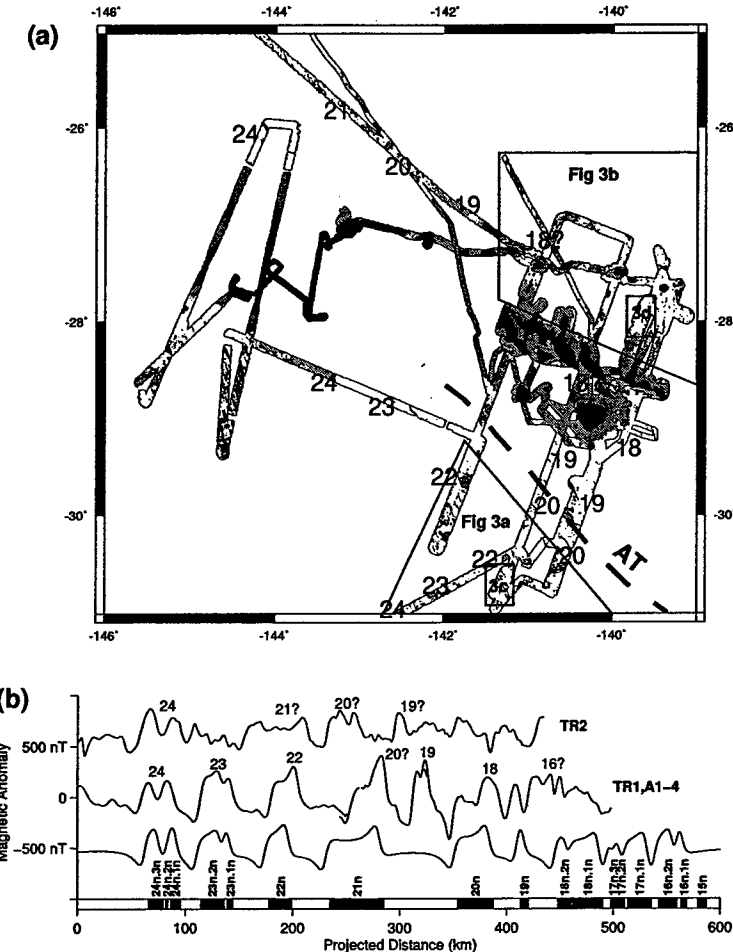


Figure 3-2: (a) Composite map of study region showing seafloor fabric, constructional volcanics, and magnetic anomaly picks. Bold outline shows region of multibeam bathymetry data coverage. Areas with data shallower than 3500 m are shaded dark gray, and between 3500 m and 4000 m shaded light gray. Points in the abyssal region with higher than average local topographic slope are plotted as black. Thick dashed line labelled AT indicates the location of the main scarp of the Adventure Trough. The morphological expression of the AT is a series of scarps in a zone nearly 50 km wide. Regions used to compute histograms in Figure 3-3a & b are indicated, as well as regions shown in Figure 3-3c & d. (b) Observed magnetic anomalies (top two profiles) of northernmost and southeasternmost survey lines, projected perpendicular to mean spreading direction and model magnetic anomaly (bottom profile) created from magnetic polarity timescale of *Cande and Kent* [1995], shown below.

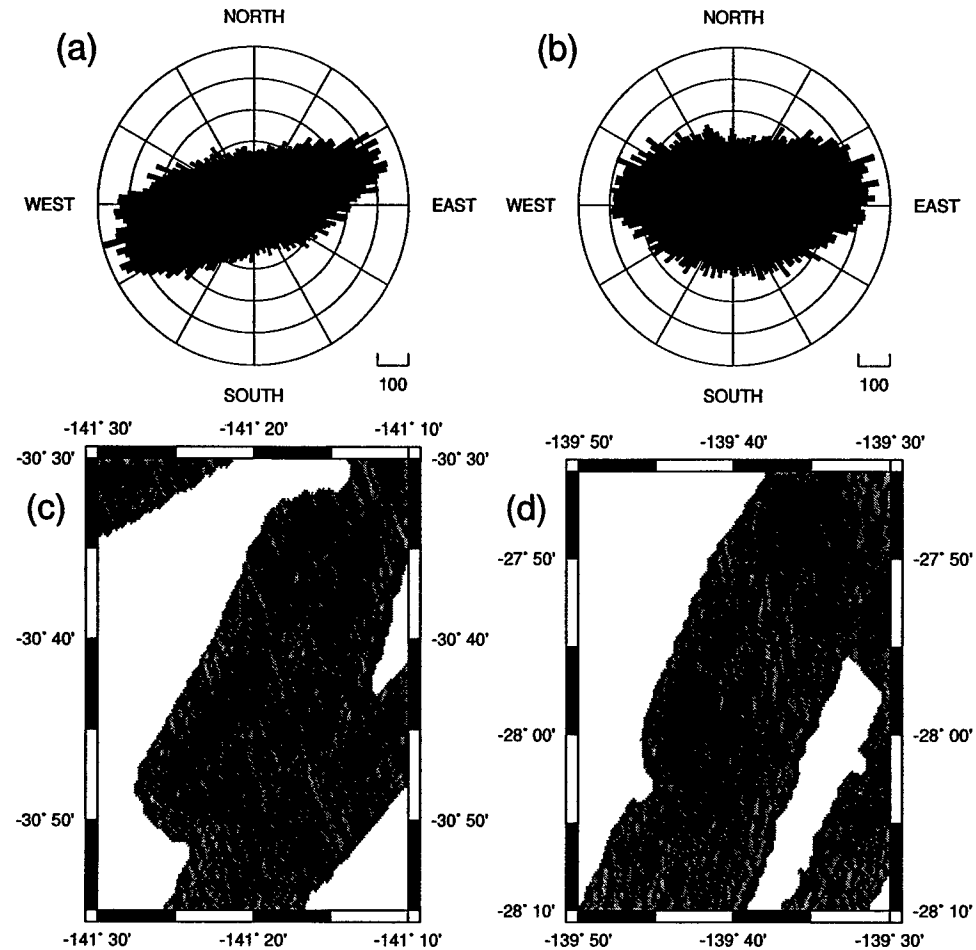


Figure 3-3: Seafloor fabric orientation in the study area. Rose diagrams of maximum gradient of topography grid, constructed with multibeam bathymetry data consisting of EW9602 Hydrosweep data and SO-47 Seabeam data gridded to 200 m spacing. Points corresponding to depths  $> 4000$  m and  $0.1 < \text{slope} < 0.3$  are included, as described in the text. (a) South of volcanics and Adventure Trough ( $N = 46,153$ ). Modal direction is N75°E. This seafloor was formed prior to chron 21. (b) North of volcanics ( $N = 52,072$ ). Modal direction is N87°E. This seafloor was formed after chron 18. (c) Shaded relief bathymetry data from a region southwest of AT, as shown in Figure 3-2a. Illumination is from the east. (d) Shaded relief bathymetry data from a region northeast of volcanics and AT, as shown in Figure 3-2a.

stage poles of *Rosa and Molnar* [1988] are nearly identical to our observed seafloor fabric directions, and would not change our calculated spreading rates appreciably.

*Rosa and Molnar*'s [1988] Pacific-Farallon rotations predict that the half spreading rate in the region was 15 mm/yr west of the AT and increased to over 27 mm/yr to the east (after chron 21, see Table 1). In contrast, our observations show that the spreading rate was more nearly the same on either side of the AT, and in fact slightly higher before chron 21. The 10° change in azimuth predicted by the stage poles of *Rosa and Molnar* [1988], however, are confirmed by our observations. On the other hand, spreading rates computed from the finite rotations of *Mayes et al.* [1990] match fairly closely the observed spreading rates in the Austral region, but predict no change in spreading direction until chron 13. The finite rotations of *Engebretson et al.* [1984] also predict a clockwise rotation at chron 21, but their azimuths are more than 10° off from our observed seafloor fabric directions, and they predict an increase in spreading rate, not a decrease as observed, at the same time. Our data and method place tight constraints on the direction of Pacific-Farallon motion and provide good information on spreading rates, but cannot determine the time of the relative motion change more precisely. We propose that this change happens at the time of AT propagation, but our data are not sufficient to determine this with certainty.

Table 3.1: Predicted and observed spreading rates and azimuths in study region

Source	chron 25-chron 21		chron 21-chron 18	
	$\frac{1}{2}$ rate (mm/yr)	Azimuth	$\frac{1}{2}$ rate (mm/yr)	Azimuth
<i>Rosa and Molnar</i> [1988]	15.4	71.5°	27.5	81.6°
<i>Mayes et al.</i> [1990]	26.5	75.0°	19.1	75.0°
this study	28	75°	22	87°

### 3.3 The structure of the Adventure Trough

Within the survey area, the Adventure Trough is not expressed as a deep (as it is at some other locations) but rather as a series of scarps. As many as three southwest facing scarps can make up the feature (Figure 3-4). The principle orientation of the AT is N40°W, or 25° counterclockwise from the abyssal hill orientation (Section 3.2).

Although the thermal boundary conditions across a pseudofault are similar to those across a fracture zone (see Chapter 2), the tectonic setting of the two kinds of features are quite different. From thermal considerations alone, one might expect that if a pseudofault does not relieve vertical stresses it would evolve as in Figure 2.3. Indeed, at least one of the 4 profiles across the AT resembles the locked-fault FZ model (profile A9, shown at bottom left in Figure 3-4). However, most of the AT scarps show little resemblance to the flexurally dominated model. Most likely, the tectonic effects of rifting the ocean lithosphere produce a topographic signal that swamps the flexural one.

To address the question of the structure of the old propagating rift, we turn to two geophysical tools. Shipboard gravity data and multichannel seismic reflection data were collected by EW9602 on crossings of the AT in four different locations. This provides additional independent constraints on the crustal structure of a pseudofault on old lithosphere.

The apparent crustal thickness (see Section 4.2.1 for details) for the AT crossings is plotted at the right side of Figure 3-4. No useful Moho observations were made across the AT in profile A3. On line A5, there seems to be significant crustal thinning at the main scarp at  $x = -20$  km. Profile A7 shows a general thickening towards the center (assuming no lateral velocity variations; see Section 4.2.1), which is probably related to volcanic effects. This line is much closer to the center of the Macdonald volcanic line than the other profiles, and there may be signs of constructional volcanism at the pseudofault itself (near  $x = 0$  on the third row of Figure 3-4). To the northwest of this feature, a large positive ridgelike structure is apparent in the satellite gravity

data, which we guess is constructional.

Care must be taken in interpreting the reflection Moho represented in Figure 3-4, as no detailed velocity information is available across the scarps. Variation in apparent crustal thickness may be due either to actual crustal thickness variations or to lateral changes in crustal velocity structure.

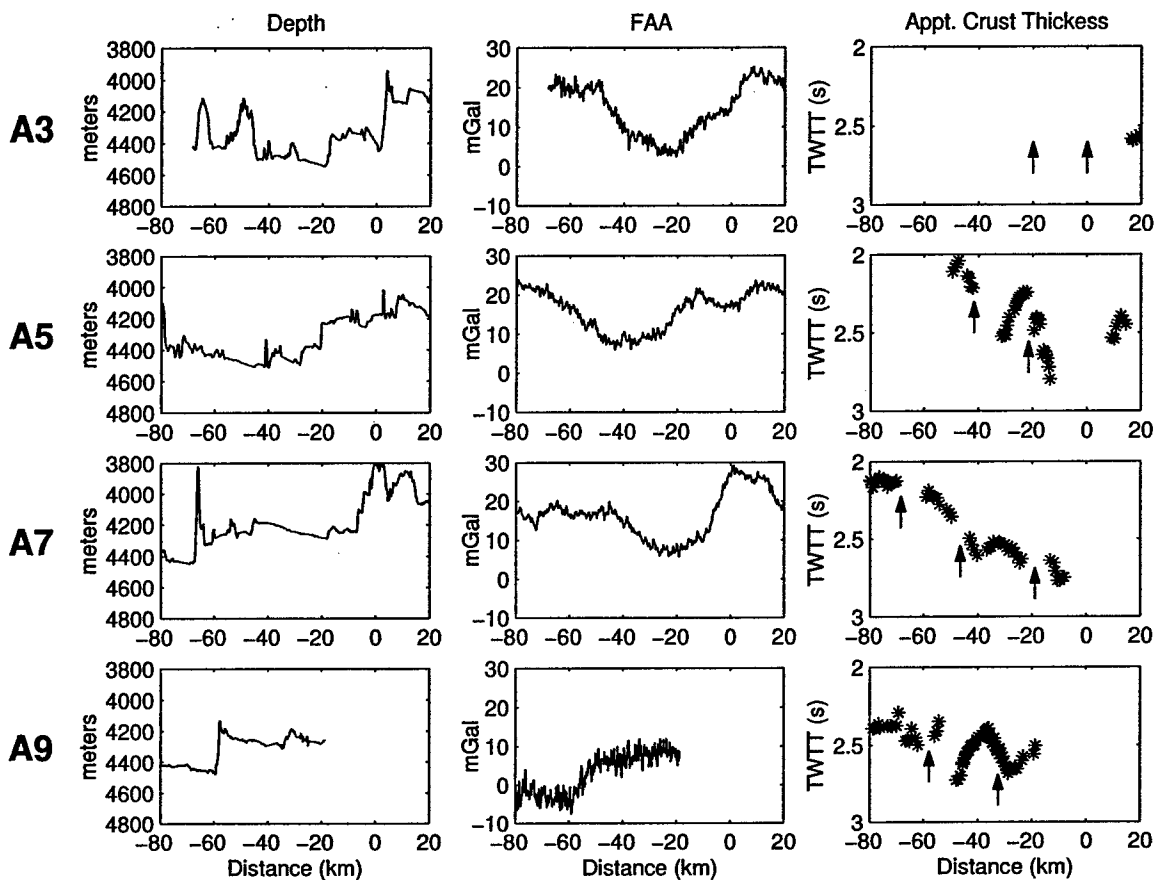


Figure 3-4: Bathymetry, gravity and seismic Moho profiles across the Adventure Trough, projected along an azimuth of N50°E (perpendicular to the mean trend of the AT). Left column of panels shows hydrosweep centerbeam depth across the AT, showing the locations of multiple scarps. Center column of panels is free air gravity anomaly for the same profiles, and the left column shows apparent crustal thickness from seismic Moho observations (see Section 4.2.1). Shown are lines A3, A5, A7 and A9, from top to bottom. The data for seismic lines A5, A7 and A9 are shown in Figures B-4, B-5 and B-6, respectively. The location of tectonic scarps in each profile is shown in the rightmost panels by arrows.

### 3.4 Discussion

The Southern Austral region has been the site of multiple episodes of volcanic activity [McNutt *et al.*, 1997]. The first episode was approximately 25-35 Ma, and produced widespread volcanic activity on ocean lithosphere that was less than about 10 m.y. old. The most recent episode has been taking place since about 6 Ma, and is exemplified by the current volcanic activity at Macdonald Seamount. This younger episode is in at least one location (Marotiri) overprinting a much older volcanic edifice [McNutt *et al.*, 1997]. Such overprinting suggests that preexisting crustal structure influences the location of later volcanism. The trace of the Adventure Trough, which extends 1200 km to the southeast, is obscured at its intersection with the Austral Island chain, where it merges into a large ridgelike structure. We suppose that this is a constructional volcanic ridge formed along a line of disrupted lithosphere. That the only two emergent islands in the study region (Rapa and Marotiri) occur at the intersection between the AT and the Austral chain is also suggestive of a lithospheric structural control on the location of volcanism in the region.

A clockwise change in spreading direction such as we have observed here would have placed right-stepping transform faults on the Pacific-Farallon spreading center (such as at the Austral and Marquesas fracture zones) into extension. Features associated with a “leaky” transform are observed at the Marquesas Fracture Zone, though apparently at a somewhat later time than observed in this study [Kuykendall *et al.*, 1994; Jordahl *et al.*, 1995]. This discrepancy in time may be due to the wide spacing of survey areas of Jordahl *et al.* [1995] causing extensional features west of 135°W to be overlooked. Such features may be observed in recent satellite altimetry maps [Smith and Sandwell, 1995] as far west as 140°W on the Marquesas Fracture Zone, and possibly on the Austral Fracture Zone as well.

The discrepancy in our observed relative motions with those predicted by previous studies of Pacific-Farallon motion is of some interest. The data used by Rosa and Molnar [1988] were sparse in the South Pacific, and the Adventure Trough had not

yet been identified as a propagating rift [*Cande and Haxby, 1991*]. *Mayes et al.* [1990] used satellite altimetry and published magnetic anomalies to reconstruct a self-consistent tectonic history of the entire South Pacific, but they allowed for no change in Pacific-Farallon spreading orientation (although they allowed the rate to change) from chron 34 to chron 13. *Tebbens and Cande* [1997] have used more recent data in the southeast Pacific to improve Pacific-Farallon relative motion since chron 13, but relative motions before that time are, as this study shows, still inadequate. There has been sufficient increase in data available for the South Pacific in the last ten years [e.g., *Kruse, 1998*, *Cande and Haxby, 1991*, *Kuykendall et al., 1994*] to justify a resynthesis of plate motions before chron 13. These older reconstructions have recently been used to argue against a change in absolute plate motion at the Hawaiian-Emperor bend [*Norton, 1995*]. A new interpretation of existing data, together with new techniques for testing absolute plate motions [e.g., *Wessel and Kroenke, 1997*] will help to test this hypothesis and others.



# Chapter 4

## History of Volcanic Loading of the Southern Austral Islands

We may now consider that we have nearly crossed the Pacific. It is necessary to sail over this great ocean to comprehend its immensity. Moving quickly onwards for weeks together, we meet with nothing but the same blue, profoundly deep, ocean. Even within the archipelagoes, the islands are mere specks, and far distant one from the other. Accustomed to look at maps drawn on a small scale, where dots, shading, and names are crowded together, we do not rightly judge how infinitely small the proportion of dry land is to water of this vast expanse.

Charles Darwin, *Voyage of the Beagle*

### 4.1 Introduction

The Cook-Austral island chain (see Figure 4-1) is one of the more enigmatic midplate linear volcanic features [e.g., *Okal and Batiza, 1987*]. Although the trend of the chain agrees well with absolute plate motions relative to a hotspot reference frame obtained from Hawaii and other hotspot tracks [*Duncan and Clague, 1986*], the age distribution along the chain is complex and does not increase monotonically to the northwest, as does Hawaii. For example, Rarotonga, over a thousand kilometers to the northwest of the assumed location of the hotspot at Macdonald Seamount, has been dated at 1.1–2.3 Ma [*Turner and Jarrard, 1982*], much younger than would be possible if produced by a single stationary hotspot now located beneath Macdonald. Also,

several guyots, presumably older than about 40 Ma, are known to exist intermingled with the relatively young islands of the Austral Chain [Menard, 1964; Johnson and Malahoff, 1971]. At least three hotspots are necessary to explain the ages of just the subaerial volcanism in the Cook-Austral chain [Turner and Jarrard, 1982]. When the submarine volcanoes are included, the situation is even less well described by hotspot theory [McNutt *et al.*, 1997].

#### 4.1.1 Morphology of the Cook-Austral chain

The Cook-Austral chain consists of two parallel intermittent linear features separated by 250 km for much of its length [Turner and Jarrard, 1982]. The southeastern (and youngest according to a hotspot model) part of the chain, terminating at Macdonald Seamount, consists of a chain of islands and seamounts stretching for 700 km from Macdonald to near Neilson Reef (see Figure 4-1). Macdonald Seamount itself is a rather isolated feature, its summit is currently 39 meters below the sea surface, and it is the site of active volcanism [Stoffers *et al.*, 1989].

From Président Thiers Reef to Palmerston Atoll more than 1500 km to the northwest, the Cook-Austral chain is a series of islands and seamounts parallel to but laterally offset by 250 km from the Macdonald segment of the chain (see Figure 4-1). The character of the chain seen in the Geosat map here is not that of linear features as near Macdonald, but discrete volcanic edifices. There are also signs of features along the Macdonald-Neilson trend farther to the northwest, notably Mangaia and Rarotonga, as well as numerous smaller features visible in the Geosat map. Exceptionally young (<2 Ma dated by K/Ar) rocks have been recovered on islands very far from Macdonald, including Rurutu and Rarotonga [Turner and Jarrard, 1982].

In the study region of the southern Australs discussed in this chapter (Figure 4-2), three distinct chains of volcanoes can be delineated [McNutt *et al.*, 1997]. The northernmost, the Taukina line, is made up of small, discrete edifices, often topped with a summit caldera, similar in morphology to near-axis seamounts at the East Pacific

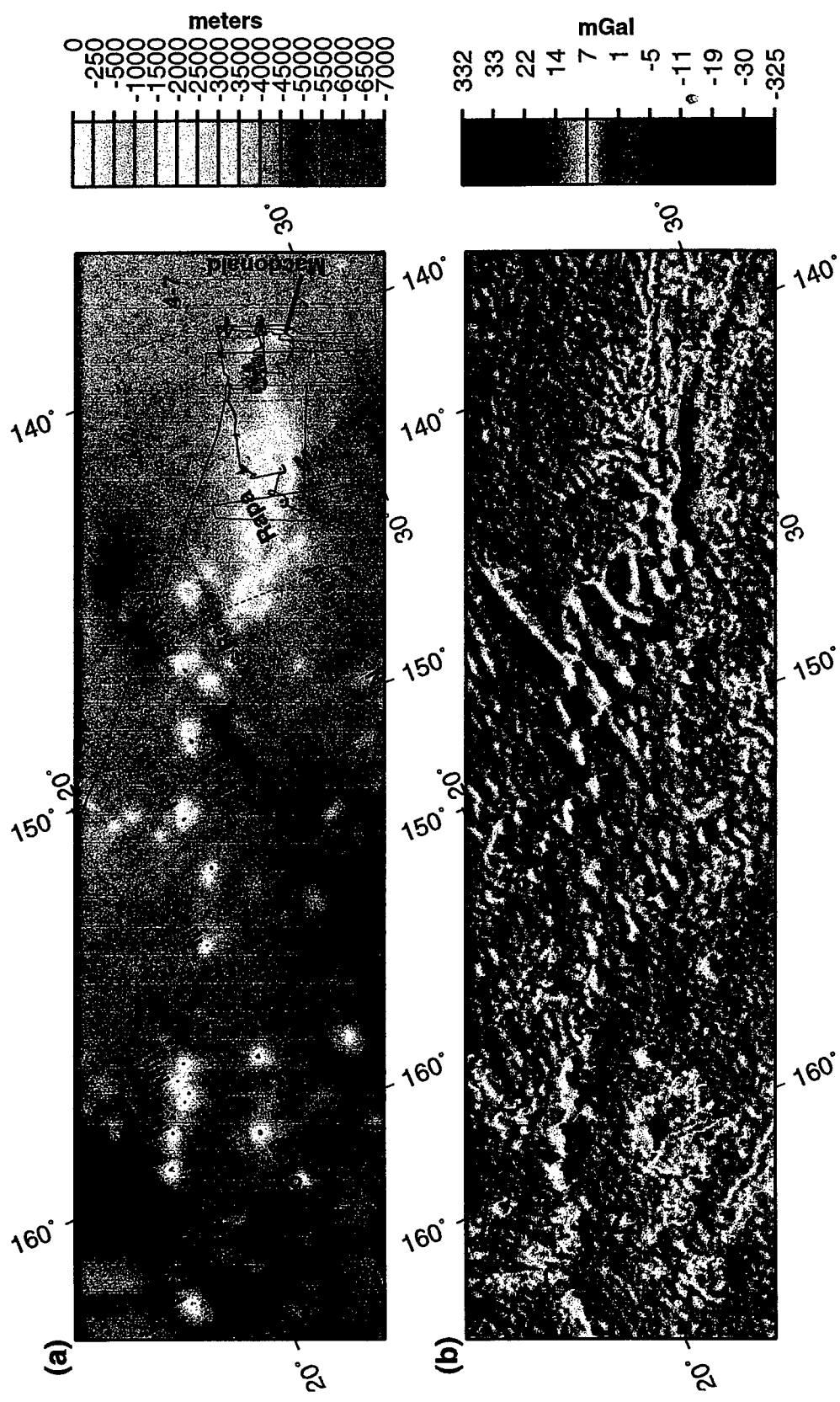


Figure 4-1: (a, top panel) ETOPO5 bathymetry map of the Cook-Austral region. Map is an oblique Mercator projection about the pole of rotation of the Pacific plate with respect to fixed hotspots from the finite rotation pole of *Duncan and Clague* [1986]. Names of islands and prominent submarine features are shown, as well as the ship track of EW9602. The regions shown in more detail in Figures 4-2 and 4-7 are shown by the dashed boxes. (b, bottom panel) Free air gravity anomaly map of the region shown in (a) from declassified Geosat geodetic mission and ERS-1 altimetry data [Smith and Sandwell, 1995]. Shaded relief, illumination from the north.

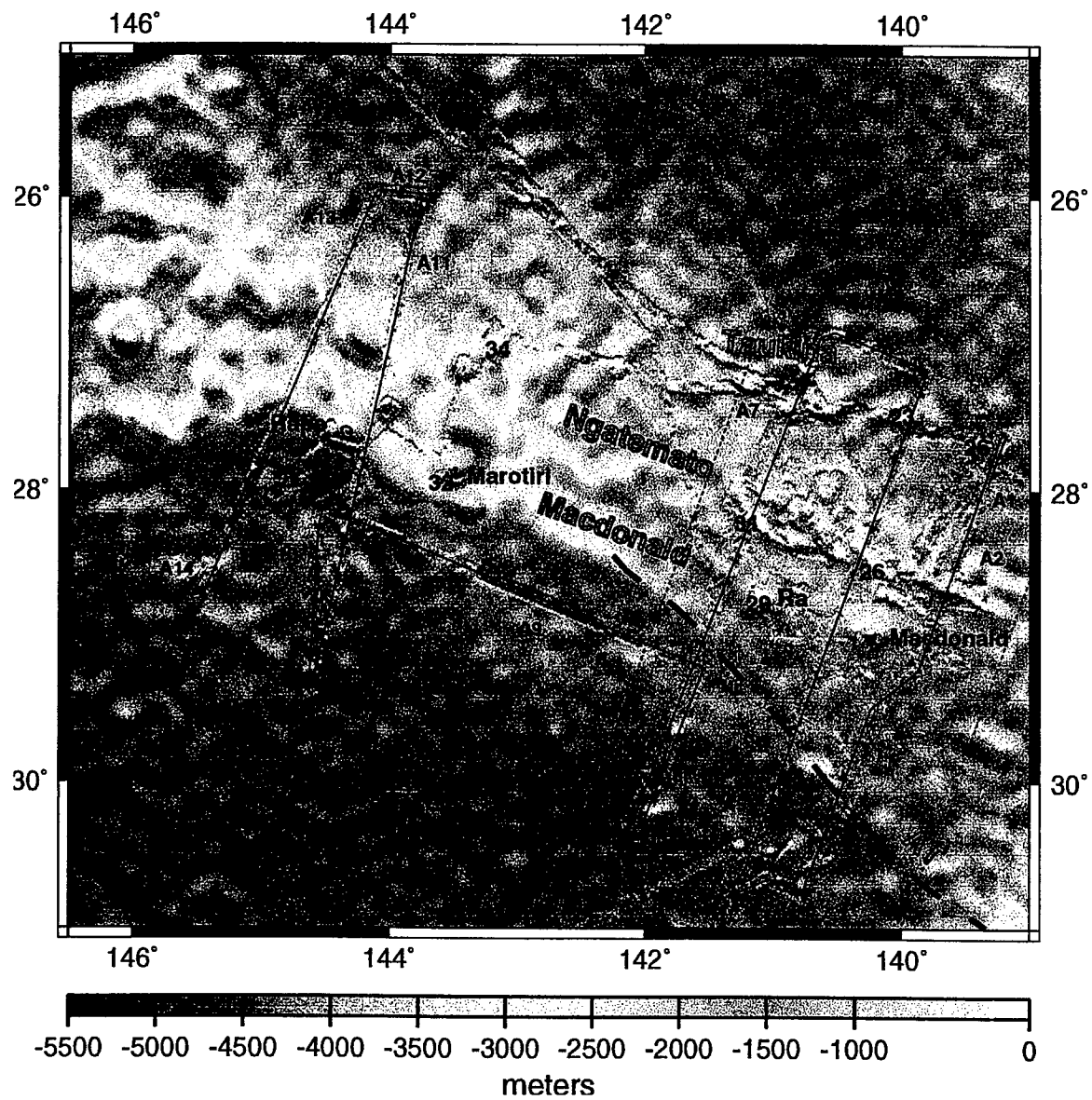


Figure 4-2: Bathymetry of the study area, from multibeam shipboard data from EW9602 and SO-47, overlaid on bathymetry predicted from shipboard data and satellite altimetry [Smith and Sandwell, 1997]. Seismic lines A1–A14 are indicated, and dated dredge samples are indicated with the age in Ma [McNutt *et al.*, 1997]. The three volcanic chains discussed in the text are labeled, and the Adventure Trough is the heavy dashed line labeled “AT”. The model domain used for flexural studies in this chapter is indicated by a light dashed line.

Rise [Scheirer *et al.*, 1996]. The Ngatemato line consists of broad, low, en echelon volcanic features made up of many discrete cones, which also occur on the seafloor nearby in a 75 km swath [Caress *et al.*, 1997]. The Ngatemato chain can be seen in satellite gravity data to continue to the southeast, beyond the region near the Austral Islands mapped by multibeam sonar systems, for hundreds of kilometers, joining with the Foundation Seamounts [Mammerickx, 1992; see also Figure 1-1]. The en echelon nature of the chain is similar to the Puka Puka ridges described by Sandwell *et al.* [1995] and the Tahiti-Easter seamount chain [Searle *et al.*, 1995]. These three chains span the Superswell region of the South Pacific from the East Pacific Rise to over 60 Ma lithosphere.

The third line of southern Austral seamounts is the Macdonald line, including the largest seamounts and some emergent islands. Macdonald and Ra Seamounts and Marotiri and Rapa Islands are all large, discrete edifices on this trend. A suite of samples from these features have been dated in a monotonically increasing series from Macdonald to Rapa which is consistent with the movement of the Pacific plate over a stationary hotspot [Turner and Jarrard, 1982]. However, much older samples have been dredged from the lower part of the edifices of Ra and Marotiri [McNutt *et al.*, 1997]. The Macdonald chain has apparently interacted with and possibly reactivated older volcanoes.

#### 4.1.2 Tectonic setting

Macdonald seamount sits on ~45 Ma seafloor [Cande and Haxby, 1991]. The Austral Islands cross the Austral Fracture Zone (AFZ, with age offset ~10 m.y.) near the island of Raivavae (see Figure 3-1). It has been suggested that the AFZ is a boundary between different source chemistries of the Austral basalts [Lassiter *et al.*, 1998]; however, the full lead isotopic variation of the Austral Islands basalts has been observed in a single melt inclusion by Saal *et al.* [1998]. Although there is no obviously fracture-zone-related effect on the morphology of the island chain as seen in

the ETOPO5 bathymetry, there are fracture-zone-parallel lineations visible in gravity anomaly maps.

From bathymetric profiles and satellite gravity data, *Cande and Haxby* [1991] identified a large linear feature south of the Austral Islands, oblique to both hotspot and fracture zone trends, which they named the Adventure Trough (see Chapter 3). On the basis of its morphology and a discontinuity of magnetic anomalies across the feature, they have interpreted this feature as the site of propagating rifts, ridge jumps and asymmetrical spreading which accounts for approximately 300 km of missing Pacific seafloor. This missing lithosphere must have been transferred to the Farallon plate, and about 50 km of it has been observed south of the Challenger FZ on what is now the Nazca plate. The signal of the Adventure Trough is present in the gravity data only south of the Austral Islands, but the morphology of the island chain is complicated near the location of its intersection with the trough feature, perhaps due to volcanic reactivation of existing structures in the ocean lithosphere caused by the ridge propagation associated with the trough.

#### 4.1.3 Elastic properties of the lithosphere

Previous studies have indicated an anomalously low value of the flexural rigidity of the lithosphere beneath the Cook-Austral Islands [*Calmant and Cazenave*, 1986]. Studies of the elastic thickness beneath the Marquesas and Society Islands have shown higher values when more dense ship tracks are included [*Filmer et al.*, 1993] than when based on gridded bathymetric databases alone [*Calmant and Cazenave*, 1986; *Calmant*, 1987]. Thus, the low value of the elastic thickness obtained by *Calmant and Cazenave* [1986] for the Cook-Austral Islands may have been similarly biased. In fact, this is an area of even more sparse ship tracks, which implies that the digital bathymetry database on which they based their results is even less well controlled than for other island chains and prone to greater errors in interpretation [*Smith*, 1993]. More accurate assessment of the elastic plate thickness beneath the Cook-

Austral chain requires more accurate bathymetry of the area. Moreover, multiple episodes of volcanism in close proximity and even overlapping is sure to bias simple estimates of elastic plate thickness. Improved bathymetry mapping of the Southern Austral Islands from cruise EW9602 is used below for modeling the elastic thickness of the lithosphere.

In this chapter, several geophysical observational tools are used to investigate the structure of the southern Austral region. Two-dimensional elastic plate modeling is used to constrain the volume and age of the seamounts and the flexural rigidity of the lithosphere. Seismic, gravity and elastic modeling methods for estimating crustal thickness yield consistent results, indicating that the older, lower seamounts are more important volumetrically than the younger, apparently larger ones.

## 4.2 Data collection and processing

### 4.2.1 Multichannel seismic data

Multichannel seismic data collected by *R/V Maurice Ewing* cruise EW9602 consists of 5 lines perpendicular to the trend of the volcanic chains, each about 200 km long, one long ( $\sim$ 200 km) line parallel to the trend of the chains, and several short connecting lines (Figure 4-3). The seismic source was a 20 airgun array with a total source volume of  $8385 \text{ cm}^3$ . Shot spacing was nominally 50 m, and shot times were randomized to prevent coherent stacking of multiples. The multichannel seismic streamer consisted of 148 channels with a group spacing of 25 m. Data were recorded with a sample interval of 2 ms.

Data were binned to a common depth point (CDP) spacing of 12.5 m and stacked at Lamont-Doherty Earth Observatory. Frequency-wavenumber domain dip filtering was performed on the shot point data before gathering for better resolution of the seismic Moho. Several full seismic reflection profiles and corresponding Moho picks are shown in Appendix B, and a segment of line A5 is shown in Figure 4-4. The

apparent crustal thickness (two-way travel time difference between the water bottom arrival and Moho reflection) obtained from the digitized Moho reflection is displayed in an across-island projection in Figure 4-5.

The seismic Moho picks were converted to depth below seafloor with a simple velocity model. The crustal velocity information from stacking velocities and 1-D modeling of the sonobuoy data does not have sufficient resolution to be used for this purpose. An estimation method was devised based on a reasonable model of abyssal crustal thickness and the later addition of volcanic material. It was assumed that 6 km thick crust corresponds to 2 s of two-way travel time, and that any variations to this model is a result of crustal thickening with material of a constant seismic velocity. If the apparent crustal thickening in places is due to addition of volcaniclastic material to the top of the crust, the value could be as low as 3.5 km/s. However, the seismic data show very little volcaniclastic material in the region (less than about 0.2 s two-way travel time) almost everywhere that the basement can be imaged. A value of 7 km/s for any additions to the abyssal crustal thickness is probably more accurate, and was used for seismic crustal thickness calculations. It should be noted that in this simple model, any errors in the assumed mean crustal velocity model (in which the crust is 6 km thick with an apparent thickness of 2 s) would only manifest itself in an additive constant to the computed crustal thickness. Lateral changes in the abyssal velocity structure, however, may bias this simple model, and it is possible that a thickening of layer 2A would cause an overestimate of the crustal thickening due to midplate volcanism, for example. If changes in the original oceanic crustal thickness and structure are uncorrelated with the locations of seamounts, such errors may cause scatter but would not systematically bias the results. Most of the variation in apparent crustal thickness (Figure 4-5) is probably due to real crustal thickening associated with the seamounts. The main features of the seismic Moho observations are consistent with gravity observations and flexural models, as seen in Figure 4-6).

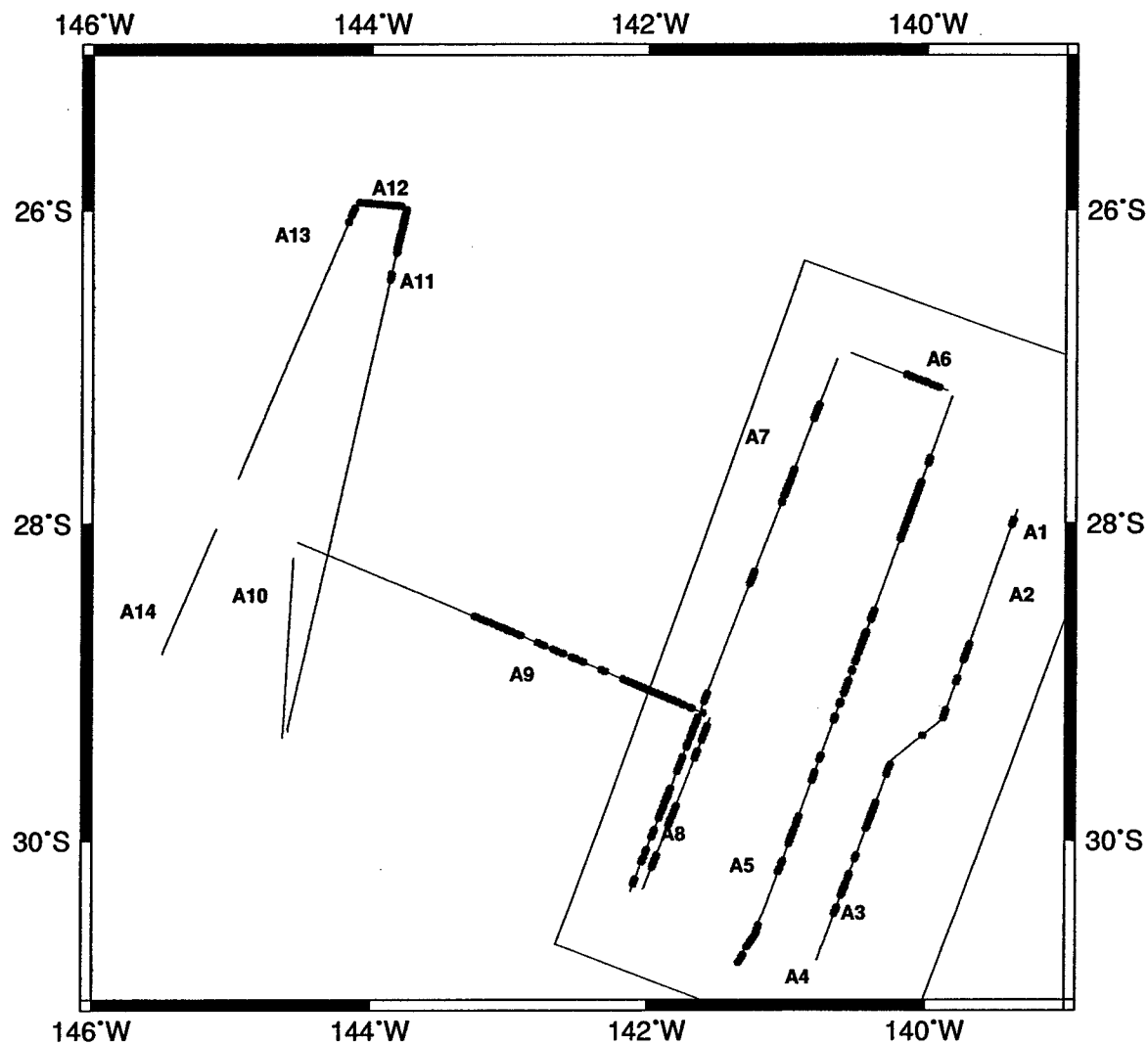


Figure 4-3: Multichannel seismic reflection lines acquired by EW9602, labeled A1-A14, and locations of digitized Moho picks (shown by grey circles). The subregion used for 2-D flexural modeling (shown in Figure 4-7) is outlined.

## 4.3 Analytical flexure modeling

### 4.3.1 Methods

In order to compare datasets directly and efficiently, rectangular grids were constructed of the Southern Austral region. The domain used was a 256 by 128 km grid in distance coordinates based on an oblique Mercator projection with an azimuth of 110°. Grid spacing was 2 km for calculation of potential fields and bathymetric

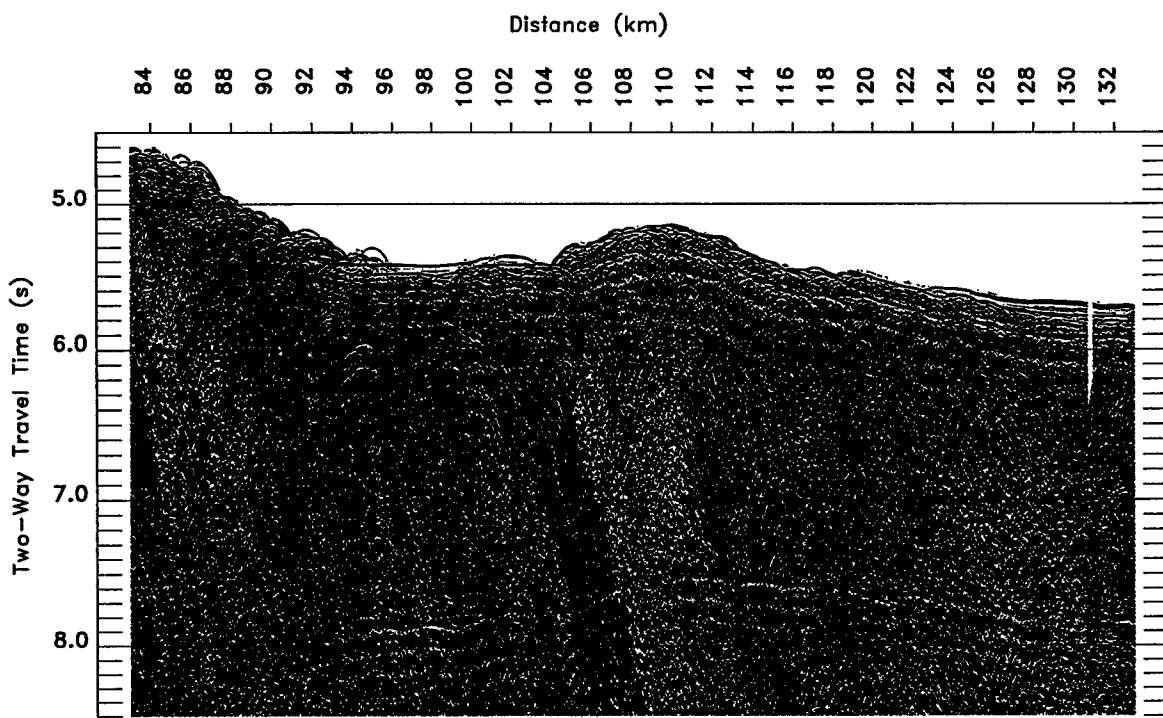


Figure 4-4: Seismic section from the north flank of the Ngatemato chain on line A5 illustrating the Moho reflection and the crustal thickening associated with the volcanics. The entire seismic line may be seen in Figure B-4 in Appendix B.

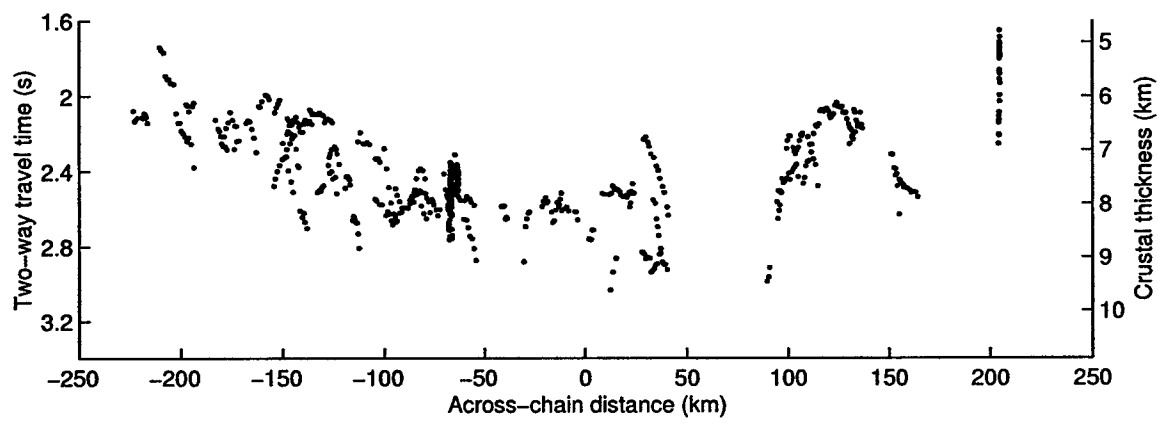


Figure 4-5: Apparent crustal thickness (left vertical axis) and computed crustal thickness (right vertical axis) for all Moho picks from lines A1-A9 projected into distance across the chain. The seismic data, Moho picks, and location and origin of each line are shown in Appendix B. Increasing apparent crustal thickness is down.

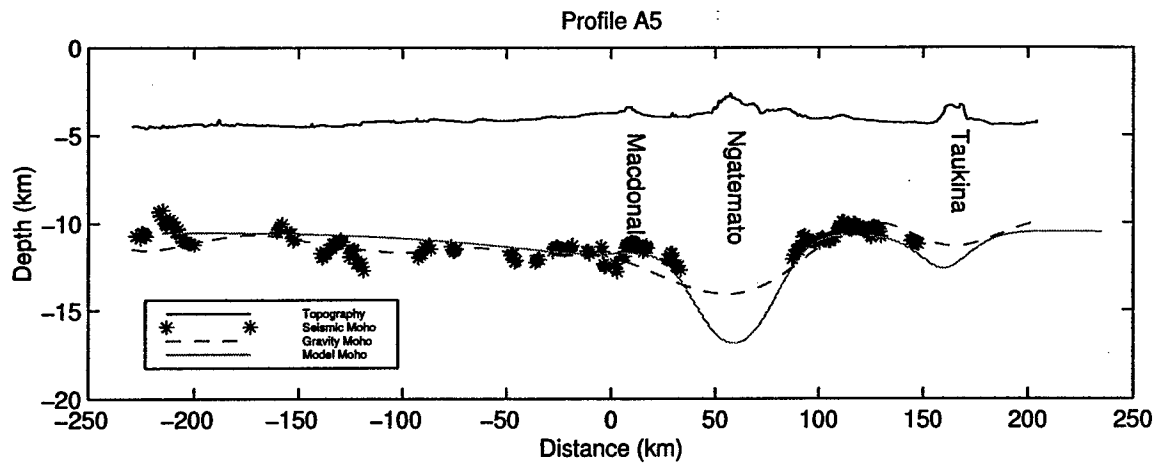


Figure 4-6: A profile of line A5 with three different geophysical estimates of crustal thickness. Top line shows Hydrosweep center beam bathymetry profile, stars indicate seismic Moho observations, dashed line is Bouguer gravity anomaly downward continued (in 3D) to a mean depth of 11 km below sea surface, and light grey line is a model Moho deflection for an analytical loading solution (see Section 4.3). Vertical axis is in kilometers below sea surface.

loading. The bathymetric grid was produced by median filtering of the gridded bathymetry from SO-47 and EW9602 multibeam data followed by regridding with splines under tension by the method of *Smith and Wessel* [1990]. Free air gravity data grids were constructed on the same scale from shipboard observations and the satellite gravity grid of *Sandwell and Smith* [1997]. The measurement error in the shipboard gravity data is probably less than 5 mGal [*Bell and Watts*, 1986]. Also, the seismic Moho observations described in Section 4.2.1 were median filtered to 2 km spacing to allow direct comparison with flexure calculations.

Analytical loading solutions to an elastic plate were used to predict the deflection due to idealized loads representing the volcanic loads in the region. The seamounts of the Taukina and Macdonald chain were represented by the sum of finite disks [*McNutt and Menard*, 1978], while the Ngatemato chain was approximated by a finite-width line load of constant height (see Appendix A). The parameters used for the size of the model loads are shown in Table 4.1. The Macdonald and Taukina seamounts were centered at the true locations of the seamounts, and the Ngatemato line was placed

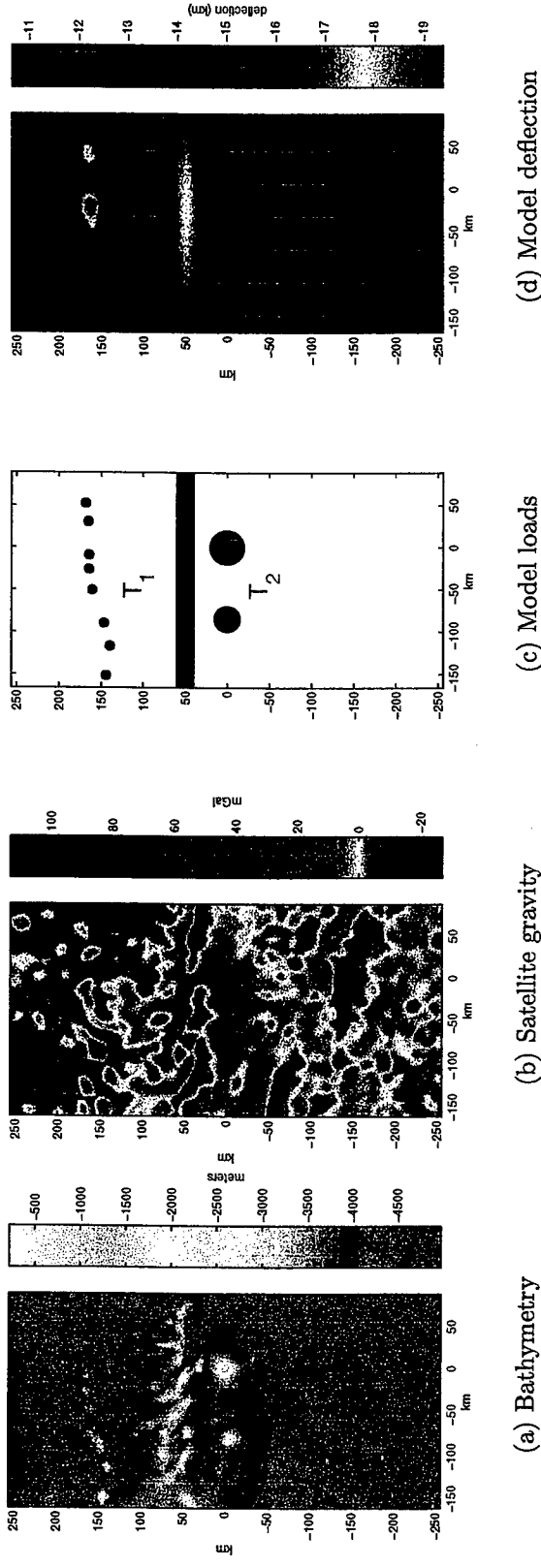


Figure 4-7: Gridded data for the model domain and model input and output, in oblique Mercator projection. (c) and (d) show the input and output of a particular realization of the analytical loading model described in the text. Taukina and Ngatemato volcanics, shown in blue as  $T_1$  in (c), load an elastic plate with  $T_e = 2$  km. Macdonald volcanics, shown in magenta, as  $T_2$  in (c), load a plate with  $T_e = 15$  km. The broad deflection seen in (d) due to the load on the thicker plate may be distinguished from the more local deflection of the Taukina and Ngatemato chains. Profile A5, shown in Figure 4-6, is oriented vertically near the center of this region.

50 km to the north of Macdonald, on an azimuth of  $110^\circ$  (parallel with the x-axis of the grid, shown in Figure 4-7).

Table 4.1: Approximated seamount dimensions used in analytical plate loading models

Seamount	Base width	Height
Macdonald	25 km	5000 m
Ra	20 km	4500 m
Taukina seamounts	10 km	600 m
Ngatemato line	20 km	1500 m

The domain used in the modeling is shown in Figure 4-7, with the output of one deflection calculation. The computed plate deflection was compared with the observed seismic Moho and minimized in a least squares sense with respect to two parameters, the effective elastic plate thicknesses of the plate loaded by the Taukina and Ngatemato volcanics ( $T_1$ ) and the Macdonald volcanics ( $T_2$ ). A model free air gravity was computed with a two interface model, one of the seawater-volcanic interface based on gridded topography and one of the crust-mantle interface based on modeled plate deflection. This is equivalent to comparing a computed Bouguer anomaly to the upward continued model Moho interface. RMS misfits with respect to  $T_1$  and  $T_2$  were computed separately for the shipboard and satellite gravity grids. Model parameters used are shown in Table 4.2. The infill density  $\rho_0$  was also varied, but model results were shown to be relatively insensitive to the value chosen.

Table 4.2: Values of constants used in flexural and gravity modeling

Young's Modulus	$E$	$1.0 \times 10^{11}$ Pa
Poisson's ratio	$\nu$	0.25
Load Density	$\rho_v$	$2800 \text{ kg m}^{-3}$
Water Density	$\rho_w$	$1000 \text{ kg m}^{-3}$
Mantle Density	$\rho_m$	$3300 \text{ kg m}^{-3}$
Infill Density	$\rho_0$	$2200\text{--}2800 \text{ kg m}^{-3}$

### 4.3.2 Modeling results

Comparing the 2-D modeling results to the independent datasets of gravity data and crustal thickness from seismic reflection data give very similar results, which are broadly consistent with the one-dimensional flexural modeling described in *McNutt et al.* [1997]. The RMS misfit of the seismic data (Figure 4-8) and the gravity data (Figure 4-9) indicate that both are best fit with a thin (1–2 km)  $T_1$  and a thicker ( $\sim$ 20 km)  $T_2$ . The misfit places strong bounds on  $T_1$ , but is less sensitive to  $T_2$ . The strongest statement one can make on the basis of the misfit plots with regard to  $T_2$  is that it is very likely to be greater than about 12 km, but the upper bound is less defined, with up to  $T_2 = 40$  km lying within 10% of the minimum misfit. There is a tradeoff between the value of  $T_1$  and the width of the idealized load assumed for the Ngatemato chain (see Appendix A).

Much of the misfit in the results presented is due to complications not included in the simple analytical loading model. The largest of these is likely to be the tectonic effects of the Adventure Trough (see Section 3.3), which traverses the southern part of the study area. The errors induced from this source are not likely to bias the elastic thickness calculations, but to increase the magnitude of the RMS misfit values. Another source of error is the distribution of the load itself, which is addressed by the topographic loading models that follow.

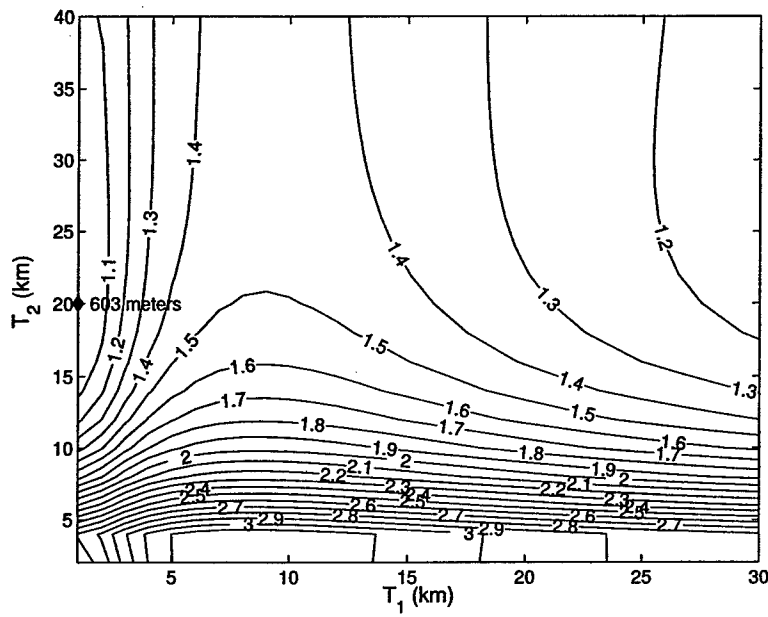


Figure 4-8: Contour plot of misfit between seismic Moho observations on lines A5 and A7 and Moho deflection in analytical loading model. Contours are normalized by the minimum RMS misfit of 603 m at  $T_1 = 1$  km,  $T_2 = 20$  km.

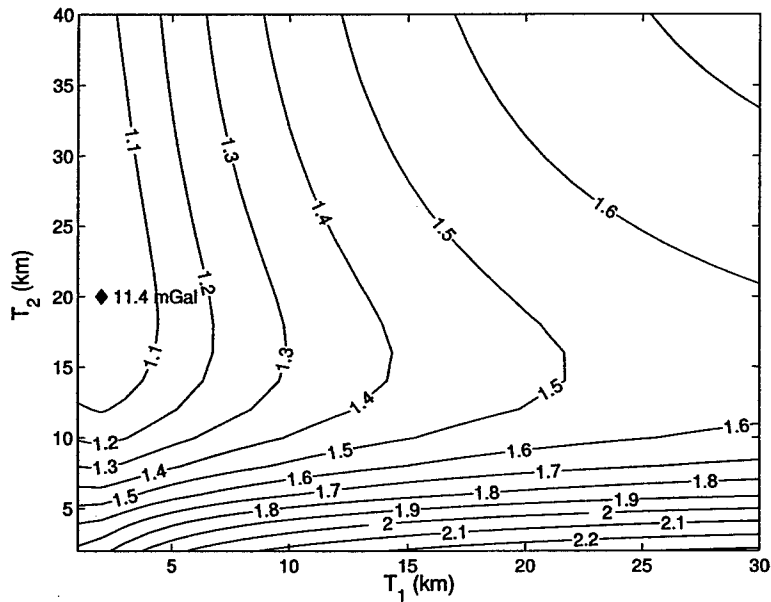


Figure 4-9: Contour plot of misfit between shipboard gravity data and gravity anomaly predicted by analytical loading model. Contours are normalized by the minimum RMS misfit of 11.4 mGal at  $T_1 = 2$  km,  $T_2 = 20$  km.

## 4.4 Flexural modeling with observed topography

### 4.4.1 Methods

Since the elastic plate loading problem is linear, the deflection found by the equation

$$D\nabla^4 w + \Delta\rho_1 gw = -\Delta\rho_2 gh \quad (4.1)$$

can be applied repeatedly and summed if the loading happened at discrete times with different thermal properties of the plate leading to different values of  $T_e$  (and thus  $D$ ). In the current problem, a load  $h_1$  loads a plate with elastic plate thickness  $T_1$  at time  $t_1$ , and at some later time  $t_2$  a volcanic load  $h_2$  loads the plate which now has elastic thickness  $T_2$ .

The difficulty lies in determining the separation of  $h_1$  and  $h_2$  from the observed topography, particularly if the volcanic loads of different ages are intermingled spatially. For the following trials, the topography was split into  $h_1$  and  $h_2$  along a line with orientation N110° E, which is horizontal in the projection used in Figure 4-7. A linear taper with width 12 km was applied between the north and south topography. Results were not sensitive to the nature and width of this taper. In addition, to account for the depression of the older topography ( $h_1$ ) by the younger load ( $h_2$ ), the deflection  $w_2$  was added to the observed topography to the northern side before computing  $w_1$ . The loads  $h_1$  and  $h_2$  are considered to be all the topography in excess of a reference level of 4600 m below sea level. A cross-section of the topography is shown in Figure 4-10. The two deflections  $w_1(x, y)$  and  $w_2(x, y)$  are solved for in the Fourier domain and summed. RMS fits to the seismic Moho and and gravity observations are computed similarly to Section 4.3.2.

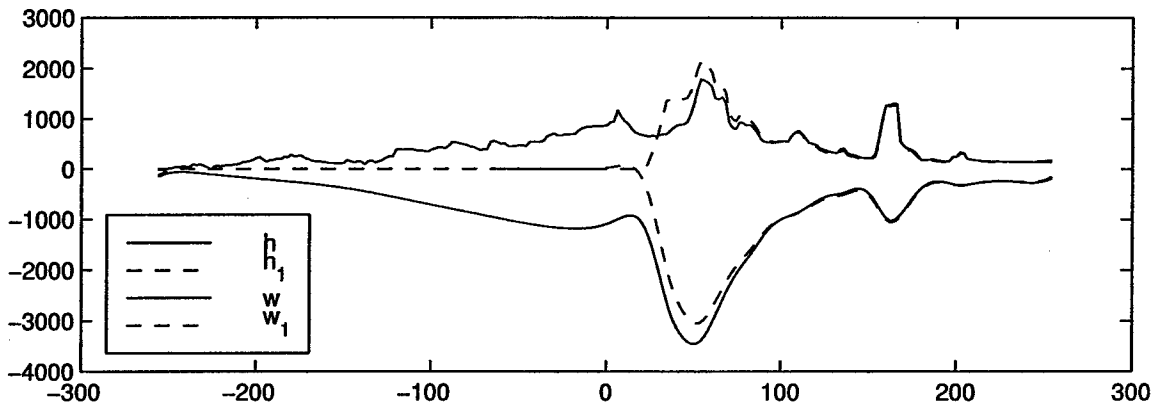


Figure 4-10: Topography and model Moho deflection on line A5 for northern and total load. The top solid line is the observed topography  $h$ . Shown by a dashed line is  $h_1$ , obtained from the observed topography plus the deflection  $w_2$  to restore it to the height before the younger volcanism, and tapered from 0 for  $y < 22$  km to full height for  $y > 34$  km. The total deflection  $-w$  (lower solid line) and the northern component of the deflection  $-w_1$  (lower dashed line) are also shown, for a best fitting model with  $T_1 = 1$  km,  $T_2 = 10$  km,  $\rho_0 = 2600$  kg/m<sup>3</sup>.

#### 4.4.2 Results

Model results for the loading with observed topography prove more sensitive to the value of  $\rho_0$  than did the analytical models of Section 4.3 (see Figure 4-11). The best fit of the shipboard gravity data is at  $\rho_0 = 2200$  kg/m<sup>3</sup> and of the seismic data is at  $\rho_0 = 2000$  kg/m<sup>3</sup>. As  $\rho_0$  is increased in the model runs, not only does the misfit increase to both the gravity and seismic fits, but the solutions for the gravity and seismic fits diverge from each other. With higher infill density, the location of the minimum misfit in  $T_1, T_2$  space is little changed, but in the seismic fits the optimum value of  $T_2$  is driven to lower values (and in fact to zero for  $\rho_0 \geq 2600$  kg/m<sup>3</sup>). The favoring of lower infill density may be due to the truncation of the  $h_2$  load by the  $h_1$  load to the north, and the downward deflection of the northern topography which has effectively  $\rho_0 = 1000$  kg/m<sup>3</sup>. The infill is constrained to be asymmetric in this way, which is not fully accounted for in the model. The presence of a bathymetric swell may account for some misfit as well (see Section 4.4.3).

Misfit plots for the observed topography loading models are shown in Figures 4-12,

4-13 and 4-14. Results are similar to the analytical loading model in that (especially for the gravity fits) the value of  $T_1$  is well constrained to low values, while the value of  $T_2$  is less well defined. The values for  $T_2$  are considerably lower (8–10 km) than the values obtained for the analytical models (15–20 km), although the 10% misfit regions overlap between the different models. Clearly the lower values for the solutions using actual topography are the result of the long wavelength topography included in  $w_2$ , which can fit long wavelengths in the observational fields. The only way to do so within the analytical loading model, which contains only more discrete loads, is with a higher flexural rigidity.

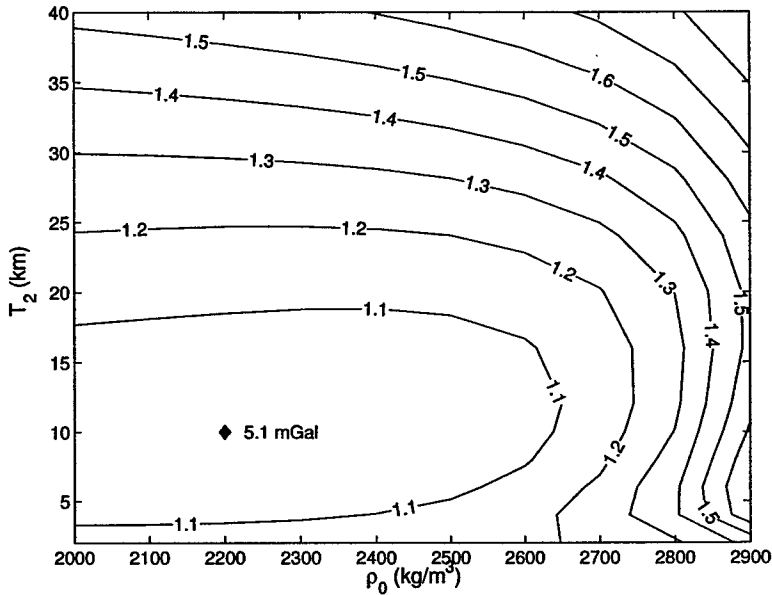


Figure 4-11: Contour plot of misfit between shipboard gravity observations and free air gravity anomaly predicted by the dual loading topography model. Axes are  $T_2$  and  $\rho_0$ , computed with  $T_1$  fixed at 1 km. Contours are normalized by the minimum RMS misfit of 5.1 mGal at  $\rho_0 = 2200 \text{ kg/m}^3$ ,  $T_2 = 10 \text{ km}$ .

#### 4.4.3 Reduced topography models

The presence of a broad swell would adversely affect the preceding models, since long wavelength topography which is thermally supported would be erroneously used as

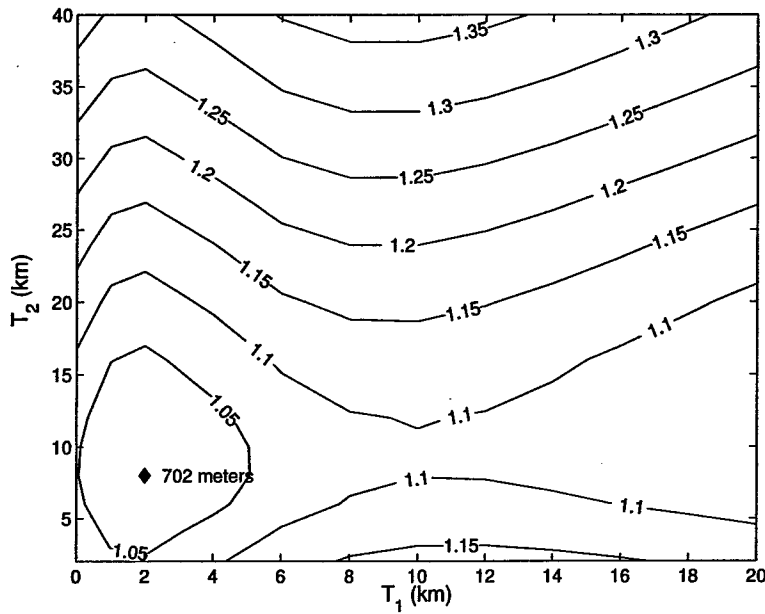


Figure 4-12: Contour plot of misfit between all seismic Moho observations in the region and Moho deflection in dual loading topography model. Contours are normalized by the local minimum RMS misfit of 702 m at  $T_1 = 2$  km,  $T_2 = 8$  km.

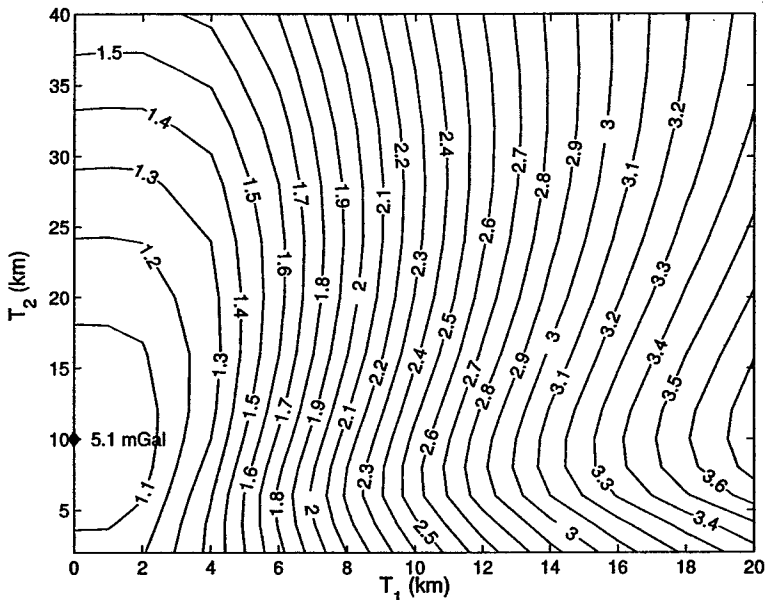


Figure 4-13: Contour plot of misfit between shipboard gravity observations and free air gravity anomaly predicted by the dual loading topography model. Contours are normalized by the minimum RMS misfit of 5.1 mGal at  $T_1 = 0$  km,  $T_2 = 10$  km.

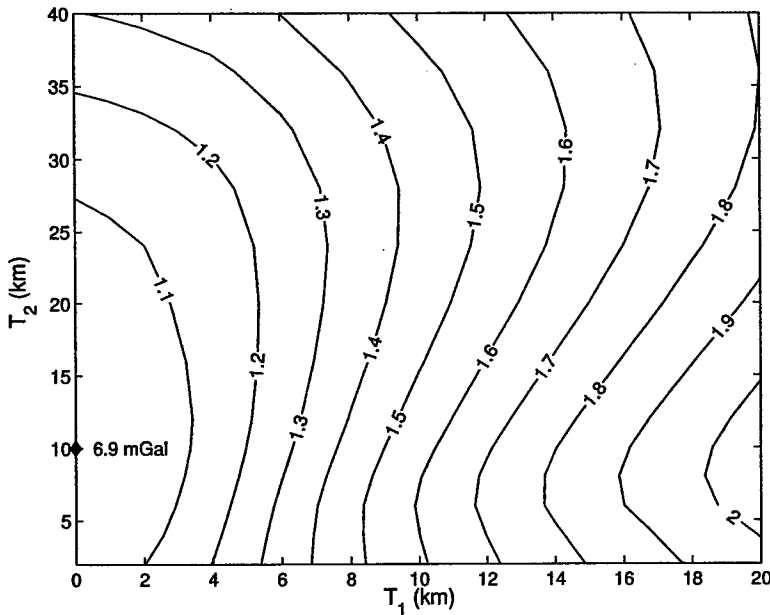


Figure 4-14: Contour plot of misfit between satellite gravity observations and free air gravity anomaly predicted by the dual loading topography model. Contours are normalized by the minimum RMS misfit of 6.9 mGal at  $T_1 = 0$  km,  $T_2 = 10$  km.

a load to predict flexural topography. The swell at the Australs is relatively small [Sichoix *et al.*, 1998], but it does systematically bias the flexural results. I removed a 300 m gaussian swell with a half width of 200 km, obtained by manually fitting bathymetric profiles, from the topography and computed flexural loading models as in the previous section. Results are shown in Figures 4-15, 4-16, and 4-17. As expected, the best fitting values for  $T_2$  are increased, since much of the long wavelength component of the load has been removed, and a higher flexural rigidity is necessary to fit the data. The misfit values are also slightly decreased, though the bounds on the solution are still broad.

#### 4.4.4 Model results summary

A summary of the modeling results presented in the preceding sections is shown in Table 4.3. I have followed the method of Kruse *et al.* [1997] and used the level of RMS misfit 5% higher than the minimum as an error estimate. This corresponds to

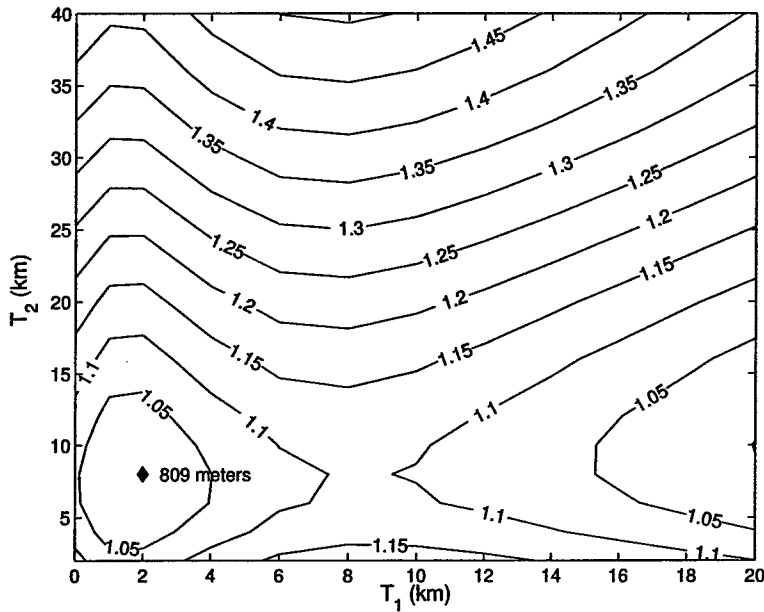


Figure 4-15: Contour plot of misfit between all seismic Moho observations in the region and Moho deflection in dual loading reduced topography model for  $\rho_0 = 2600 \text{ kg/m}^3$ . Contours are normalized by the local minimum RMS misfit of 809 m at  $T_1 = 2 \text{ km}$ ,  $T_2 = 8 \text{ km}$ .

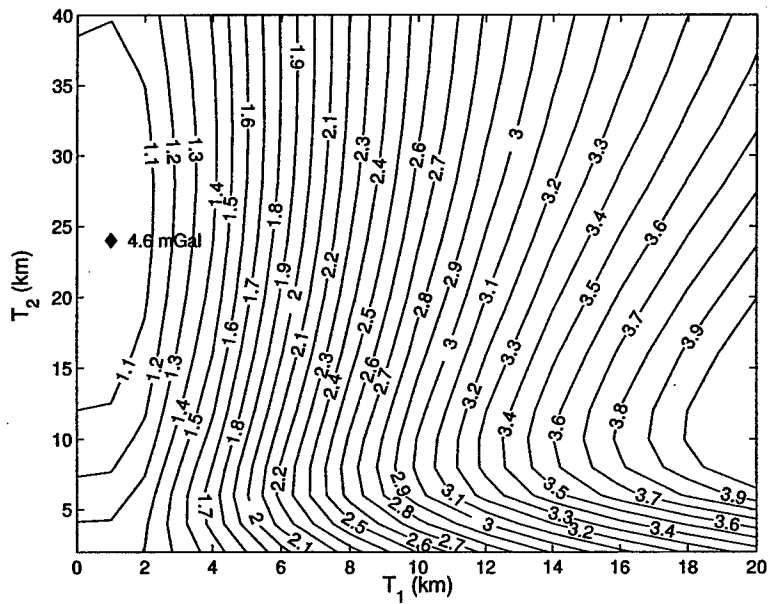


Figure 4-16: Contour plot of misfit between shipboard gravity observations and free air gravity anomaly predicted by the dual loading reduced topography model for  $\rho_0 = 2600 \text{ kg/m}^3$ . Contours are normalized by the minimum RMS misfit of 4.6 mGal at  $T_1 = 1 \text{ km}$ ,  $T_2 = 24 \text{ km}$ .

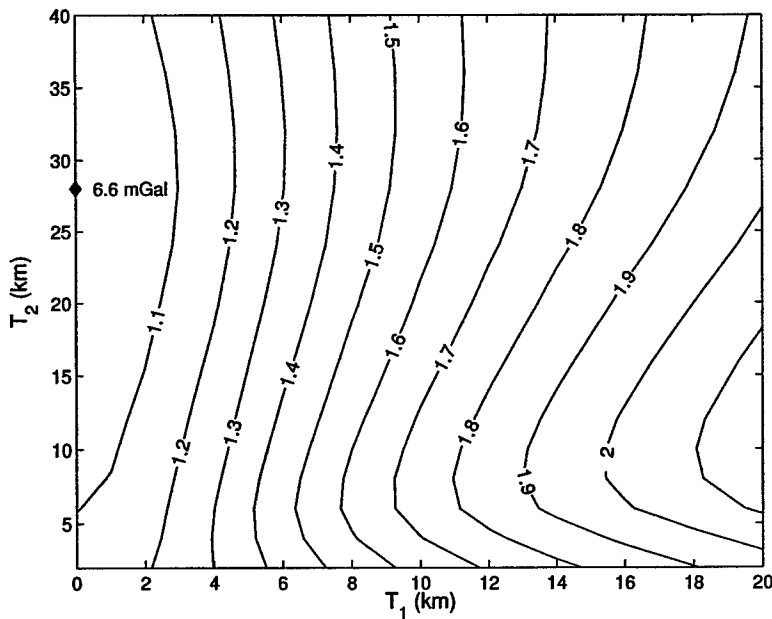


Figure 4-17: Contour plot of misfit between satellite gravity observations and free air gravity anomaly predicted by the dual loading reduced topography model for  $\rho_0 = 2600 \text{ kg/m}^3$ . Contours are normalized by the minimum RMS misfit of 6.6 mGal at  $T_1 = 0 \text{ km}$ ,  $T_2 = 28 \text{ km}$ .

the 1.05 contour in the misfit figures in this chapter.

The values for  $T_1$  are consistently low, regardless of the modeling method or parameters used. The values for  $T_2$  are much more varied, with large error bars.

## 4.5 Discussion

### 4.5.1 Elastic thickness

Although the best fitting models presented in this chapter generally are found with values of  $T_1$  of 1–2 km, the uncertainties are such that values of 5 km or more cannot be ruled out. Further, all of the models assume a continuous elastic plate, and if the plate is broken or weakened beneath the load (and the morphology suggests it may be), then the values obtained by these will underpredict the rigidity of the plate.

Model estimates of the elastic thickness ( $T_2$ ) of the plate loaded by the Macdonald

Table 4.3: Summary of flexure modeling results

$\rho_0$ (kg/m <sup>3</sup> )	$T_1$ (km)	$T_2$ (km)	method
analytical model			
2800	$1 \pm 0.7$	$20 \pm 8.1$	seismic
2800	$2 \pm 1.2$	$20 \pm 9.9$	gravity
dual topography loading model			
2200	$2 \pm 2.5$	$8 \pm 7.3$	seismic
2200	$0 \pm 2.0$	$10 \pm 4.7$	gravity
2600	$1 \pm 1.5$	$2 \pm 6.6$	seismic
2600	$0 \pm 1.0$	$12 \pm 5.2$	gravity
2800	$1 \pm 1.4$	$2 \pm 13.5$	seismic
2800	$2 \pm 2.3$	$2 \pm 4.8$	gravity
reduced topography model			
2200	$2 \pm 3.2$	$8 \pm 8.6$	seismic
2200	$2 \pm 1.4$	$28 \pm 10.6$	gravity
2600	$2 \pm 2.0$	$8 \pm 5.4$	seismic
2600	$1 \pm 0.9$	$24 \pm 9.0$	gravity
2800	$1 \pm 1.4$	$2 \pm 7.2$	seismic
2800	$0 \pm 1.1$	$24 \pm 7.9$	gravity

seamounts range from 8–24 km. Clearly the method does not have great sensitivity to  $T_2$ . The difficulty in obtaining a more precise value for  $T_2$  is due to the tradeoff between the nearby older volcanic edifices. However, it seems that the lowest estimates are biased by the swell, and possibly with apron sediments which would also be correlated with the load. A value of  $T_2$  around 15–20 km seems to be the best estimate, but the uncertainties are large and difficult to calculate. These plate thicknesses are about what one would expect for the depth to the 450°C–600°C isotherms [Watts *et al.*, 1980a]. Although low values such as those obtained by Calmant and Cazenave [1987] cannot be ruled out, the results in this chapter are generally more consistent with those of Filmer *et al.* [1993] finding normal elastic plate thicknesses in the Marquesas Islands.

#### 4.5.2 Volcanic volumes and rates

The results of the flexural modeling may be used to calculate the volume of each volcano or chain, including the compensated root and filled part of the moat. Estimates of the total volume of material added to the oceanic crust by midplate volcanic processes in the Southern Austral region indicate that the smaller, lower old seamounts have actually contributed more material than the younger, larger ones. Model results suggest that 1.2–1.6 times as much material was produced by the Ngatemato and Taukina chains together as by the Macdonald chain, within the study area shown in Figure 4-7.

The cross-sectional area of the Ngatemato and Taukina chains together is about 350–400 km<sup>2</sup>, while the Macdonald chain is about 250–300 km<sup>2</sup>, across strike. If this volume was produced at the rate of absolute plate motion, that corresponds to about 0.04 km<sup>3</sup>/y and 0.03 km<sup>3</sup>/y, respectively, considerably less than the rate of volcanic production at Hawaii or the Marquesas [Filmer *et al.*, 1994].

#### 4.5.3 Causes for Austral volcanism

The three chains of seamounts observed in the study area seem to defy explanation by any common cause. The morphology and timing of the volcanism suggests several mechanisms are at work. The en echelon nature of the Ngatemato volcanoes, their occurrence on relatively young (10–15 Ma) lithosphere, and their lack of a linear age progression are reminiscent of the Puka Puka ridges, thought to be the result of local magmatic upwelling due to lithospheric extension and fracture [Sandwell *et al.*, 1995]. A south facing scarp with the trend of the Ngatemato volcanic chain, but oblique to all preexisting tectonic features, is apparently a normal fault associated with this extension. The Taukina chain is similar in size and morphology to near-ridge seamount chains [e.g., Scheirer *et al.*, 1996], and are likely a product of excess melt production off-axis. Geochemically, the two chains are quite similar [Reynolds *et al.*, 1997], and they formed roughly contemporaneously. It seems likely that the

extension and faulting of the young oceanic lithosphere was able to tap excess melt already present in the aesthenosphere. The upwelling and melting would be expected to be enhanced by thinned lithosphere, and so it is not surprising that the volume of the Ngatemato volcanics is larger. The separation of the two chains, about 100 km, is likely related to the horizontal scale over which aesthenospheric melts may be tapped.

The Macdonald volcanic chain is quite different in morphology from the Taukina and Ngatemato chains. Also, samples from the summits of the Macdonald volcanoes have yielded young radiometric dates [*Turner and Jarrard, 1982; Stoffers et al., 1989*]. However, dredge samples from the flanks of two of these volcanoes, Marotiri and Ra, have yielded much older dates [*McNutt et al., 1997*]. Clearly, young volcanoes are overprinting older edifices. A question remains as to whether the old edifices become pathways for renewed volcanic activity or they have merely been buried in the flanks of a nearby recent volcano.

## 4.6 Conclusion

Gravity and seismic data in conjunction with flexural modeling shows that the older, lower Ngatemato seamounts have added more material to the oceanic crust than the younger, higher islands and seamounts of the Austral chain. In addition, at least some of the edifices associated with young volcanism have formed on a base of a much older volcano. The distribution of volcanism is also affected by tectonic features in the region, especially the Adventure Trough. Thus, it is likely that not only are the oldest, lower (but more voluminous) volcanoes in the region not produced by hotspot processes, but that non-hotspot processes such as lithospheric cracking play an important role in the distribution and formation of the younger, larger seamounts and islands of the Macdonald chain as well.



# Chapter 5

## Archipelagic Aprons: The Role of Mass Wasting and Volcanism

“Well, Sergeant, specifically of course we can know nothing—unqualified—but like the rest of us, I’ve fenced my life with a scaffolding of more or less speculative hypotheses.”

T. E. Lawrence, *The Mint*

### 5.1 Introduction

This chapter discusses the morphology and possible origin of some features in the southern Austral study area. Section 5.2 presents clear evidence for mass wasting processes at work in the submarine flanks of the Southern Austral Islands, while Section 5.3 presents data that argue for volcanic emplacement on the outer flanks of the main edifices, in the archipelagic apron. Finally, Section 5.4 compares and contrasts some of the features of other island chains with observations in the Australs. A reference map for the figures in this chapter is shown in Figure 5-1.

### 5.2 Evidence for mass wasting

Mass wasting is a major factor in the evolution of the islands and seamounts of the region. At some island chains (e.g., the Marquesas [*Wolfe et al., 1994*]), more than

half of the volcanic material which forms the edifices is eroded into the moat. The Australs are generally smaller edifices, and the submarine features in much of the survey area have never been emergent islands. How much material is removed from a volcanic edifice by entirely submarine erosion? How much does the rate of erosion increase after a seamount grows to become an island? First we must determine which features in the Australs are erosional at all.

Mass wasting in the Southern Austral Islands is evident in many places. On the western flank of Macdonald Seamount and to the north and south of Rapa there is evidence for deposits hundreds of meters thick, presumably derived from the large volcanoes nearby. The layering observed indicates that the sediments were laid down in a relatively smooth fashion, perhaps by turbidity flows. A seismic reflection image of the volcaniclastic pile near Macdonald Seamount is shown in Figure 5-2.

More dramatically, a large erosional feature is observed on the south flank of Rapa in Hydrosweep bathymetry data (see Figures 5-3 and 5-4). A smoothly sloping “chute” about the same width as the island itself is surrounded on either side by rougher topography. The chute appears lineated downslope in a map of Hydrosweep amplitudes (Figure 5-4). This feature may be the headwall of a landslide, or it may be the result of erosion by turbidity currents. Unfortunately, the resolution of the Hydrosweep data is fairly low for investigating this structure in detail, and in any case the coverage of this area by EW9602 data is poor. The area immediately downslope from the chute—where a landslide deposit would be found if the feature is a headwall—is not mapped.

### 5.3 Evidence for apron volcanism

Some of the most intriguing and ambiguous observations from EW9602 data are from seismic line A9, a 300 km long survey line oriented parallel to the trend of the volcanic chains, 50 km south of the Macdonald chain (see Figure 4-2). The eastern part of the

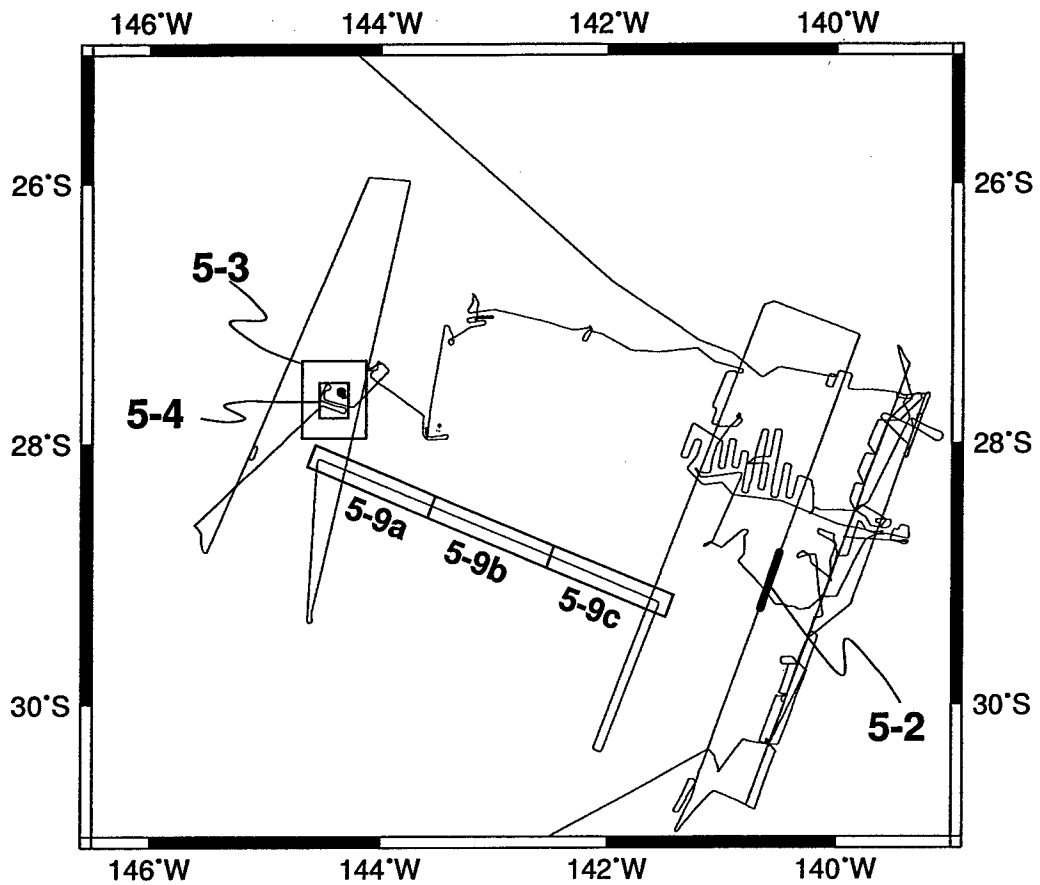


Figure 5-1: Map of the southern Austral region, indicating locations of Figures 5-2, 5-3, 5-4 and 5-9 (which is coincident with 5-10), as well as the ship track for EW9602. Map limits are the same as in Figures 4-2 and B-1.

line is characterized by flat seafloor, interrupted by a tectonic scarp associated with the Adventure Trough. On the easternmost 25 km of the line, near the intersection with line A7, abyssal hill fabric is present, but from there to a point south of Marotiri (from 130 to 275 km in Figure 5-8) the seafloor is flat (with the exception of the aforementioned scarp), characterized by slopes of less than 1°, dipping slightly to the south.

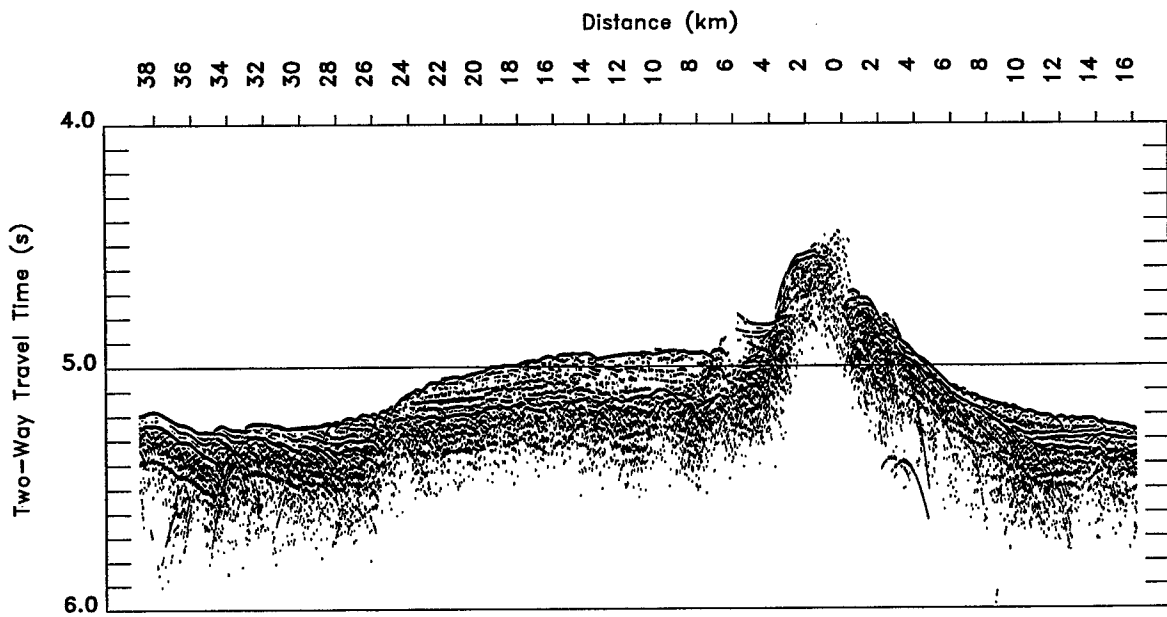


Figure 5-2: Volcaniclastic sediments derived from Macdonald Seamount, observed on line A5. Multichannel seismic data stacked at 12.5 m CDP spacing. The entire seismic line is shown at a smaller scale in Figure B-4.

The western half of the moat profile, however, is quite different. It shows a rough, hummocky terrain that stands up to 800 m higher than the flat-lying basement to the east and west. This terrain, especially to the west, appears to be made up of many overlapping edifices which are nearly circular in plan view. Each of these terrains is discussed in the next two sections.

### 5.3.1 The “moat”

Three explanations seem possible for the flat-lying “moat” terrain: that it is the top surface of sediments derived from the volcanic chain, that it is unusually smooth abyssal seafloor, or that it has been paved over by lava flows.

The hypothesis that the flat lying region is due to sedimentation deposited in the moat seems the most obvious solution. However, it can be most strongly rejected. This section of the moat is not near any islands (or any features that are likely to once have been islands), so all the sediment would have to have been derived

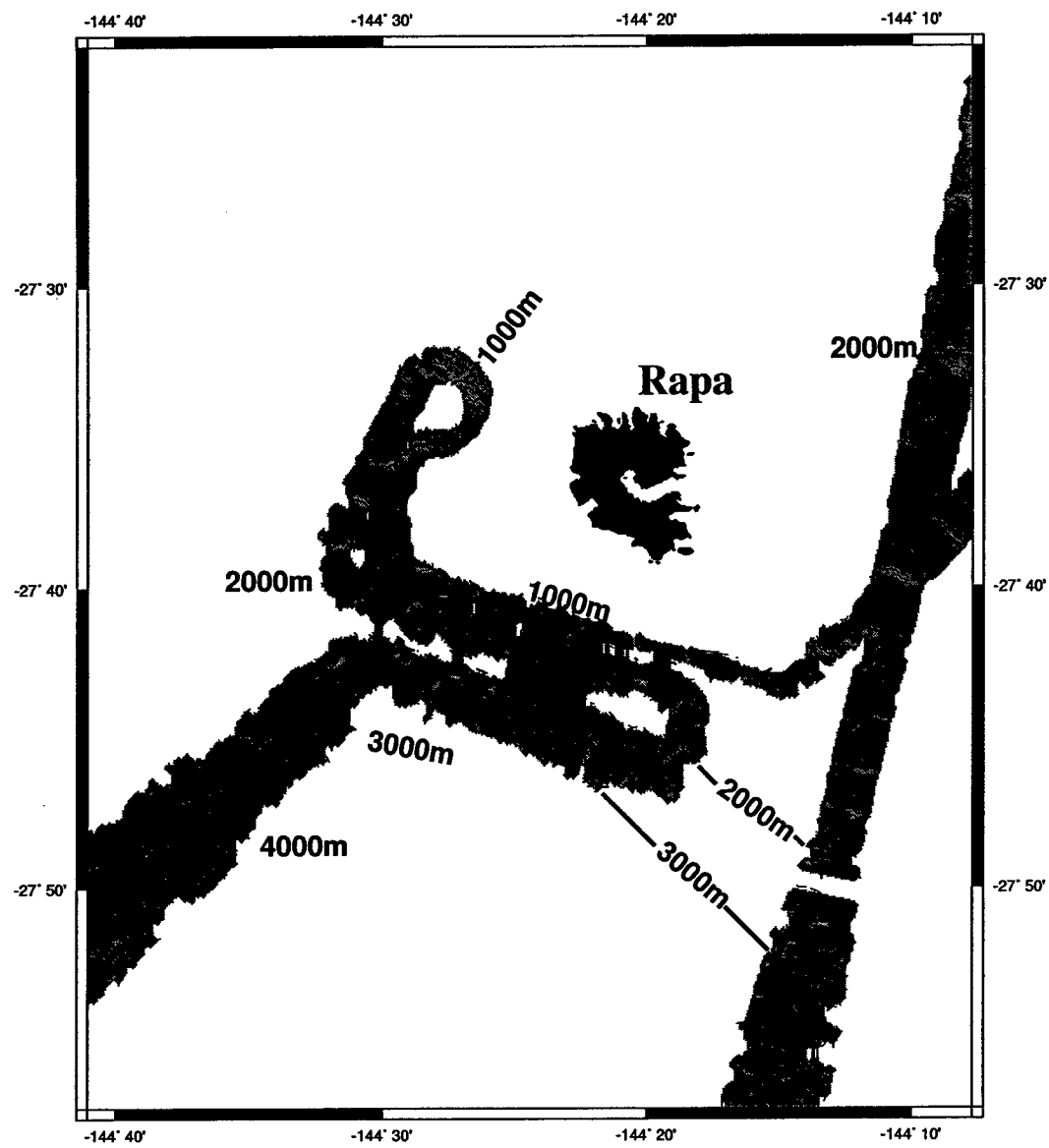


Figure 5-3: Shaded relief contour map of gridded hydrosweep bathymetry on the flanks of Rapa. Heavy contours are at 1000 m intervals, light contours are 250 m intervals.

from seamounts. Unfortunately, the seamounts immediately adjacent to this terrain have not been mapped by multibeam bathymetry, so their morphology is unknown. Satellite altimetry (which proved to be reliable for the identification and location of seamounts in the EW9602 survey) indicated the presence of a topographic ridge 50 km north of the line A9.

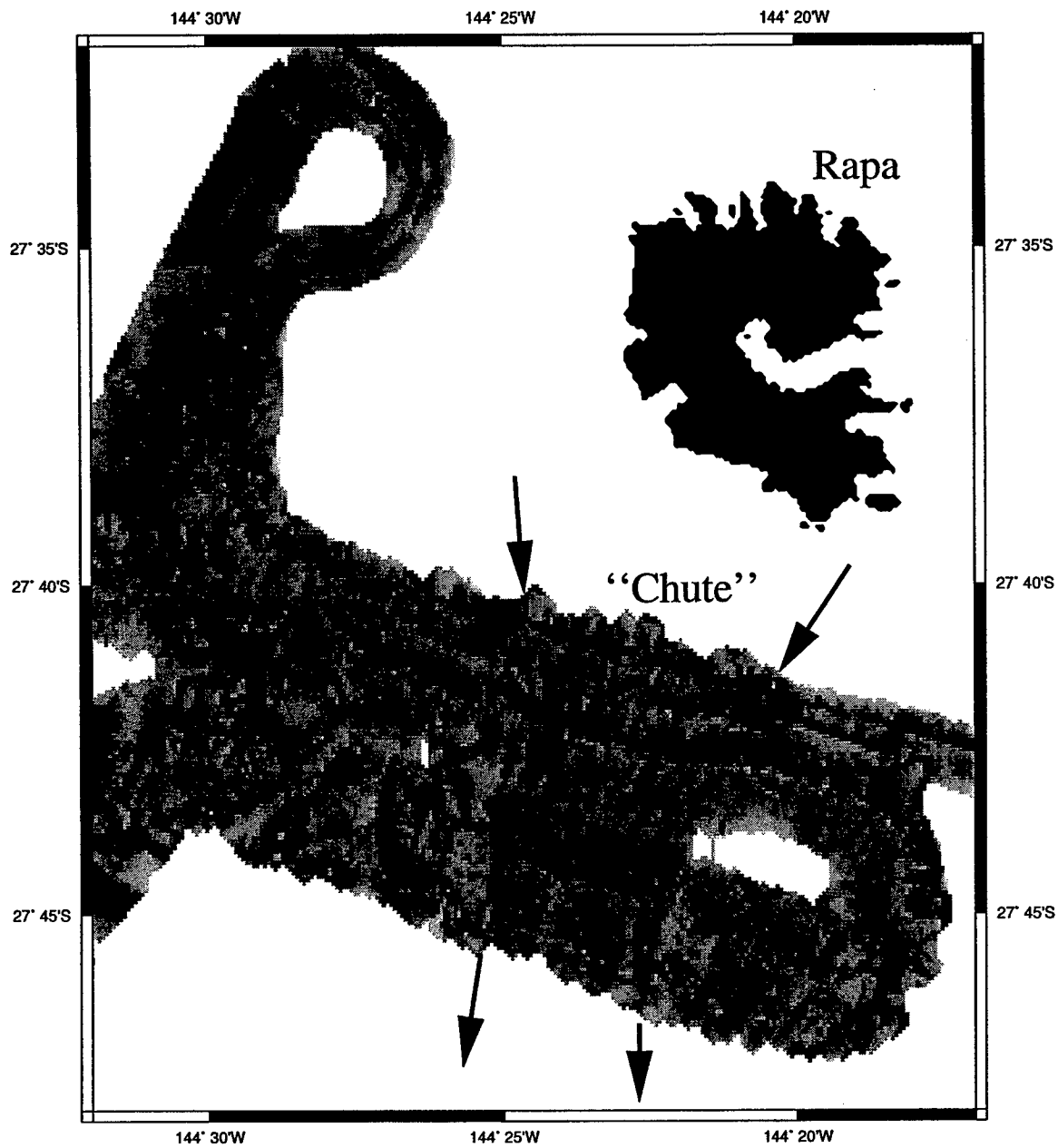


Figure 5-4: Enlarged view of gridded Hydrosweep amplitudes on the south flank of Rapa. High amplitudes are dark. Note the “chute” downslope from the island.

To have so completely filled the moat and buried the abyssal hills, there must be at least several hundred meters of sediment, but MCS data images only a thin (~ 0.1 s TWTT) pelagic layer of sediments on the eastern part of line A9 (see Figure 5-5). Even if there is a thick seismically opaque layer of volcaniclastic sediments

beneath this which we have not imaged, the basement interface should be visible in the sonobuoy data, but it is not (Figure 5-7). Nowhere else in the Southern Australs is such a flat region observed. Thicker units of sediments are imaged in some locations in the region, but much nearer to islands or seamounts, and only about 500 m in thickness at most (see Figure 5-2).

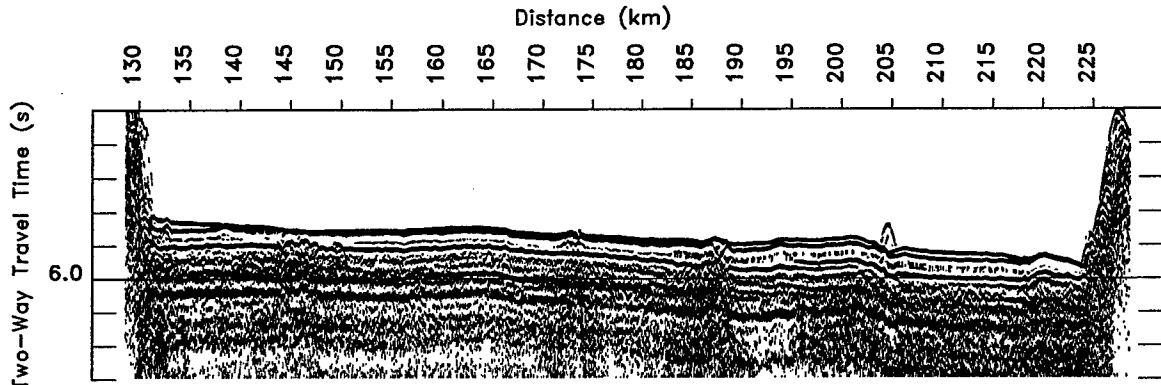


Figure 5-5: MCS image from line A9, in the “moat.” The full seismic line may be seen in Figure B-8.

The seismic data and the lack of a sedimented moat elsewhere in the region suggest that the flat terrain is due to the smooth basement. If the flat seafloor is due to flat volcanic basement, the question becomes whether this was formed at the ridge or whether more recent lava flows have covered the original abyssal fabric. Similar flat basement, imaged seismically beneath a thick sediment sequence, is observed by *Abrams et al. [1993]* in the Western Pacific. It is unlikely to be coincidental that the flat basement occurs so near the Austral Islands, so it is reasonable to assume that it is the result of lava flows which are related to the pervasive volcanism in the region rather than an original seafloor feature.

### Sonobuoy refraction data

During the multichannel seismic reflection survey by EW9602, 45 sonobuoys were deployed, of which 39 returned data. Data from Sonobuoy 22, on seismic line A9 (see Figure B-6) is shown in Figure 5-6. For each sonobuoy, an average shot spacing and

range were computed by fitting the direct water wave arrival and the seafloor reflection hyperbola where possible. One-dimensional velocity models were constructed by manually fitting travel time curves obtained from 1-D ray tracing. A number of the sonobuoys were difficult or impossible to model due to topographic effects and poor signal/noise, but useful refracted arrivals were present in 27 of the sonobuoy profiles, several of which include PmP and/or Pn arrivals. Sonobuoy velocity models for line A9 are shown in Figure 5-7, the locations of each of which are shown on Figure 5-9. Although Sonobuoys 20–22 are all on the flat moat terrain, only Sonobuoy 22 is completely free of topographic effects (20 and 21 contain sideswipes from the Adventure Trough-related scarp) and has good signal/noise for observing refracted events.

The refracted phase labeled  $R_1$  in Figure 5-6 is most relevant to the determination of the seismic velocity of the basement here. The slope and travel time of the  $R_1$  event require both a very thin sediment layer above it (about 0.1 s two-way travel time, or 125 m assuming 2.5 km/s) and high velocities (at least about 4.5 km/s) near the top of the basement. The other two events labeled in Figure 5-6,  $R_2$  and  $R_3$ , correspond to a layer 2B refracted phase and the Moho subcritical reflection [Ewing and Houtz, 1969], respectively.

### 5.3.2 Hummocky terrain

Swath views of the Hydrosweep data are shown in Figures 5-9 and 5-10. The blocky terrain is as much as 1000 m above the flat moat sediments to the east, including individual blocks as large as 3 km. In this section, I consider two possible origins of this terrain: that it is a large landslide deposit or that it is a constructional volcanic feature.

The cross-sectional area of the topography is  $50 \text{ km}^2$ , assuming a base level of 4400 m. If this material is the result of a landslide originating at Marotiri, 60 km to the north, a minimum estimate on the total volume of the deposit is about  $3000 \text{ km}^3$ , comparable to the large landslides observed in the Hawaiian Islands [Moore *et al.*,

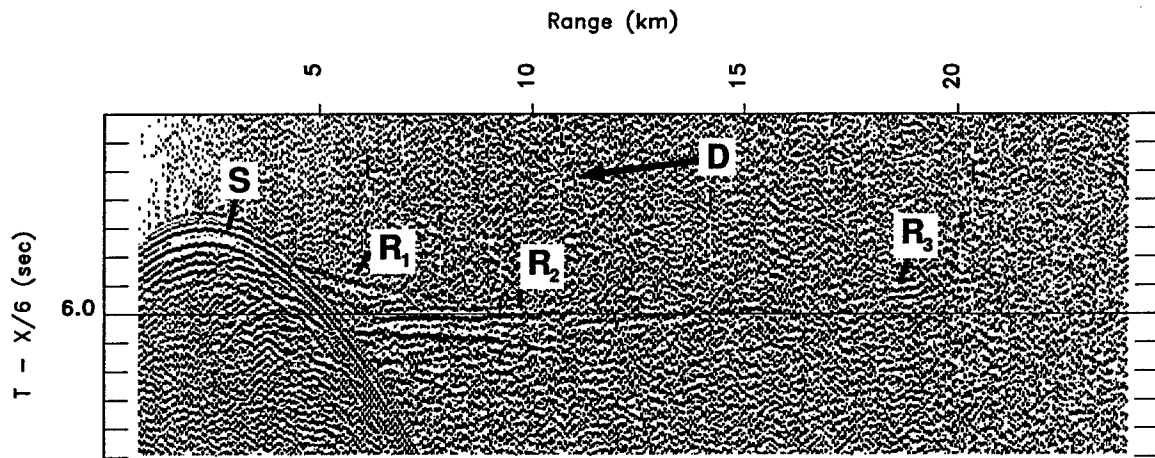


Figure 5-6: Sonobuoy 22 data, from the flat terrain on line A9 (see Figure 5-9 for location). Velocity reduced to 6 km/s. The seafloor reflection is labeled S, the direct water wave as D, and crust and mantle phases as R<sub>1</sub>, R<sub>2</sub>, and R<sub>3</sub> (see text for discussion).

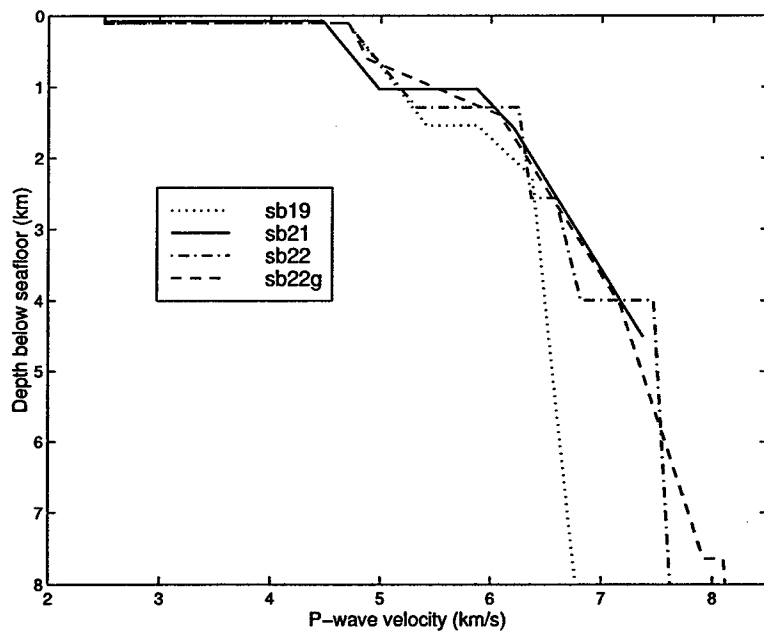


Figure 5-7: Velocity profiles from 1-D forward models of arrivals from three sonobuoys on the moat line (A9). Two different velocity models are shown for Sonobuoy 22 (data shown in Figure 5-6), one with velocity discontinuities within the crust (sb22) and one without (sb22g). Velocity models sb19 and sb21 both allow discontinuous velocity profiles. Travel time modeling was done with JDSeis.

1989]. If this feature is a landslide deposit, it is remarkable that the Austral Islands, much smaller than the Hawaiian Islands, can produce such prodigious mass wasting features.

Although the lobate nature of the flows and chaotic nature of the feature suggest that it may be depositional, the circularity of these edifices argues very strongly that they are constructional volcanic features. The simplest hypothesis is that all of the hummocky terrain is volcanic as well. It is a curious deposit, perhaps built up from lava flows which erupted on the distal south flank of Marotiri.

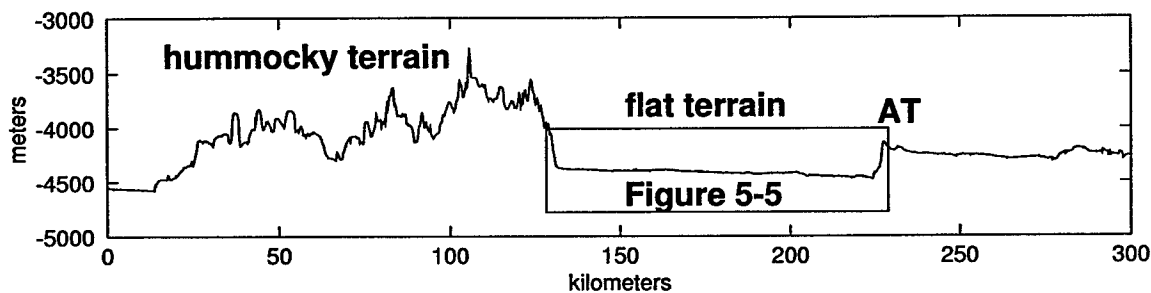


Figure 5-8: Bathymetry of line A9, along the moat south of Rapa and Marotiri. Hydrosweep center beam is plotted. Horizontal axis is in distance along track, with northwest to the left. From 15–130 km is the blocky terrain interpreted as a constructional volcanic feature. A scarp associated with the Adventure Trough (labeled "AT") is at about 225 km. The flat terrain and the location of the MCS data shown in Figure 5-5 are also shown.

It is difficult to determine whether the feature is the product of a single event or multiple episodes. The more rounded character of the deposit in the western part of the feature suggests that it may be an older, with edges rounded by pelagic sedimentation and perhaps by collapse or erosion. In contrast, the eastern deposit displays a more angular, chaotic texture to the blocks. Higher resolution sidescan sonar data would be the ideal tool to map the extent and character of the feature, but is unlikely to be available soon.

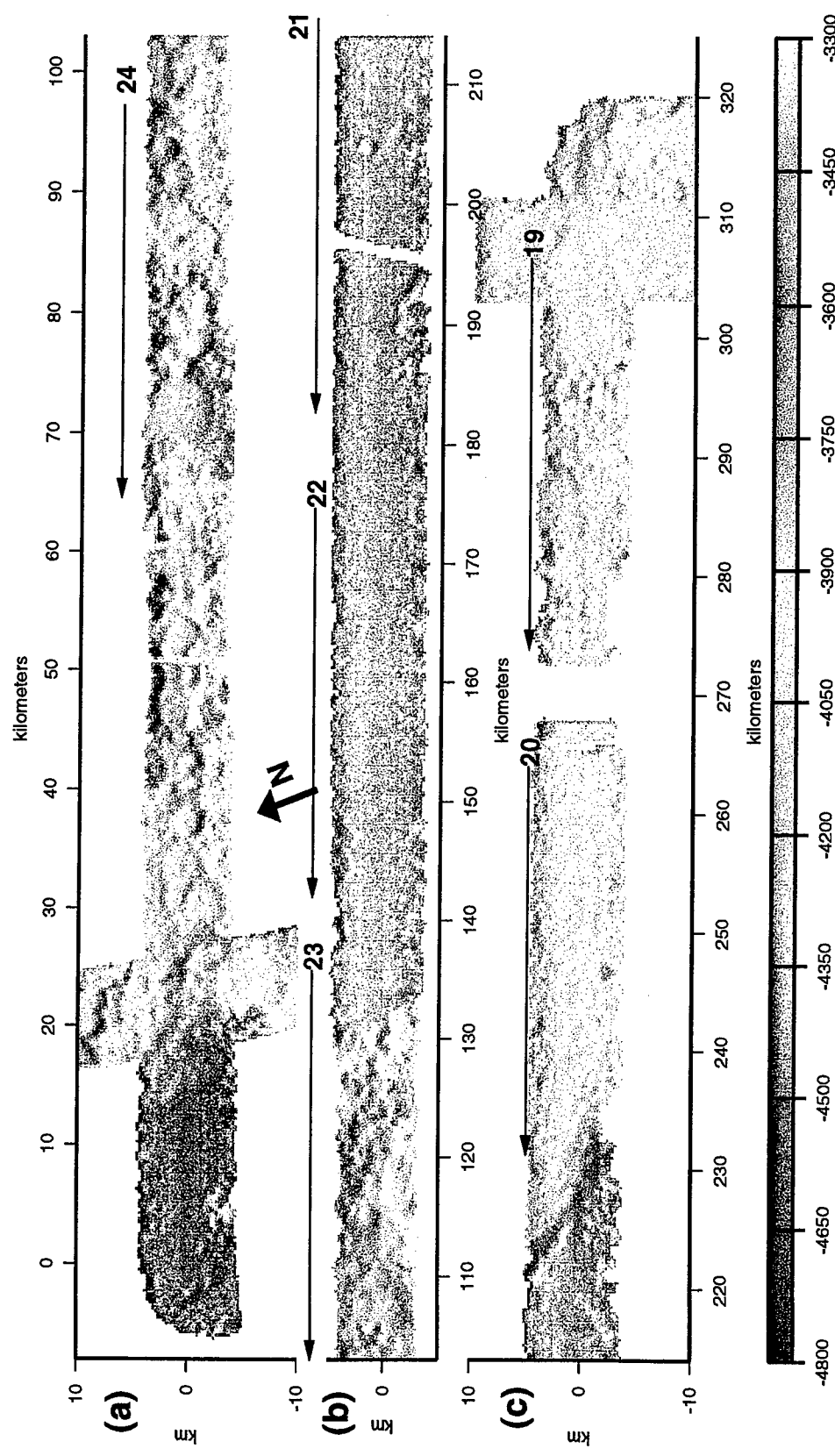


Figure 5-9: Shaded relief Hydrosweep bathymetry of hummocky terrain on line A9. Oblique Mercator projection, arrow indicates north. The x-axis showing projected distance is the same as in Figure 5-8. The numbers indicate the locations of sonobuoy deployments, and the arrow the approximate ranges of sonobuoy data.

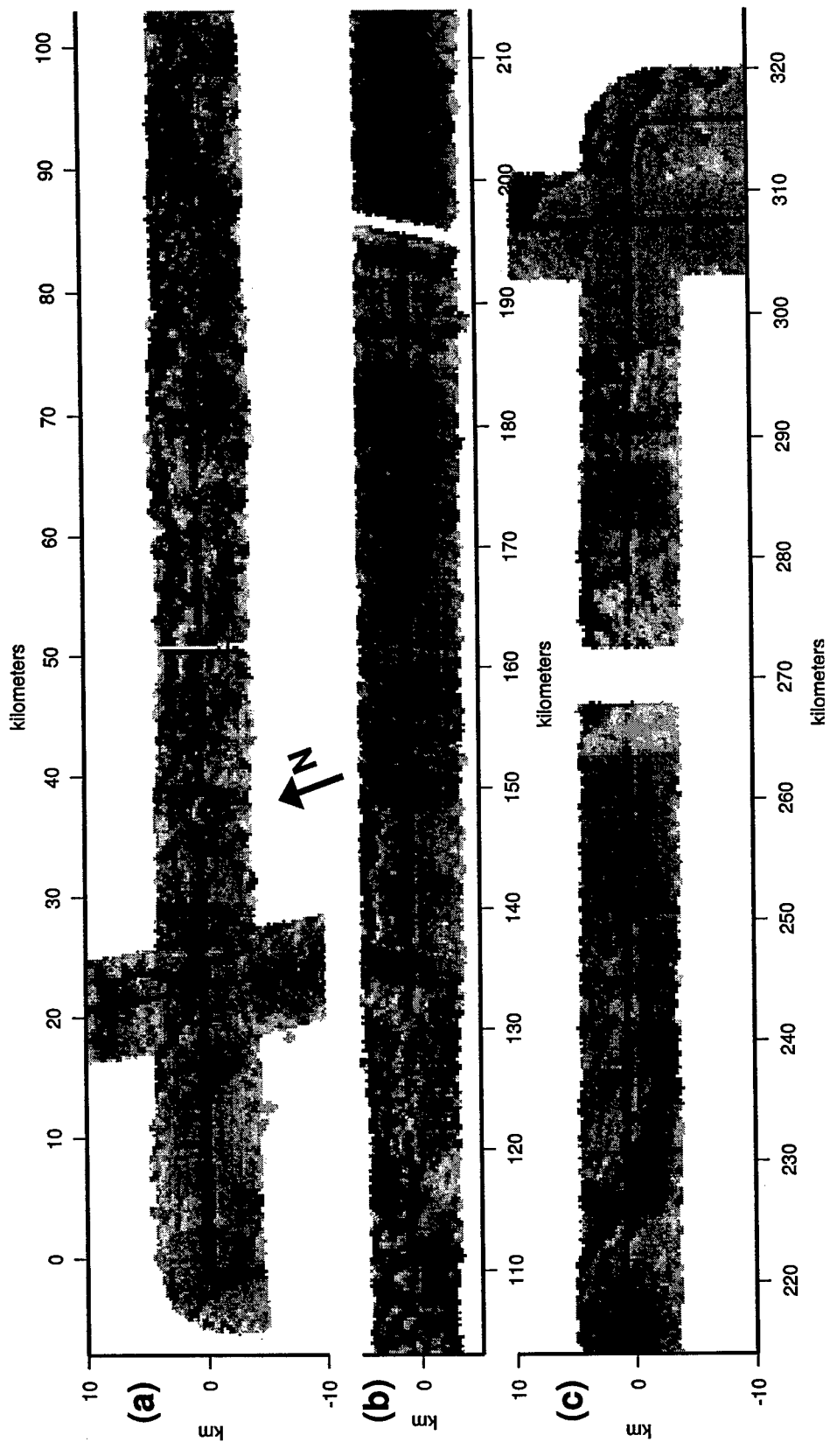


Figure 5-10: Grey shaded Hydrosweep amplitude data of hummocky terrain on line A9. High amplitudes are dark.

A further argument for the volcanic origins of both the smooth basement and the hummocky terrain is the likelihood of a common origin for the two features. The flat basement dips slightly away from the hummocky terrain, suggesting that voluminous lava flows could have originated there. The full extent of either the flat or the hummocky deposits is difficult to estimate with data limited to a single profile. If this volcanic interpretation of the south moat features is correct, this is yet another distinct type of volcanic feature, in addition to the three lines of seamounts described by *McNutt et al. [1997]* and in Chapter 4.

Clearly both volcanic and erosional processes are important in forming and modifying the features observed in the Hydrosweep and seismic data in and around the moat of the Austral Islands. A more definitive test of the origin of the proposed volcanic terrain to the south of the Austral Islands requires further study, and will be difficult with the sparse data currently available.

## 5.4 Discussion

Features analogous to those described in this chapter may be found in other island chains, many of which are better studied than the Australs. Bathymetric profiles of four Pacific island chains are shown in Figure 5-11, with corresponding seismic reflection profiles in Figures 5-12 through 5-15.

The Hawaiian Islands are the best studied island chain, if not the most typical. Thanks to near-100% sidescan sonar data coverage within 200 nautical miles of the islands [*Laughton, 1981*], large landslide deposits [*Moore et al., 1989*] and voluminous arch volcanism [*Clague et al., 1990*] have both been observed there. The flexural moat surrounding the islands is partially filled with sediments, largely terrigenous with an increasing pelagic fraction as distance from the islands increases.

The Marquesas Islands are a prime example of an archipelagic apron [*Menard,*

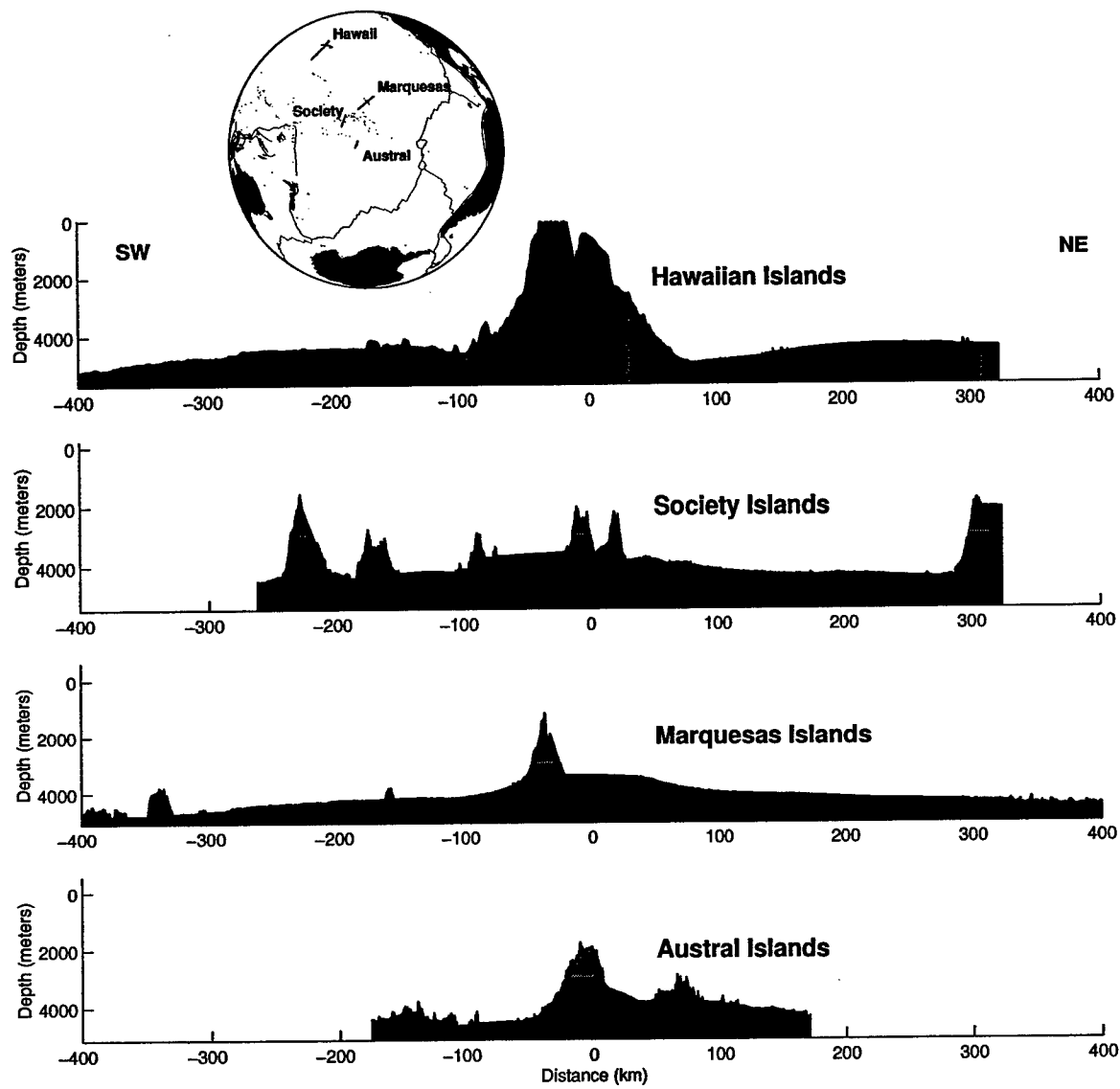
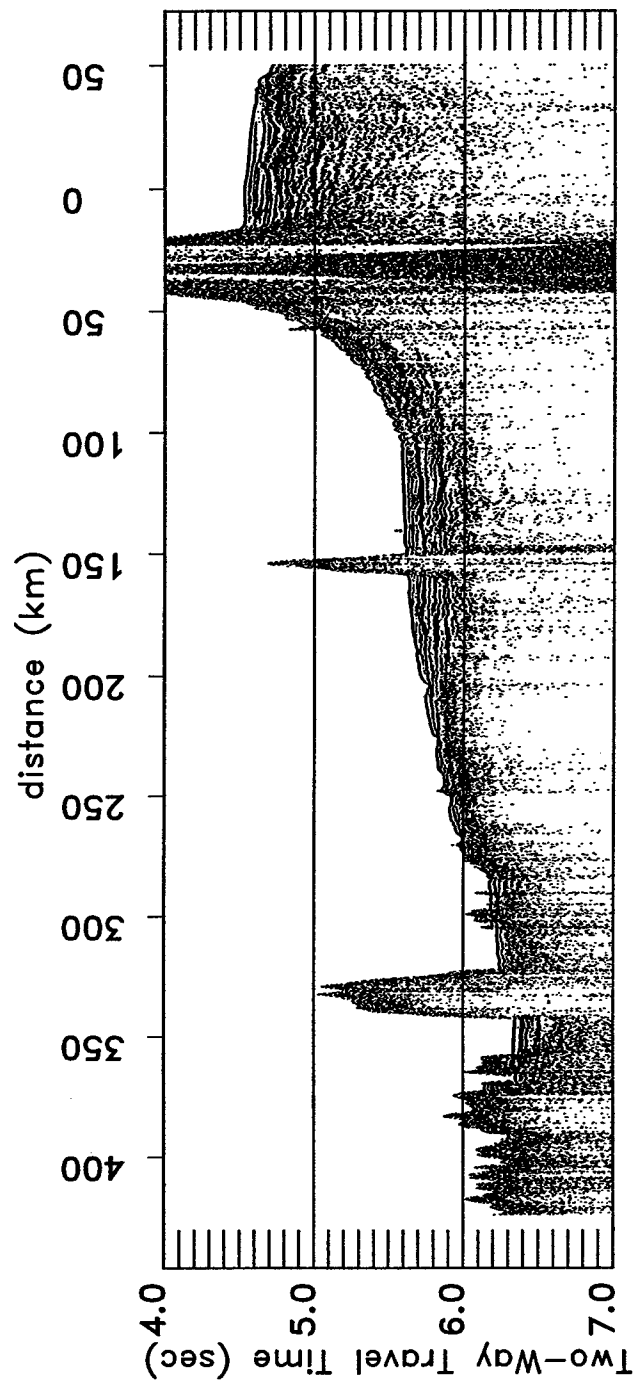
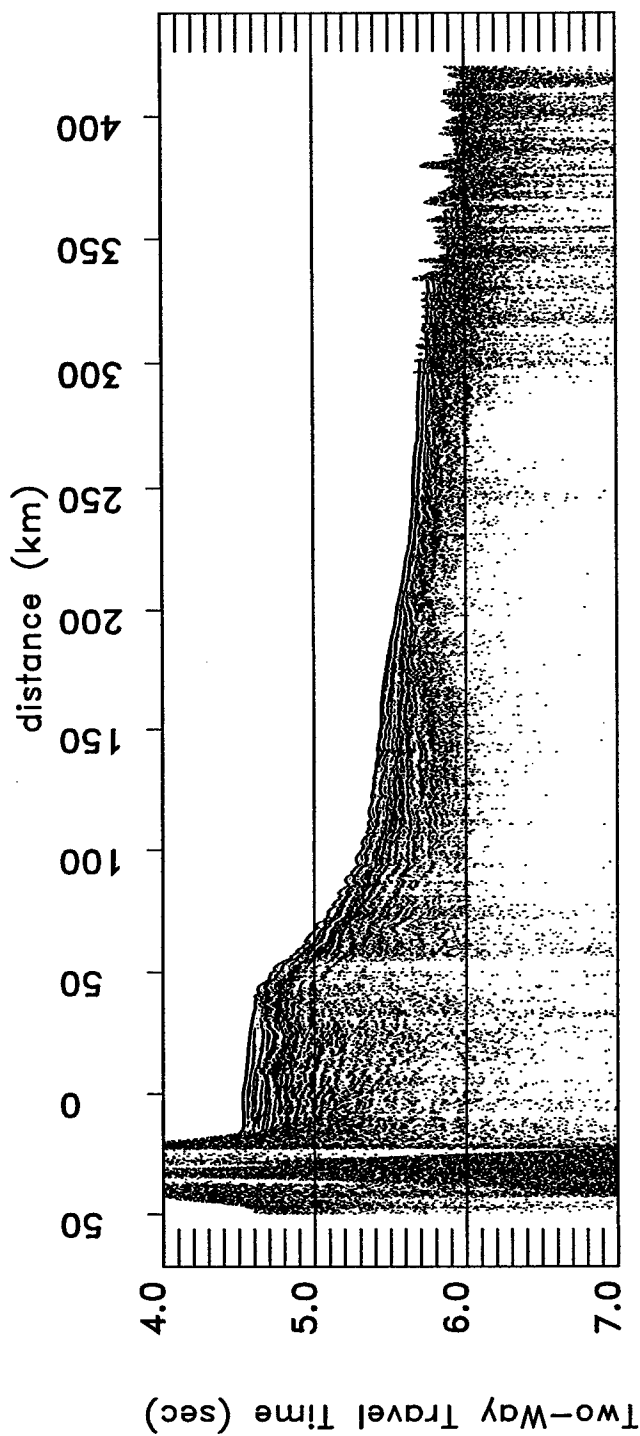


Figure 5-11: Bathymetric profiles of four Pacific island chains. All profiles are plotted at the same scale, with 22× vertical exaggeration. The base level of each profile is calculated from a *Parsons and Sclater* [1977] age-depth curve, using ages from the center of each profile as given by the crustal age map of *Müller et al.* [1997]. Each profile is projected into orthogonal distance from the axis of the volcanic chain. Data sources for Hawaii profile are R/V *Roger Revelle* leg KIWI03 and Geological Survey of Japan cruise GH7901 (provided by NGDC). Marquesas and Society profiles are data from R/V *Maurice Ewing* cruise EW9103, and Austral Islands data are from R/V *Maurice Ewing* cruise EW9602. Black portions of each profile are the regions shown in the seismic profiles in Figures 5-12 through 5-15.



(a) Southwest half of profile

Figure 5-12: EW9103 multichannel seismic profile 1162 across the Marquesas Islands, described by Wolfe *et al.* [1994]. Southwest is to the left.



(b) Northeast half of profile

Figure 5-12: (continued)

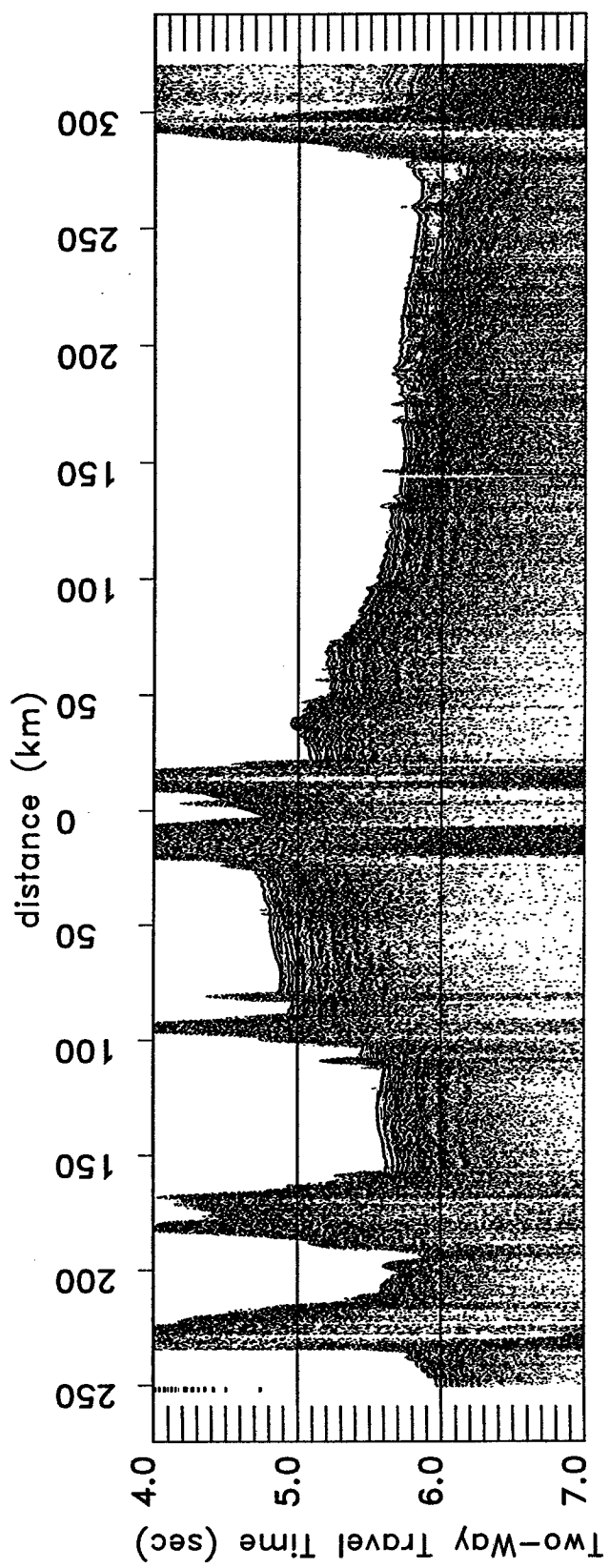


Figure 5-13: EW9103 multichannel seismic profile 1164 across the Society Islands. Southwest is to the left, with the Savannah Seamounts on the left side of the figure and the Tuamotu Plateau to the right.

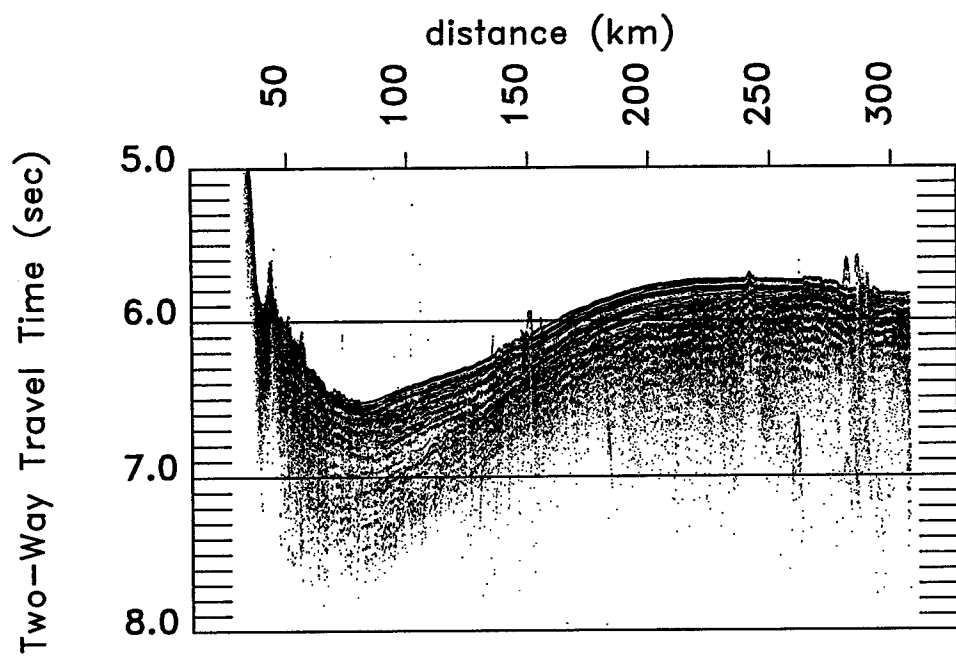


Figure 5-14: KIWI03 single channel seismic reflection profile across the Hawaiian Islands, near Oahu. Southwest is to the left.

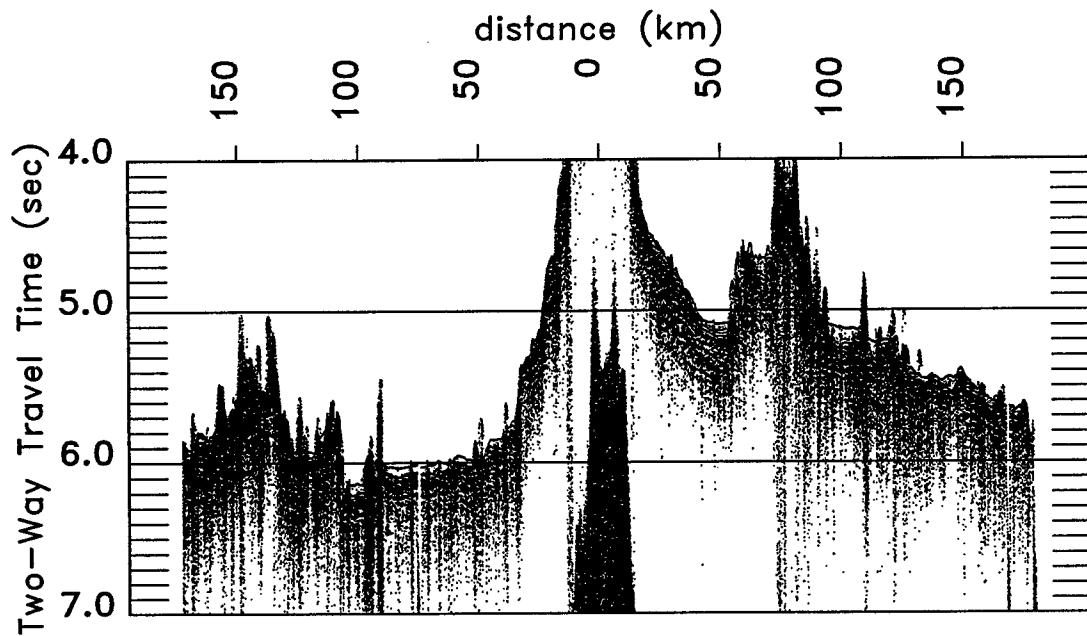


Figure 5-15: EW9602 MCS reflection profile across the Austral Islands, near Rapa. Southwest is to the left.

1959]. The broad, smooth topography extending from the base of the volcanic edifices, sloping gently upwards towards the islands, defines the Marquesas apron (see Figure 5-12). The Marquesas apron appears to consist of sediments derived from the central volcanic edifices and burying the abyssal seafloor to a distance of more than 300 km [Wolfe *et al.* [1994]].

H. W. Menard, when he first coined the term “archipelagic apron” in 1956, argued that most of the volume of the apron consists of submarine basalt flows emplaced *in situ*. Later studies [e.g., Rees *et al.*, 1993; Wolfe *et al.*, 1994] have found that much of the moat material is sediments derived from the volcanic edifices by mass wasting processes. However, data presented in this chapter support the notion that volcanic processes can contribute a significant amount of material to the archipelagic apron.

Large abyssal basalt flows are known to occur at mid-ocean ridges [e.g., Gregg *et al.*, 1996], and also on the Hawaiian arch [Clague *et al.*, 1990]. Their role in constructing an archipelagic apron is still unknown. Although Menard [1959] seems to have underestimated the quantity of material that could be derived from mass wasting of islands such as the Hawaiian and Marquesas Islands, his suggestion that *in situ* lava flows make up a significant proportion of the volume of the moat material has not been ruled out. At the Austral Islands and parts of the Society Islands, the sediments are thin compared with Hawaii and the Marquesas, and/or acoustically opaque. If the features described in this chapter are volcanic, then submarine fissure eruptions or flood basalts comprise a significant portion of the Austral apron. Perhaps *in situ* volcanism plays a role in the construction of other aprons as well.

A possible explanation for the varying proportions of volcanic material in the aprons of different island chains is that the sediment supply at large, reefless islands such as Hawaii and the Marquesas is quite high compared to the volume of fissure eruptions on the outer flanks and arch, while the sediment supply at reef-fringed islands such as the Societies or the smaller and mostly submarine Australs is much less, leading to a higher proportion of basalt flows in the apron.

## 5.5 Conclusion

Recent data from the Austral Islands imply the presence of lava flows on the seafloor in the flexural moat of the volcanic chain. Multibeam bathymetry data show that the archipelagic apron there is generally small in lateral extent (<50 km). In only one location on the mapped seafloor around the Austral Islands does the morphology fully fit the description of an archipelagic apron, where the seafloor is flat with no indication of abyssal hills. This region is crossed by only one multibeam survey line, so its full extent is not known, but it extends for over 100 km along the trend of the volcanic chain. Coincident multichannel seismic reflection and sonobuoy data indicate only a thin layer of sediments in the region, with high seismic velocities directly underneath, so this region of apron material is unlikely to consist of volcaniclastic sediments. Further, there is no nearby island which could have provided the source for the required quantity of mass wasting to fill the moat with sediments; therefore any sediments would have had to have been derived from nearby seamounts, which seems unlikely. The seafloor here has been paved over by abyssal basalt flows, probably associated with the Austral Islands volcanism.

# Chapter 6

## Discussion and Conclusion

When a thing was in my reach, I no longer wanted it; my delight lay in the desire. Everything which my mind could consistently wish for was attainable, as with all the ambitions of sane men, and when a desire gained head, I used to strive until I had just to open my hand and take it. Then I would turn away, content that it had been within my strength. I sought only to assure myself, and cared not a jot to make the others know it.

T. E. Lawrence, *The Seven Pillars of Wisdom*

### 6.1 Relative and absolute plate motions

Chapters 2 and 3 describe some of the evidence for and effects of small changes in Pacific-Farallon relative plate motion.

Tectonic studies of the results of past plate motion changes can enlighten and be enlightened by studies of active tectonics under the influence of relative plate motion changes. A counterclockwise rotation of 4–8° in Pacific-Cocos relative motion between 8° and 12° at the East Pacific Rise has occurred in the last few million years [Cox and Engebretson, 1985; Perram and Macdonald, 1990; Carbotte and Macdonald, 1992; Pockalny *et al.*, 1997; Pockalny, 1997]. There is evidence that the apparent Euler poles estimated from fracture zones during a plate reorganization do not change instantaneously. The change to a new spreading direction occurs more quickly at fracture zones that are put into extension by the plate motion change than those that are put into compression [Pockalny *et al.*, 1997]. Studies of the active tectonics are

important for understanding the edge forces and stresses affecting the plate and timing of tectonic effects, while studies of older lithosphere can provide a more complete history and show the end state of such a plate motion change.

*Wessel and Kroenke [1997b]* recently proposed that a recent change in the absolute motion of the Pacific plate explains these observations and others. Similarly, the Eocene plate motion change described in Chapter 3 may be related to the Pacific absolute plate motion change occurring at the Hawaiian-Emperor bend [e.g., *Clague and Dalrymple, 1987*]. One of the main difficulties in explaining the Hawaiian-Emperor bend in terms of an absolute plate motion change has been the lack of tectonic evidence of relative plate motion changes between the Pacific and neighboring plates [Norton, 1995]. One possibility is that the plate with the largest constructional boundary with the Pacific, the Farallon plate, was carried along with the Pacific plate as edge forcing changed because of a “locking” effect of the large offset fracture zones at the Pacific-Farallon Ridge. The stresses at this boundary may have caused the large propagating rift event that created the Adventure Trough [*Cande and Haxby, 1991*]. There was a relatively small resulting change in Pacific-Farallon motion [*Caress et al., 1988, Chapter 3*], but it was much less than would have occurred if the absolute motions of the two plates were decoupled. However, the timing of plate motion changes can be difficult to resolve on timescales of less than  $\sim 10$  m.y. [*Vogt, 1986; Gripp and Gordon, 1998*]. Further data (e.g., fracture zone lineations digitized from satellite altimetry maps, better magnetic anomaly locations, and high resolution bathymetric surveys) that can constrain the timing and magnitude of the plate motion change and incorporating these data into models of the geodynamic processes that affect large-scale propagating rifts and interlocking transform faults may test the validity of this idea.

## 6.2 Midplate volcanism, lithospheric cracks and hotspots

The results presented in Chapter 4 on the elastic plate thickness beneath the volcanic loads in the Southern Austral region largely support the conclusions reached by *McNutt et al.* [1997] on the basis of 1-D flexural modeling and radiometric dating. One major difference between the one-dimensional loading models in *McNutt et al.* [1997] and the two-dimensional results presented here are that the 1-D models significantly underestimated the volume of the more recent volcanics (see Section 4.5.2) due to the axisymmetric nature of the loads of the Macdonald seamounts and the bias introduced by the locations of survey lines, which intentionally did not include the maximum of the volcanic load.

The values of  $T_e$  obtained for the Ngatemato Seamounts (0-2 km) are even lower than what would be expected for lithosphere 10–15 Ma at the time of loading, as implied by the radiometric dates obtained from two dredge samples from the chain [*McNutt et al.*, 1997]. The Puka Puka seamount chain shows a similar anomalously low rigidity, which may be partly accounted for by the fracturing of the lithosphere [*Goodwillie*, 1995]. A broken plate model [*Wessel*, 1996] may be a more appropriate representation of the lithospheric flexure beneath Ngatemato than the continuous plate approach used in Chapter 4. However, neither a broken plate by itself nor a curvature-dependent flexural rigidity model [*Wessel*, 1993] can fully explain the low  $T_e$ .

The flexural rigidity of the lithosphere beneath the recent volcanic loads in the Austral Islands is not well constrained. Modeling results from Chapter 4 suggest a value of  $T_e$  between 10 and 20 km, but the error bars are large (see Table 4.3). These results are not sufficient to resolve models of abnormally low [*Calmant and Cazenave*, 1987] or normal [*Filmer et al.*, 1993] elastic thicknesses in the southern part of the Superswell region.

## 6.3 Flood basalts in archipelagic aprons

I proposed in Chapter 5 that the morphology of a region of flat seafloor south of Marotiri may be due to the paving over of abyssal hill topography by flood basalts.

The distances between Rapa and Marotiri (99 km) and between Ra and Macdonald Seamounts (95 km) are nearly the same, and about the same as the distance from the flat moat terrain from Marotiri (see Figure 6-1). This distance is about the distance to the maximum of the arch for the point loading of a 8 km elastic plate.

Regular spacing of volcanoes is observed in many other midplate chains [Vogt, 1974; Moore and Clague, 1992]. *ten Brink* [1991] proposed that the radius to the inflection point of flexural stresses controls the spacing of volcanoes. However, the volcano spacing shown in Figure 6-1 is significantly larger than the inflection radius, and more nearly the peak of the flexural arch, similar to the North Arch volcanic field north of Oahu [Clague *et al.*, 1990].

These observations suggest that basaltic flows may make up a significant portion of at least some archipelagic aprons. The proportion of *in situ* basalts to sediments may vary between island chains, as the sediment supply and flexural stresses differ.

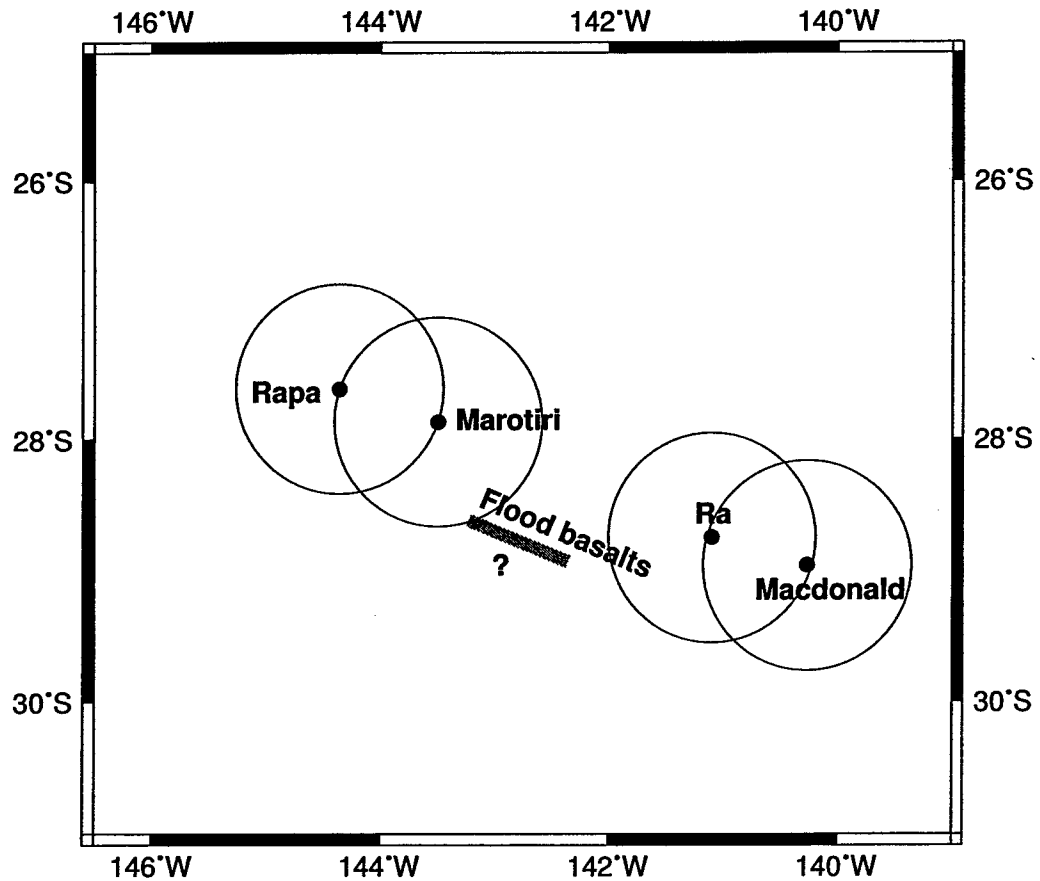


Figure 6-1: Schematic map of flexural arches of islands and large seamount of the Southern Australs. The locations of Rapa and Marotiri Islands and Ra and Macdonald Seamounts are shown by black dots. Circle with radius 100 km (corresponding to the distance of maximum extensional stresses at the top of the lithosphere for the point loading of an elastic plate with  $T_e = 8$  km,  $\rho = 2700$  kg/m $^3$ ) are centered at each of the named islands and seamounts. Macdonald and Marotiri are located at the arch of Ra and Rapa, respectively. The flat-lying region of the moat proposed in Chapter 5 to be an abyssal flood basalt is shown in gray. Map limits are the same as in Figures 4-2, 5-1 and B-1.



## Appendix A

# Analytical Solutions to the Elastic Plate Equation

There was a craving to be famous; and a horror of being known to like being known. Contempt for my passion for distinction made me refuse every offered honour. I cherished my independence almost as did a Beduin, but my impotence of vision showed me my shape best in painted pictures, and the oblique overheard remarks of others best taught me my created impression. The eagerness to overhear and oversee myself was my assault on my inviolate citadel.

T. E. Lawrence, *The Seven Pillars of Wisdom*

I have used several analytical solutions to the elastic plate equation in the preceding chapters. Nowhere in the literature do they seem to be gathered in one place, so I have included them here. I have included solutions for the 2-D and axisymmetric cases for both infinitesimal and finite width, constant thickness loads on an infinite, unbroken plate. Many other analytical treatments exist, including solutions for a broken 2-D plate [e.g., *Turcotte and Schubert*, 1982], for the point-load response of a semi-infinite plate [*Wessel*, 1996], and a more complete treatment of the axisymmetric case [*Lambeck and Makiboglu*, 1980], as well as for stress-dependent flexural rigidity [*Wessel*, 1993]. This appendix is not intended to be exhaustive, but convenient.

The applications of elastic beam and plate theory to geological problems are well known, dating back to *Vening Meinesz* [1941]. The modeling of the ocean lithosphere as an elastic plate has been common since the advent of plate tectonics and

particularly since *Parsons and Sclater* [1977] developed a thermal framework for the thickening of the ocean lithosphere with age. Some of the notable applications have been to the loading of the lithosphere by islands and seamounts [e.g., *Walcott*, 1970; *Watts and Cochran*, 1974; *McNutt and Menard*, 1978; *Watts and ten Brink*, 1989], the bending of downgoing plates at subduction zones [e.g., *Turcotte et al.*, 1978; *Judge and McNutt*, 1991], and the evolution of fracture zones [e.g., *Sandwell and Schubert*, 1982; *Sandwell*, 1984; *Christeson and McNutt*, 1992].

The deflection  $w$  of an elastic plate floating on an inviscid fluid caused by a load  $h$  is governed by the equation

$$D\nabla^4 w + \Delta\rho_1 gw = -\Delta\rho_2 gh \quad (\text{A.1})$$

where  $\Delta\rho_1 = \rho_m - \rho_0$ , the difference in densities of the infilling material and the mantle,  $\Delta\rho_2 = \rho_v - \rho_w$ , the density difference between the volcanic load and seawater, and the flexural rigidity  $D$  is defined by

$$D = \frac{ET_e^3}{12(1-\sigma^2)} \quad (\text{A.2})$$

where  $E$  is Young's modulus,  $\sigma$  is Poisson's ratio, and  $T_e$  is the effective elastic thickness of the lithospheric plate.

Equation (A.1) is often solved in the Fourier domain, but analytical solutions for some special cases are useful.

## A.1 The 2-D case

The two-dimensional case of a line load at the origin  $V(x) = V_0 \delta(x)$  leads to the solution [*Turcotte and Schubert*, 1982]

$$w(x) = w_0 e^{-x/\alpha} \left( \cos \frac{x}{\alpha} + \sin \frac{x}{\alpha} \right), \quad x \geq 0 \quad (\text{A.3})$$

where

$$w_0 = \frac{V_0 \alpha^3}{8D} \quad (A.4)$$

and  $\alpha$  is the flexural parameter

$$\alpha = \left( \frac{4D}{\Delta \rho_1 g} \right)^{1/4}. \quad (A.5)$$

Positive  $w$  is defined as downward deflection. This solution changes sign at  $x/\alpha = 3\pi/4$  and the minimum at  $x/\alpha = \pi$  corresponds to the location of maximum of the flexural arch topography. Determining  $\alpha$  from the location of the flexural bulge is one of the simplest ways to estimate the effective elastic thickness  $T_e$ , but unfortunately  $\alpha$  depends on the value assumed for  $\Delta \rho_1$  as well. Also, the location of the flexural bulge due to a distributed load is different from this infinitesimal line load response.

The solution to (A.1) for an infinitely long load of constant thickness  $h$  and width  $2A$  centered at  $x = 0$  may be found by integration of (A.3):

$$w(x) = \frac{\Delta \rho_2 h}{2\Delta \rho_1} \left[ e^{-(x-A)/\alpha} \cos \left( \frac{x-A}{\alpha} \right) - e^{-(x+A)/\alpha} \cos \left( \frac{x+A}{\alpha} \right) \right] \quad (A.6)$$

for  $x \geq A$  and

$$w(x) = \frac{\Delta \rho_2 h}{2\Delta \rho_1} \left[ 2 - e^{(x-A)/\alpha} \cos \left( \frac{x-A}{\alpha} \right) - e^{-(x+A)/\alpha} \cos \left( \frac{x+A}{\alpha} \right) \right] \quad (A.7)$$

for  $0 \leq x \leq A$ . Solutions for more complex line loads (such as a triangular or gaussian load) may also be found by integration, but in practice it is more convenient to approximate such loads by a finite sum of the solution given by (A.6) and (A.7). This solution approaches (A.3) for  $A \ll \alpha$  and Airy isostasy for  $A \gg \alpha$ . The behavior of the finite width loading solution when  $A$  is of the same order as  $\alpha$  is of interest.

Figure A-1 shows the deflection due to a constant magnitude load of varying width. Some important observations are that as the width of the load increases, both the amplitude of the deflection and the curvature of the plate (and thus the stresses in

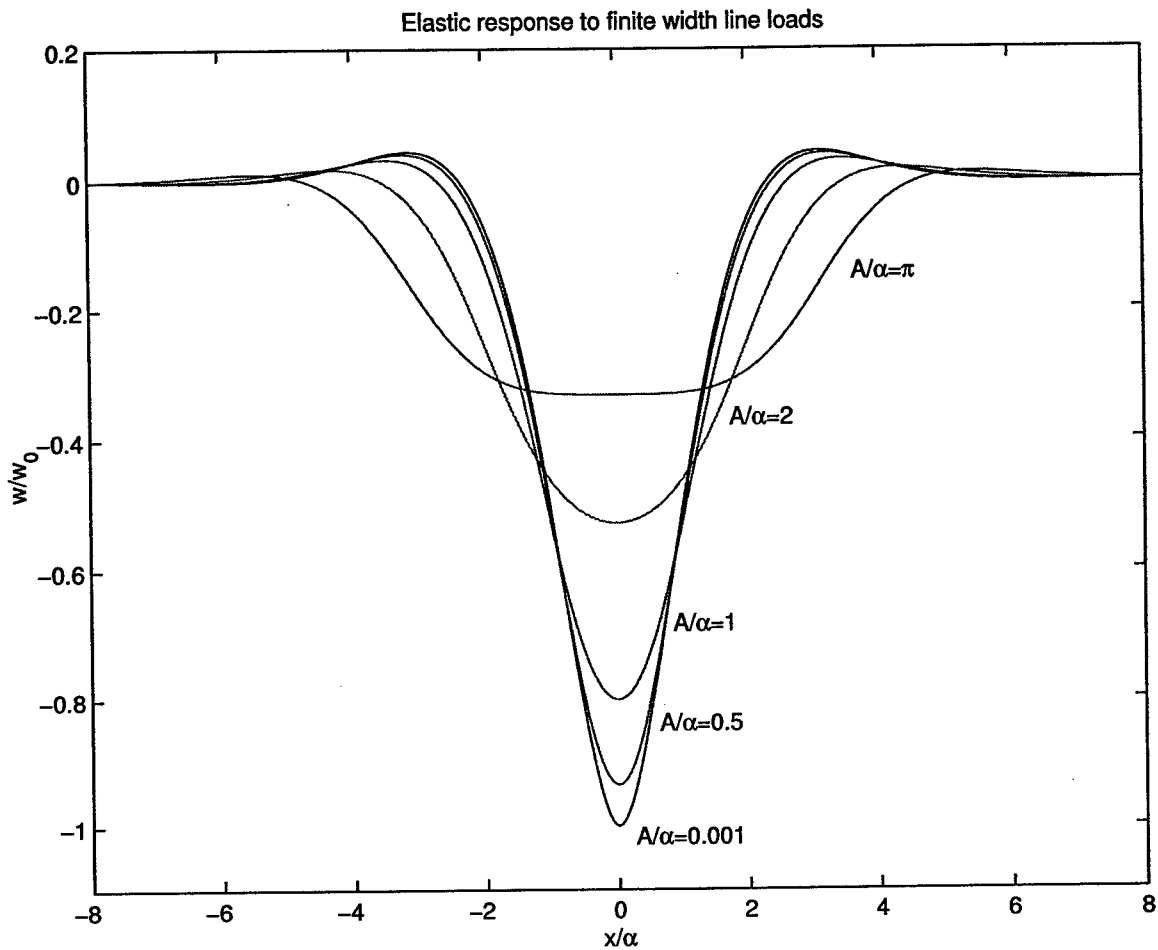


Figure A-1: The solution to the elastic plate equation for a finite width line load of varying width  $A$  with a constant total mass. The curve for  $A/\alpha = 0.001$  is indistinguishable on this scale from the infinitesimal line load solution given by equation (A.3).

the plate) at  $x = 0$  decrease, while the location of the flexural bulge moves outward. Some of these effects are shown in figure A-2.

A realistic value for the Hawaiian Islands, where the half width of the load is about 70 km and the distance from the center of the load to the flexural bulge is about 250 km, would be  $A/\alpha \approx 1$ . For younger, weaker plates, the ratio  $A/\alpha$  could easily be much higher. For example, the Ngatemato Seamounts discussed in Chapter 4 correspond to  $A/\alpha$  between 2 and 3.

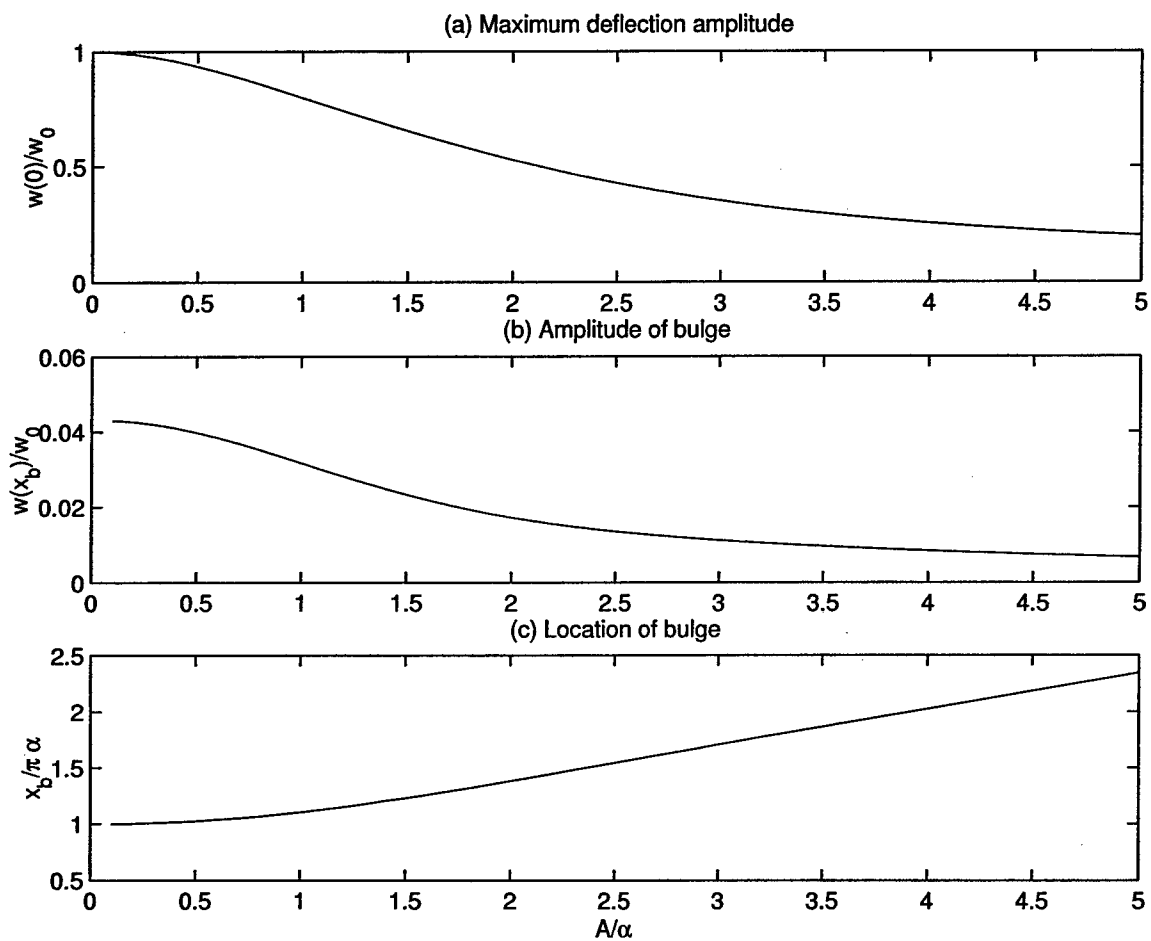


Figure A-2: The effect of varying the width  $A$  of a distributed load on a 2-D elastic plate on (a) the maximum deflection at  $x = 0$ , (b) the amplitude of the flexural bulge, and (c) the location of the flexural bulge.

## A.2 The axisymmetric case

The general solution to (A.1) for an axisymmetric load on an infinite plate may be expressed in terms of zero-order Kelvin-Bessel functions [McNutt and Menard, 1978]:

$$w(r) = C_1 \text{Ber} \left( \frac{r\sqrt{2}}{\alpha} \right) + C_2 \text{Bei} \left( \frac{r\sqrt{2}}{\alpha} \right) + C_3 \text{Ker} \left( \frac{r\sqrt{2}}{\alpha} \right) + C_4 \text{Kei} \left( \frac{r\sqrt{2}}{\alpha} \right) \quad (\text{A.8})$$

where the constants  $C_i$  depend on the geometry of the load. The flexural parameter  $\alpha$  here is defined as in (A.5), which differs by a factor of  $\sqrt{2}$  from the value of the flexural parameter used in most published solutions for the axisymmetric case.

For a point load  $q$  at  $r = 0$ , (A.8) becomes [Lambeck and Makiboglu, 1980]:

$$w(r) = -\frac{q\alpha^2}{2\pi D} \text{Kei} \left( \frac{r\sqrt{2}}{\alpha} \right) \quad (\text{A.9})$$

which, in analogy to (A.3) may be integrated to find the solution for a disk of constant thickness  $h$  with finite radius  $A$  [McNutt and Menard, 1978]:

$$w(r) = \frac{\Delta\rho_2 h}{\Delta\rho_1} \left[ \frac{A\sqrt{2}}{\alpha} \text{Ber}' \left( \frac{A\sqrt{2}}{\alpha} \right) \text{Ker} \left( \frac{r\sqrt{2}}{\alpha} \right) - \frac{A\sqrt{2}}{\alpha} \text{Bei}' \left( \frac{A\sqrt{2}}{\alpha} \right) \text{Kei} \left( \frac{r\sqrt{2}}{\alpha} \right) \right] \quad (\text{A.10})$$

for  $r \geq A$  and

$$w(r) = \frac{\Delta\rho_2 h}{\Delta\rho_1} \left[ 1 + \frac{A\sqrt{2}}{\alpha} \text{Ker}' \left( \frac{A\sqrt{2}}{\alpha} \right) \text{Ber} \left( \frac{r\sqrt{2}}{\alpha} \right) - \frac{A\sqrt{2}}{\alpha} \text{Kei}' \left( \frac{A\sqrt{2}}{\alpha} \right) \text{Bei} \left( \frac{r\sqrt{2}}{\alpha} \right) \right] \quad (\text{A.11})$$

for  $0 \leq r \leq A$ , where primes indicate differentiation.

The relation of the finite to the infinitesimal loading solutions is quite similar to the two-dimensional case already discussed. Again, more complex axisymmetric loads may be solved for (and some are given by Lambeck and Makiboglu [1980]), but for most applications a finite sum of the solution given by (A.10) and (A.11) is adequate.

## Appendix B

### Seismic Reflection Data

This appendix contains figures of available seismic reflection data in the Austral Islands, including the 6 long line survey of MCS data collected by EW9602, used in chapters 4 and 5. Also shown are two single channel profiles collected by R/V *Vema* in 1965.

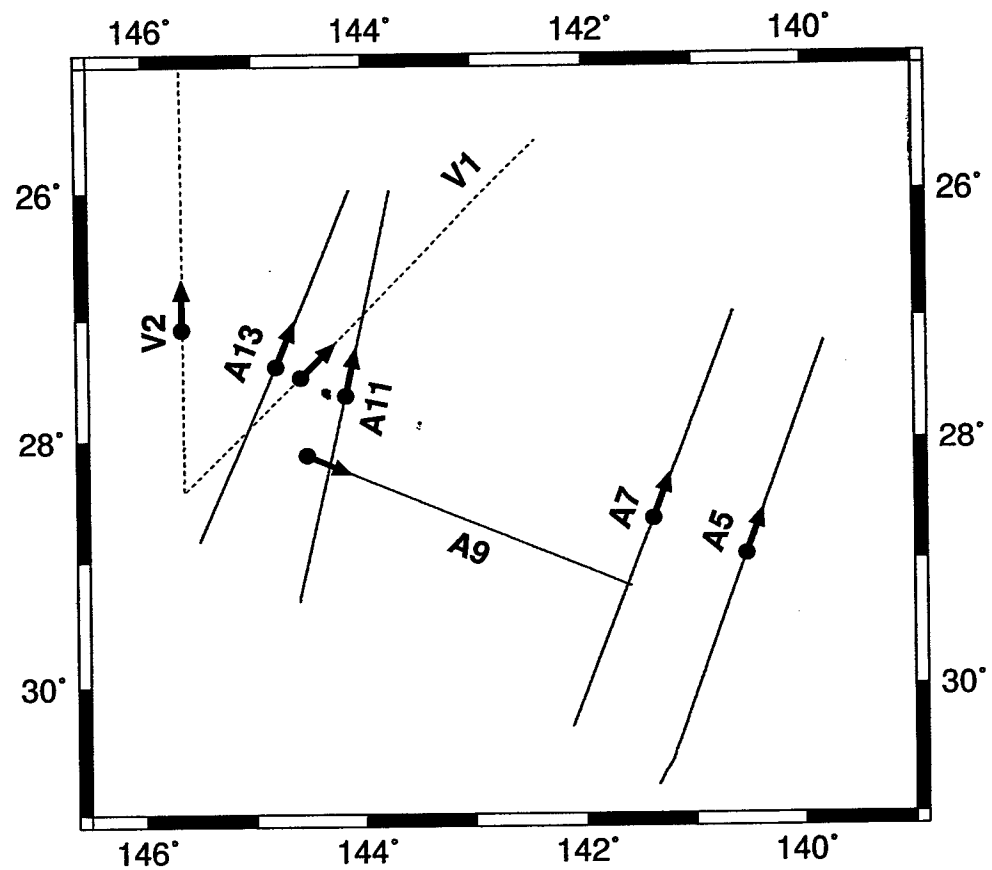


Figure B-1: Location map for seismic profiles presented in Appendix B. The five MCS lines collected by *R/V Maurice Ewing* are labeled A5–A13, and the two single channel profiles collected by *R/V Vema* are V1 and V2, indicated by dashed lines. Black circles with arrows show the origin and positive  $x$ -direction of the distance axis of the seismic section plots in this appendix. See Figure 4-2 for the bathymetry of this region.

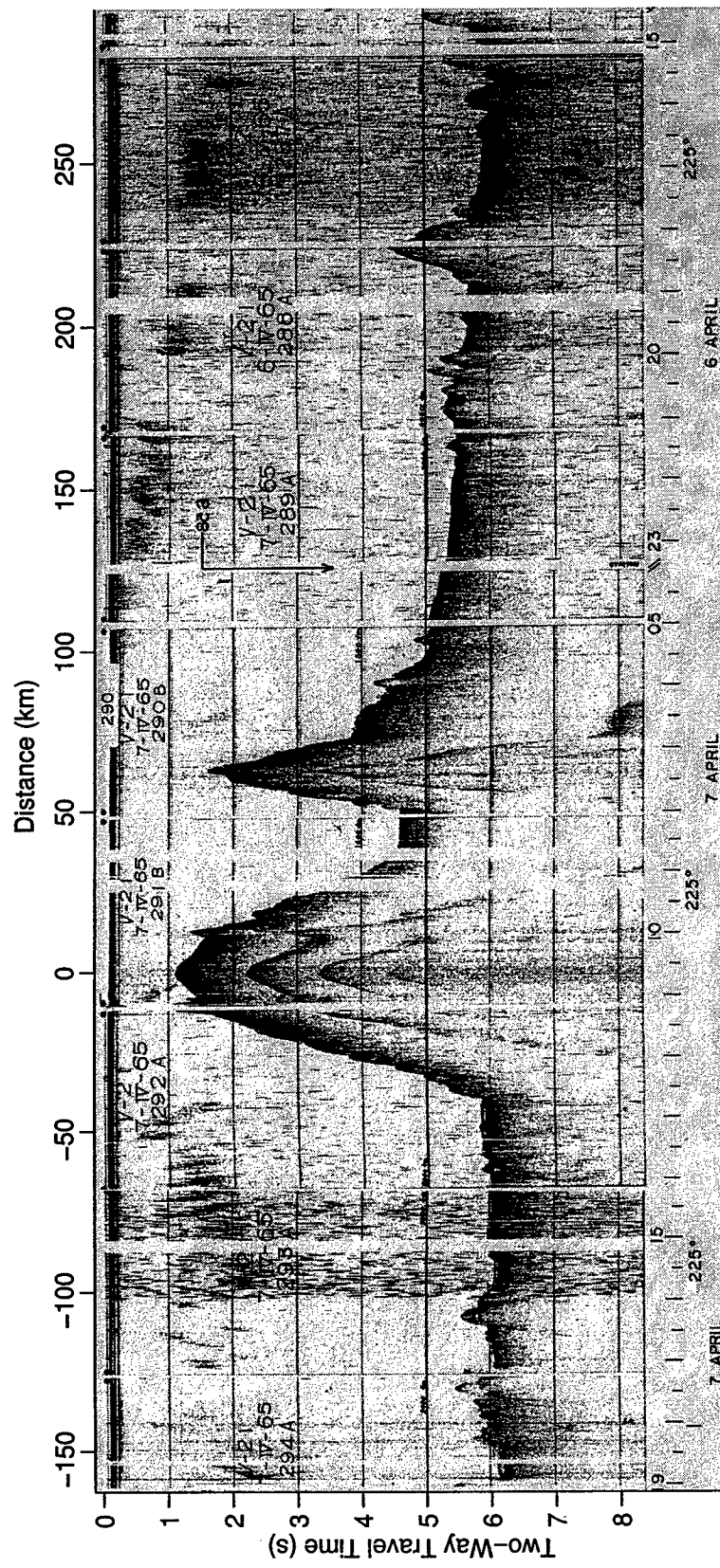


Figure B-2: *R/V Vema* single-channel seismic profile V1 across Austral Islands. Northeast is to the right and the horizontal axis is labeled at the bottom in hours of shipboard time and at the top with an approximate distance scale. Data, provided by NGDC as a digital image of the photographic plate made from the original analog shipboard records.

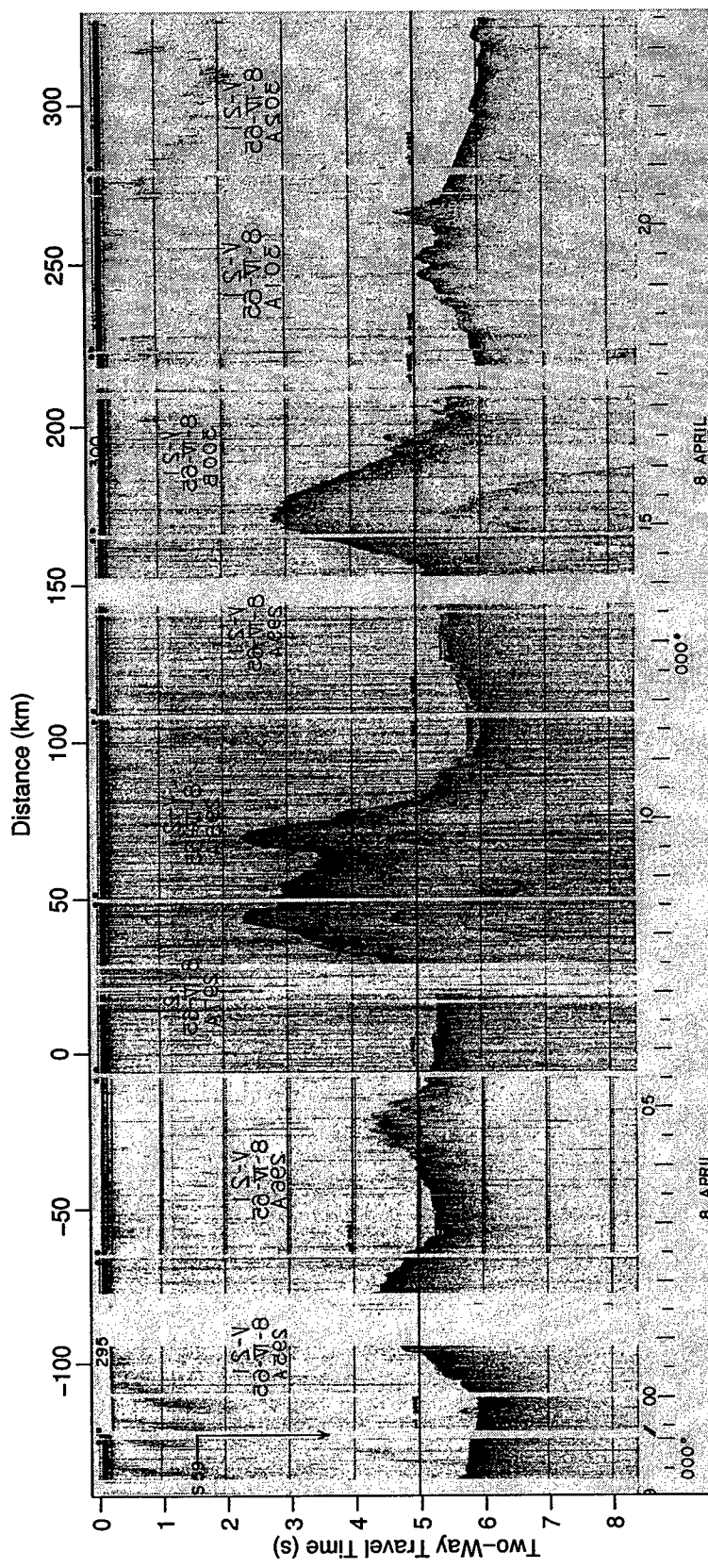


Figure B-3: *R/V Vema* single-channel seismic profile V2 across Austral Islands. Profile is oriented south-north, with north to the right. The horizontal axis is labeled at the bottom in hours of shipboard time and at the top with an approximate distance scale. Data provided by NGDC as a digital image of the photographic plate made from the original analog shipboard records.

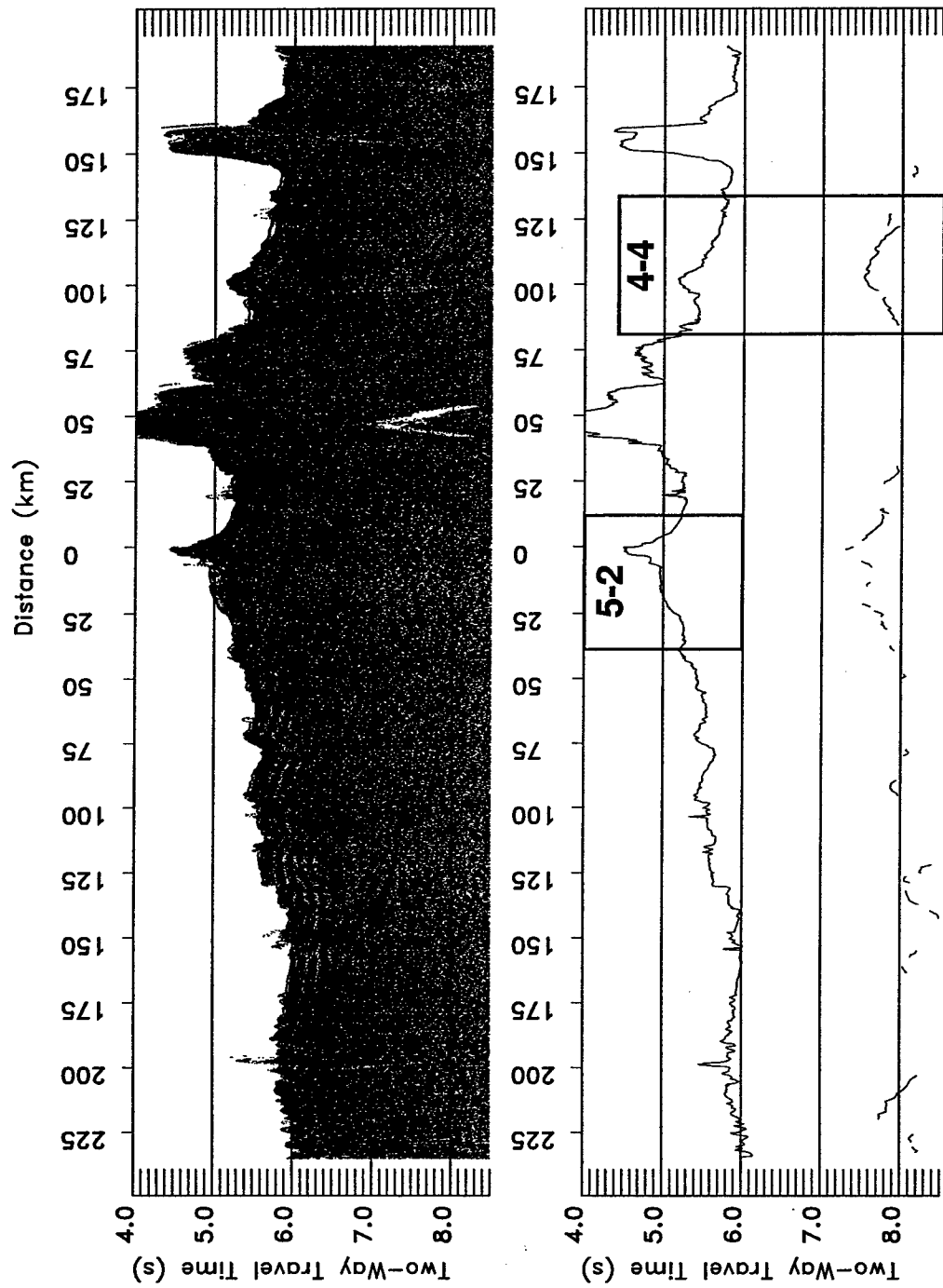


Figure B-4: EW9602 multichannel seismic profile A5 across the Austral Islands (top). Southwest is to the left. AGC has been applied to the stacked seismic data before display. Bottom panel shows Hydrosweep center beam bathymetry (assuming that the water velocity is 750 m/s) and Moho picks for the same profile. The locations of the data shown in Figures 4-4 and 5-2 are shown as inset boxes.

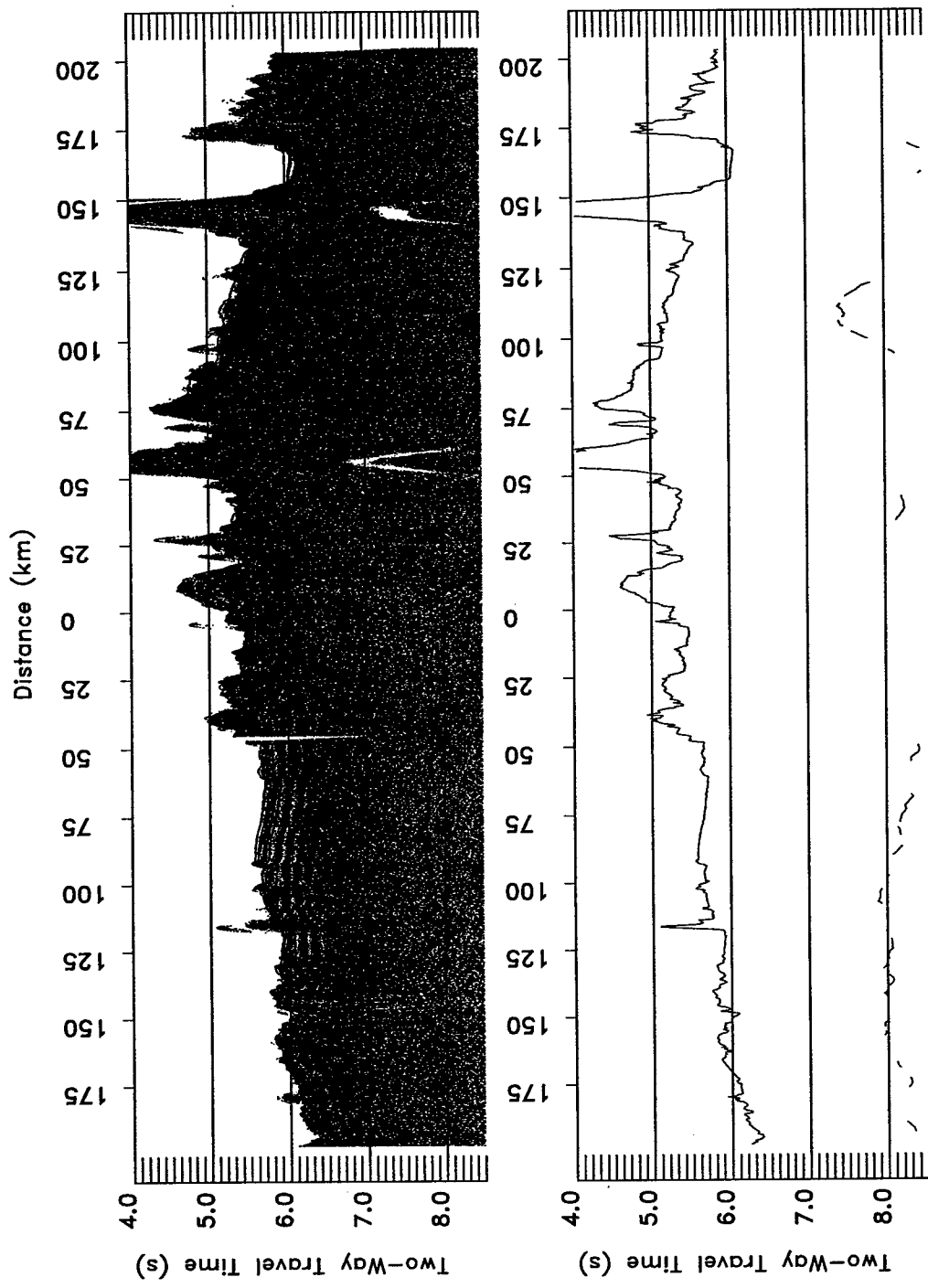


Figure B-5: EW9602 multichannel seismic profile A7 across the Austral Islands (top). Southwest is to the left. AGC has been applied to the stacked seismic data before display. Bottom panel shows Hydro-sweep center beam bathymetry (assuming that the water velocity is 750 m/s) and Moho picks for the same profile.

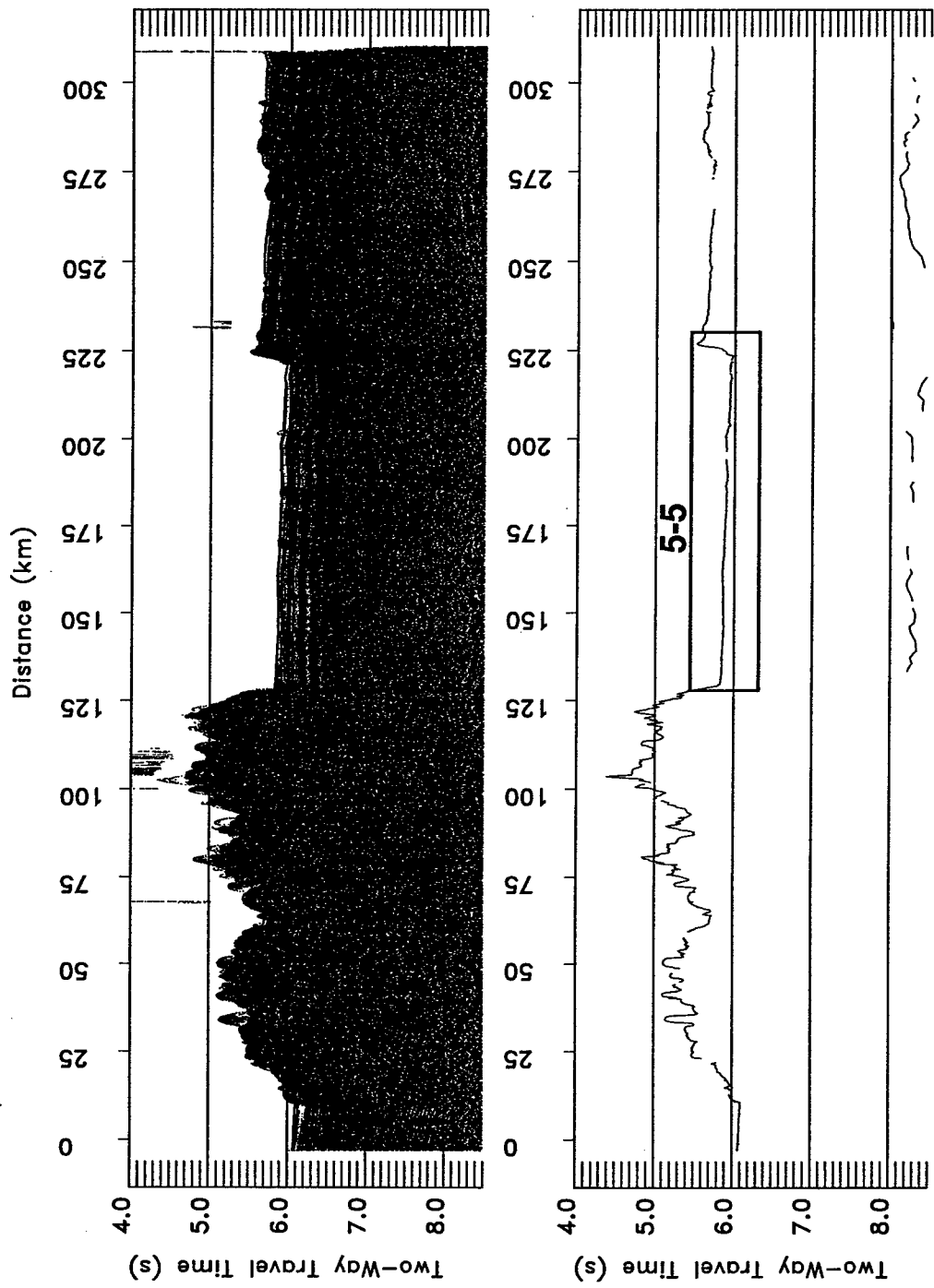


Figure B-6: EW9602 multichannel seismic profile A9 across the Austral Islands (top). Northwest is to the left. AGC has been applied to the stacked seismic data before display. Bottom panel shows Hydrosweep center beam bathymetry (assuming that the water velocity is 750 m/s) and Moho picks for the same profile. The location of the data shown in Figure 5-5 is shown as an inset box.

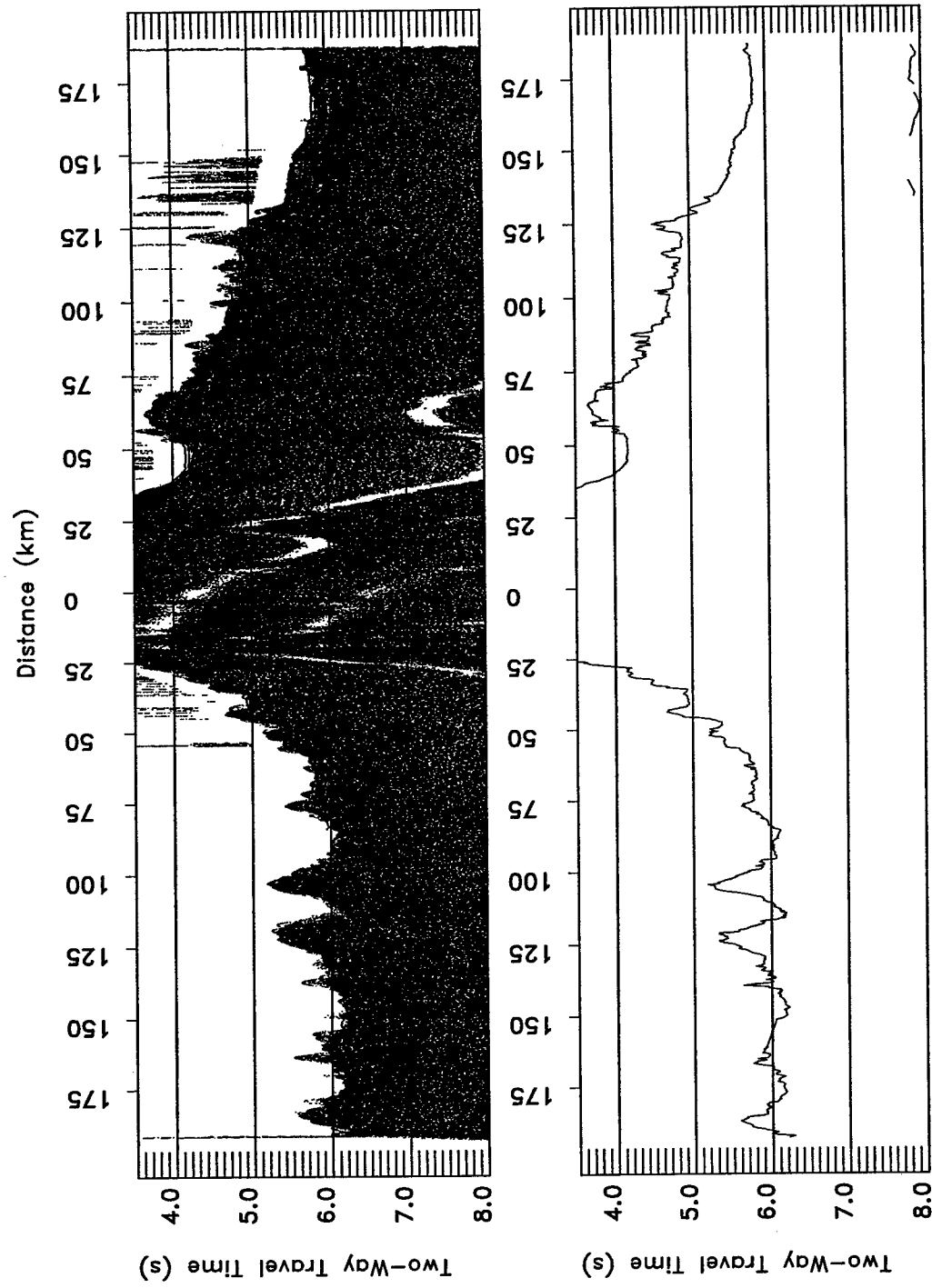


Figure B-7: EW9602 multichannel seismic profile A11 across the Austral Islands (top). Southwest is to the left. AGC has been applied to the stacked seismic data before display. Bottom panel shows Hydrosweep center beam bathymetry (assuming that the water velocity is 750 m/s) and Moho picks for the same profile.

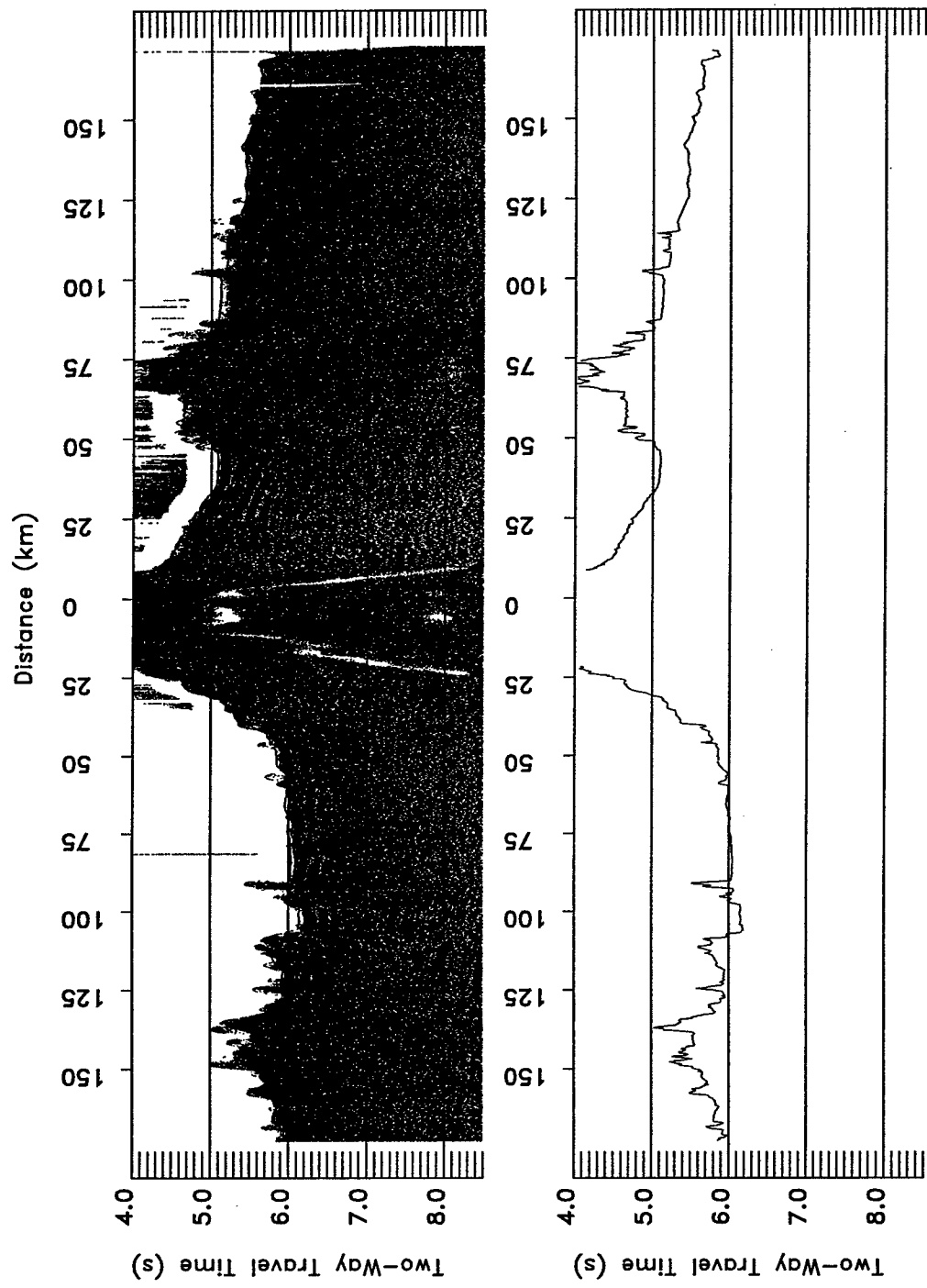


Figure B-8: EW9602 multichannel seismic profiles A13 and A14 across the Austral Islands (top). Southwest is to the left. AGC has been applied to the stacked seismic data before display. Bottom panel shows Hydrosweep center beam bathymetry (assuming that the water velocity is 750 m/s) and Moho picks for the same profile.



# Bibliography

Abrams, L. J., R. L. Larson, T. H. Shipley, and Y. Lancelot, Cretaceous volcanic sequences and Jurassic oceanic crust in the East Mariana and Pigafetta Basins of the Western Pacific, in *The Mesozoic Pacific: Geology, Tectonics, and Volcanism*, no. 77 in Geophysical Monograph Series, pp. 77–101, AGU, 1993.

Bell, R., and A. B. Watts, Evaluation of the BGM-3 sea gravimeter on board *R/V Conrad*, *Geophysics*, 51, 1480–1493, 1986.

Bemis, K. G., and D. K. Smith, Production of small volcanoes in the Superswell region of the South Pacific, *Earth Planet. Sci. Lett.*, 118, 251–262, 1993.

Berggren, W. A., D. V. Kent, J. J. Flynn, and J. A. V. Couverling, Cenozoic geochronology, *Geol. Soc. Am. Bull.*, 96, 1407–1418, 1985.

Bonatti, E., and C. G. A. Harrison, Hot lines in the Earth's mantle, *Nature*, 263, 402–404, 1976.

Bonneville, A., and M. McNutt, Shear strength of the great Pacific fracture zones, *Geophys. Res. Lett.*, 19, 2023–2026, 1992.

Calmant, S., The elastic thickness of the lithosphere in the Pacific Ocean, *Earth Planet. Sci. Lett.*, 1987.

Calmant, S., and A. Cazenave, The effective elastic lithosphere under the Cook-Austral and Society Islands, *Earth Planet. Sci. Lett.*, 77, 187–202, 1986.

Calmant, S., and A. Cazenave, Anomalous elastic thickness of the oceanic lithosphere in the south-central Pacific, *Nature*, 328, 236–238, 1987.

Cande, S. C., and W. F. Haxby, Eocene propagating rifts in the Southwest Pacific and their conjugate features on the Nazca Plate, *J. Geophys. Res.*, 96, 19,609–19,622, 1991.

Cande, S. C., and D. V. Kent, Revised calibration of the geomagnetic polarity time scale for the Late Cretaceous and Cenozoic, *J. Geophys. Res.*, 100, 6093–6095, 1995.

Cande, S. C., J. L. LaBrecque, R. L. Larson, W. C. P. III, X. Golovchenko, and W. F. Haxby, *Magnetic Lineations of the World's Ocean Basins*, American Association of Petroleum Geologists, Tulsa, 1989, scale 1:27,400,000.

Carbotte, S. M., and K. C. Macdonald, East Pacific Rise 8°–10°30': Evolution of ridge segments and discontinuities from SeaMARC II and three-dimensional magnetic studies, *J. Geophys. Res.*, 97, 6959–6982, 1992.

Caress, D. W., H. W. Menard, and R. N. Hey, Eocene reorganization of the Pacific-Farallon spreading center north of the Mendocino Fracture Zone, *J. Geophys. Res.*, 93, 2813–2838, 1988.

Caress, D. W., M. K. McNutt, R. S. Detrick, and J. C. Mutter, Seismic imaging of hotspot-related crustal underplating beneath the Marquesas Islands, *Nature*, 373, 600–603, 1995.

Caress, D. W., J. R. Reynolds, M. K. McNutt, and K. A. Jordahl, Unusual morphology of Ngatemato Seamounts in the Southern Austral Islands, *EOS Trans. AGU 1997 Fall Meeting Suppl.*, 78, F726, 1997.

Cherry-Garrard, A. G. B., *The Worst Journey in the World*, 2nd ed., Carroll & Graf, New York, 1997, first published 1937.

Christeson, G. L., and M. K. McNutt, Geophysical constraints on the shear stress along the Marquesas Fracture Zone, *J. Geophys. Res.*, 97, 4425–4437, 1992.

Clague, D. A., and G. B. Dalrymple, The Hawaiian-Emperor volcanic chain: Part I. Geologic evolution, *U. S. Geol. Surv. Prof. Paper*, 1350, 5–54, 1987.

Clague, D. A., R. T. Holcomb, J. M. Sinton, R. S. Detrick, and M. E. Torresan, Pliocene and Pliostocene alkalic flood basalts on the seafloor north of the Hawaiian Islands, *Earth Planet. Sci. Lett.*, 98, 175–191, 1990.

Cox, A. V., and D. C. Engebretson, Change in motion of the Pacific plate at 5 m.y. B. P., *Nature*, 313, 474–474, 1985.

Darwin, C., *Voyage of the Beagle*, Penguin, New York, 1989, first published 1839.

Duncan, R. A., and D. A. Clague, Pacific plate motion recorded by linear volcanic chains, in *The Pacific Ocean*, edited by A. E. M. Nairn, F. G. Stehli, and S. Uyeda, vol. 7A of *The Ocean Basins and Margins*, chap. 3, pp. 89–121, Plenum Press, New York, 1986.

Engebretson, D. C., A. Cox, and R. G. Gordon, Relative motions between oceanic plates of the Pacific Basin, *J. Geophys. Res.*, 89, 10,291–10,310, 1984.

Ewing, J., and R. Houtz, Mantle reflections in airgun-sonobuoy profiles, *J. Geophys. Res.*, 74, 6706–6709, 1969.

Filmer, P. E., M. K. McNutt, and C. J. Wolfe, Elastic thickness of the lithosphere in the Marquesas and Society Islands, *J. Geophys. Res.*, 98, 19,565–19,577, 1993.

Filmer, P. E., M. K. McNutt, H. Webb, and D. Dixon, Volcanism and archipelagic aprons in the Marquesas and Hawaiian Islands, *Marine Geophys. Res.*, 16, 385–406, 1994.

Fischer, K., M. K. McNutt, and L. Shure, Thermal and mechanical constraints on the lithosphere beneath the Marquesas Islands, *Nature*, 322, 733–736, 1986.

Fleitout, L., and C. Moriceau, Short-wavelength geoid, bathymetry and the convective pattern beneath the Pacific Ocean, *Geophys. J. Int.*, 110, 6–29, 1992.

Fornari, D. J., D. G. Gallo, M. H. Edwards, J. A. Madsen, M. R. Perfit, and A. N. Shor, Structure and topography of the Siqueiros transform fault system: Evidence for the development of intra-transform spreading centers, *Mar. Geophys. Res.*, pp. 263–299, 1989.

Goodwillie, A. M., Short-wavelength gravity lineations and unusual flexure results at the Puka Puka volcanic ridge system, *Earth Planet. Sci. Lett.*, 136, 297–314, 1995.

Goodwillie, A. M., and A. B. Watts, An altimetric and bathymetric study of elastic thickness in the central Pacific Ocean, *Earth Planet. Sci. Lett.*, 118, 311–326, 1993.

Gregg, T. K. P., D. J. Fornari, M. R. Perfit, R. M. Haymon, and J. H. Fink, Rapid emplacement of a mid-ocean ridge lava flow on the East Pacific Rise at 9°46' – 51' N, *Earth Planet. Sci. Lett.*, 144, E1–E7, 1996.

Gripp, A. E., and R. G. Gordon, An assumption tested model of current plate velocity relative to the hotspots, in *Evolution of Ocean Island Volcanoes: Penrose Conference Program and Abstract Volume*, p. 35, Geological Society of America, 1998.

Handschoenmacher, D. W., Post-Eocene plate tectonics of the Eastern Pacific, in *The Geophysics of the Pacific Ocean Basin and its Margins*, edited by G. H. Sutton, no. 19 in *Geophys. Monogr. Ser.*, pp. 177–202, AGU, 1976.

Haxby, W. F., and J. K. Weissel, Evidence for small-scale mantle convection from Seasat altimeter data, *J. Geophys. Res.*, 91, 3507–3520, 1986.

Hey, R. N., H. W. Menard, T. M. Atwater, and D. W. Caress, Changes in direction of seafloor spreading revisited, *J. Geophys. Res.*, 93, 2803–2811, 1988.

Jackson, E. D., and H. R. Shaw, Stress fields in central portions of the Pacific plate: Delineated in time by linear volcanic chains, *J. Geophys. Res.*, 80, 1861–1874, 1975.

Johnson, R. H., and A. Malahoff, Relation of Macdonald Volcano to migration of volcanism along the Austral chain, *J. Geophys. Res.*, **76**, 3282–3290, 1971.

Jordahl, K. A., M. K. McNutt, H. F. Webb, S. E. Kruse, and M. G. Kuykendall, Why there are no earthquakes on the Marquesas Fracture Zone, *J. Geophys. Res.*, **100**, 24,431–24,447, 1995.

Jordahl, K. A., M. K. McNutt, and H. Zorn, Pacific-Farallon relative motion 42–59 Ma determined from magnetic and tectonic data from the Southern Austral Islands, *Geophys. Res. Lett.*, **25**, 2869–2872, 1998.

Judge, A. V., and M. K. McNutt, The relationship between plate curvature and elastic plate thickness: A study of the Peru-Chile trench, *J. Geophys. Res.*, **96**, 16,625–16,640, 1991.

Kruse, S. E., Magnetic lineations on the flanks of the Marquesas swell: implications for the age of the sea floor, *Geophys. Res. Lett.*, **15**, 573–576, 1988.

Kruse, S. E., Z. J. Liu, D. F. Naar, and R. A. Duncan, Effective elastic thickness of the lithosphere along the Easter Seamount Chain, *J. Geophys. Res.*, **102**, 27,305–27,317, 1997.

Kuykendall, M. G., S. E. Kruse, and M. K. McNutt, The effects of changes in plate motions on the shape of the Marquesas Fracture Zone, *Geophys. Res. Lett.*, **21**, 2845–2848, 1994.

Lambeck, K., and S. M. Makiboglu, Seamount loading and stress in the ocean lithosphere, *J. Geophys. Res.*, **85**, 6403–6418, 1980.

Lassiter, J. C., E. H. Hauri, and H. G. Barsczus, Influence of the Austral Fracture Zone on the composition of lavas from Raivavae, Austral Islands: Evidence for crustal assimilation during magma ascent and evolution, *EOS Trans. AGU 1998 Spring Meeting Suppl.*, 1998.

Laughton, A. S., The first decade of GLORIA, *J. Geophys. Res.*, **86**, 11,511–11,534, 1981.

Lawrence, T. E., *The Mint*, W. W. Norton, 1963, first published 1935.

Lawrence, T. E., *The Seven Pillars of Wisdom: A Triumph*, Anchor, New York, 1991, first published 1926.

Levitt, D. A., and D. T. Sandwell, Modal depth anomalies from multibeam bathymetry: Is there a South Pacific superswell?, *Earth Planet. Sci. Lett.*, **139**, 1–16, 1996.

Lonsdale, P., Tectonic and magmatic ridges in the Eltanin fault system, South Pacific, *Mar. Geophys. Res.*, 8, 203–242, 1986.

Mammerickx, J., The Foundation Seamounts: Tectonic setting of a newly discovered seamount chain in the South Pacific, *Earth Planet. Sci. Lett.*, 113, 292–306, 1992.

Mammerickx, J., and D. Sandwell, Rifting of old oceanic lithosphere, *J. Geophys. Res.*, 91, 1975–1988, 1986.

Mardia, K. V., *Statistics of Directional Data*, Academic Press, London, 1972.

Mayes, C. L., L. A. Lawver, and D. T. Sandwell, Tectonic history and new isochron chart of the South Pacific, *J. Geophys. Res.*, 95, 8543–8567, 1990.

McNutt, M. K., Superswells, *Reviews of Geophysics*, 36, 211–244, 1998.

McNutt, M. K., and K. M. Fischer, The South Pacific Superswell, in *Seamounts, Islands and Atolls*, edited by B. H. Keating, P. Fryer, R. Batiza, and G. W. Boehlert, vol. 43 of *AGU Geophys. Monogr. Ser.*, pp. 25–34, 1987.

McNutt, M. K., and A. V. Judge, The superswell and mantle dynamics beneath the South Pacific, *Science*, 248, 969–975, 1990.

McNutt, M. K., and H. W. Menard, Lithospheric flexure and uplifted atolls, *J. Geophys. Res.*, 83, 1206–1212, 1978.

McNutt, M. K., K. Fischer, S. Kruse, and J. Natland, The origin of the Marquesas fracture zone ridge and its implications for the nature of hot spots, *Earth Planet. Sci. Lett.*, 91, 381–393, 1989.

McNutt, M. K., L. Sichoix, and A. Bonneville, Modal depths from shipboard bathymetry: There is a South Pacific Superswell, *Geophys. Res. Lett.*, 23, 3397–3400, 1996.

McNutt, M. K., D. W. Caress, J. Reynolds, K. A. Jordahl, and R. A. Duncan, Failure of plume theory to explain midplate volcanism in the Southern Austral Islands, *Nature*, 389, 479–483, 1997.

Menard, H. W., Archipelagic aprons, *Bull. Amer. Assoc. Petrol. Geol.*, 91, 13,915–13,923, 1959.

Menard, H. W., *Pacific Geology*, McGraw Hill, 1964.

Moore, J. G., and D. A. Clague, Growth of the island of Hawaii, *Geol. Soc. Am. Bull.*, 102, 1471–1484, 1992.

Moore, J. G., D. A. Clague, R. T. Holcombe, P. W. Lipman, W. R. Normark, and M. E. Torresan, Prodigious landslides on the Hawaiian Ridge, *J. Geophys. Res.*, **94**, 17,465–17,484, 1989.

Morgan, W. J., Convection plumes in the lower mantle, *Nature*, **230**, 42–43, 1971.

Müller, R. D., W. R. Roest, J.-Y. Royer, L. M. Gahagan, and J. G. Sclater, Digital isochrons of the world's ocean floor, *J. Geophys. Res.*, **102**, 3211–3214, 1997.

Nolasco, R., P. Tarits, J. H. Filloux, and A. D. Chave, Magnetotelluric imaging of the Society Islands hotspot, *J. Geophys. Res.*, 1998, in press.

Norton, I. O., Plate motions in the North Pacific: The 43 Ma nonevent, *Tectonics*, **14**, 1080–1094, 1995.

Okal, E. A., and R. Batiza, Hotspots: The first 25 years, in *Seamounts, Islands and Atolls*, edited by B. H. Keating, P. Fryer, R. Batiza, and G. W. Boehlert, vol. 43 of *AGU Geophys. Monogr. Ser.*, pp. 1–11, 1987.

Pardo-Casas, F., and P. Molnar, Relative motion for the Nazca (Farallon) and South America plates since late Cretaceous time, *Tectonics*, **6**, 233–248, 1987.

Parker, R. L., The rapid calculation of potential anomalies, *Geophys. J. R. Astron. Soc.*, **31**, 447–455, 1973.

Parmentier, E. M., and W. F. Haxby, Thermal stresses in the oceanic lithosphere: Evidence from geoid anomalies at fracture zones, *J. Geophys. Res.*, **91**, 7193–7204, 1986.

Parsons, B., and J. G. Sclater, An analysis of the variation of the ocean floor bathymetry and heat flow with age, *J. Geophys. Res.*, **82**, 803–827, 1977.

Perram, L. J., and K. C. Macdonald, A one-million year history of the 11°45' N East Pacific Rise discontinuity, *J. Geophys. Res.*, **95**, 21,363–21,381, 1990.

Pockalny, R. A., Evidence of transpression along the Clipperton Transform: Implications for processes of plate boundary reorganization, *Earth Planet. Sci. Lett.*, **146**, 449–464, 1997.

Pockalny, R. A., P. J. Fox, D. J. Fornari, K. C. Macdonald, and M. R. Perfit, Tectonic reconstruction of the Clipperton and Siqueiros fracture zones: Evidence and consequences of plate motion change for the last 3 Myr, *J. Geophys. Res.*, **102**, 3167–3181, 1997.

Rees, B. A., R. S. Detrick, and B. J. Coakley, Seismic stratigraphy of the Hawaiian flexural moat, *Geol. Soc. Am. Bull.*, **105**, 189–205, 1993.

Reynolds, J. R., D. A. Clague, and R. A. Duncan, Extinct and reactivated volcanoes: Austral Islands region, *EOS Trans. AGU 1997 Fall Meeting Suppl.*, 78, F780, 1997.

Rosa, J. W. C., and P. Molnar, Uncertainties in reconstructions of the Pacific, Farallon, Vancouver, and Kula plates and constraints on the rigidity of the Pacific and Farallon (and Vancouver) plates between 72 and 35 Ma, *J. Geophys. Res.*, 93, 2997–3008, 1988.

Saal, A. E., S. R. Hart, N. Shimizu, E. H. Hauri, and G. D. Layne, Pb isotopic variability in melt inclusions from oceanic island basalts, Polynesia, *Science*, 282, 1481–1484, 1998.

Sandwell, D., and G. Schubert, Lithospheric flexure at fracture zones, *J. Geophys. Res.*, 87, 4657–4667, 1982.

Sandwell, D. T., Thermomechanical evolution of oceanic fracture zones, *J. Geophys. Res.*, 89, 11,401–11,413, 1984.

Sandwell, D. T., and W. H. F. Smith, New global marine gravity map/grid based on stacked ERS-1, Geosat, and Topex altimetry, *EOS Trans. AGU*, 75, 321, 1994.

Sandwell, D. T., and W. H. F. Smith, Marine gravity anomaly from Geosat and ERS 1 satellite altimetry, *J. Geophys. Res.*, 102, 10,039–10,054, 1997.

Sandwell, D. T., E. L. Winterer, J. Mammerickx, R. A. Duncan, M. A. Lynch, D. A. Levitt, and C. L. Johnson, Evidence for diffuse extension of the Pacific plate from Pukapuka ridges and cross-grain gravity lineations, *J. Geophys. Res.*, 100, 15,087–15,099, 1995.

Scheirer, D. S., K. C. Macdonald, D. W. Forsyth, and Y. Shen, Abundant seamounts of the Rano Rahi seamount field near the Southern East Pacific Rise, 15°S to 19°S, *Mar. Geophys. Res.*, 18, 13–52, 1996.

Searle, R. C., J. Francheteau, and B. Cornaglia, New observations on mid-plate volcanism and the tectonic history of the pacific plate, Tahiti to Easter Microplate, *Earth Planet. Sci. Lett.*, 131, 293–306, 1995.

Sichoix, L., A. Bonneville, and M. K. McNutt, The seafloor swells and Superswell of French Polynesia, *J. Geophys. Res.*, 103, 27,123–27,133, 1998.

Sleep, N. H., Tapping of magmas from ubiquitous mantle heterogeneities: An alternative to plumes?, *J. Geophys. Res.*, 89, 10,029–10,041, 1984.

Smith, W. H., and D. T. Sandwell, Marine gravity field from declassified Geosat and ERS-1 altimetry, *EOS Trans. AGU*, 76, 156, 1995, fall meeting supplement.

Smith, W. H. F., On the accuracy of digital bathymetry data, *J. Geophys. Res.*, **98**, 9591–9604, 1993.

Smith, W. H. F., and D. T. Sandwell, Global sea floor topography from satellite altimetry and ship depth soundings, *Science*, **277**, 1956–1962, 1997.

Smith, W. H. F., and P. Wessel, Gridding with continuous curvature splines in tension, *Geophysics*, **55**, 293, 1990.

Stoffers, P., R. Botz, and J.-L. Cheminee, Geology of Macdonald Seamount region, Austral Islands: Recent hotspot volcanism in the South Pacific, *Mar. Geophys. Res.*, **11**, 101, 1989.

Tebbens, S. F., and S. C. Cande, Southeast Pacific tectonic evolution from early Oligocene to Present, *J. Geophys. Res.*, **102**, 12,061–12,084, 1997.

ten Brink, U., Volcano spacing and plate rigidity, *Geology*, **19**, 397–400, 1991.

ten Brink, U. S., and T. M. Brocher, Multichannel seismic evidence for a subcrustal complex under Oahu and a model for Hawaiian volcanism, *J. Geophys. Res.*, **92**, 13,687–13,707, 1987.

ten Brink, U. S., and T. M. Brocher, Multichannel seismic evidence for variations in crustal thickness across the Molokai fracture zone, *J. Geophys. Res.*, **93**, 1119–1130, 1988.

Tucholke, B. E., and H. Schouten, Kane Fracture Zone, *Mar. Geophys. Res.*, **10**, 1–39, 1988.

Turcotte, D. L., and G. Schubert, *Geodynamics*, John Wiley & Sons, 1982.

Turcotte, D. L., D. C. McAdoo, and J. G. Caldwell, An elastic-perfectly plastic analysis of the bending of the lithosphere at a trench, *Tectonophysics*, **47**, 193–205, 1978.

Turner, D. L., and R. D. Jarrard, K/Ar dating of the Cook-Austral island chain: A test of the hotspot hypothesis, *J. Volcanol. Geotherm. Res.*, **12**, 187–220, 1982.

Vening Meinesz, F. A., Gravity over the Hawaiian archipelego and over the Madeira area, *Proc. K. Ned. Akad. Wet.*, **44**, 44 pp., 1941.

Vogt, P. R., Volcano spacing, fractures, and thickness of the lithosphere, *Earth Planet. Sci. Lett.*, **21**, 235–252, 1974.

Vogt, P. R., Plate kinematics during the last 20 m.y. and the problem of “present” motions, in *The Western North Atlantic Region*, edited by P. R. Vogt and B. E. Tucholke, vol. M of *The Geology of North America*, pp. 405–425, Geological Society of America, Boulder, Colo., 1986.

Walcott, R. I., Flexure of the lithosphere over the Hawaiian Islands, *Tectonophysics*, 9, 435–446, 1970.

Watts, A. B., and J. R. Cochran, Gravity anomalies and flexure of the lithosphere along the Hawaiian-Emperor seamount chain, *Geophys. J. R. Astron. Soc.*, 38, 119–141, 1974.

Watts, A. B., and U. S. ten Brink, Crustal structure, flexure, and subsidence history of the Hawaiian Islands, *J. Geophys. Res.*, 94, 10,473–10,500, 1989.

Watts, A. B., J. H. Bodine, and N. M. Ribe, Observations of flexure and the geological evolution of the Pacific Ocean basin, *Nature*, 283, 532–537, 1980a.

Watts, A. B., J. H. Bodine, and M. S. Steckler, Observations of flexure and the state of stress in the oceanic lithosphere, *J. Geophys. Res.*, 85, 6369–6376, 1980b.

Wessel, P., Thermal stresses and the bimodal distribution of elastic thickness estimates of the oceanic lithosphere, *J. Geophys. Res.*, 97, 14,177–14,193, 1992.

Wessel, P., A re-examination of the flexural deformation beneath the Hawaiian Islands, *J. Geophys. Res.*, 98, 12,177–12,190, 1993.

Wessel, P., Analytical solutions for 3-D flexural deformation of semi-infinite elastic plates, *Geophys. J.*, 124, 907–918, 1996.

Wessel, P., and W. F. Haxby, Thermal stress, differential subsidence, and flexure at oceanic fracture zones, *J. Geophys. Res.*, 95, 375–391, 1990.

Wessel, P., and L. Kroenke, A geometric technique for relocating hotspots and refining absolute plate motions, *Nature*, 387, 365–369, 1997a.

Wessel, P., and L. W. Kroenke, New evidence of a Late Neogene change in Pacific absolute plate motion, *EOS Trans. AGU 1997 Fall Meeting Suppl.*, 78, F726, 1997b.

Wessel, P., and W. H. F. Smith, Free software helps map and display data, *Eos Trans. AGU*, 72, 445–446, 1991.

Wilson, J. T., A possible origin of the Hawaiian Islands, *Can. J. Phys.*, 41, 863–870, 1963.

Wolfe, C. J., M. K. McNutt, and R. S. Detrick, The Marquesas archipelagic apron: Seismic stratigraphy and implications for volcano growth, mass wasting, and crustal underplating, *J. Geophys. Res.*, 99, 13,591–13,608, 1994.

Zindler, A., H. Staudigel, and R. Batiza, Isotope and trace element geochemistry of young Pacific seamounts: Implications for the scale of mantle heterogeneity, *Earth Planet. Sci. Lett.*, 70, 175–195, 1984.

**Document Library**  
*Distribution List for Technical Report Exchange—November 1998*

University of California, San Diego  
SIO Library 0175C  
9500 Gilman Drive  
La Jolla, CA 92093-0175

Hancock Library of Biology & Oceanography  
Alan Hancock Laboratory  
University of Southern California  
University Park  
Los Angeles, CA 90089-0371

Gifts & Exchanges  
Library  
Bedford Institute of Oceanography  
P.O. Box 1006  
Dartmouth, NS B2Y 4 A2  
CANADA

NOAA/EDIS Miami Library Center  
4301 Rickenbacker Causeway  
Miami, FL 33149

Research Library  
U.S. Army Corps of Engineers  
Waterways Experiment Station  
3909 Halls Ferry Road  
Vicksburg, MS 39180-6199

Institute of Geophysics  
University of Hawaii  
Library Room 252  
2525 Correa Road  
Honolulu, HI 96822

Marine Resources Information Center  
Building E38-320  
MIT  
Cambridge, MA 02139

Library  
Lamont-Doherty Geological Observatory  
Columbia University  
Palisades, NY 10964

Library  
Serials Department  
Oregon State University  
Corvallis, OR 97331

Pell Marine Science Library  
University of Rhode Island  
Narragansett Bay Campus  
Narragansett, RI 02882

Working Collection  
Texas A&M University  
Dept. of Oceanography  
College Station, TX 77843

Fisheries-Oceanography Library  
151 Oceanography Teaching Bldg.  
University of Washington  
Seattle, WA 98195

Library  
R.S.M.A.S.  
University of Miami  
4600 Rickenbacker Causeway  
Miami, FL 33149

Maury Oceanographic Library  
Naval Oceanographic Office  
Building 1003 South  
1002 Balch Blvd.  
Stennis Space Center, MS 39522-5001

Library  
Institute of Ocean Sciences  
P.O. Box 6000  
Sidney, B.C. V8L 4B2  
CANADA

National Oceanographic Library  
Southampton Oceanography Centre  
European Way  
Southampton SO14 3ZH  
UK

The Librarian  
CSIRO Marine Laboratories  
G.P.O. Box 1538  
Hobart, Tasmania  
AUSTRALIA 7001

Library  
Proudman Oceanographic Laboratory  
Bidston Observatory  
Birkenhead  
Merseyside L43 7 RA  
UK

IFREMER  
Centre de Brest  
Service Documentation-Publications  
BP 70 29280 PLOUZANE  
FRANCE

<b>REPORT DOCUMENTATION PAGE</b>		<b>1. REPORT NO.</b> MIT/WHOI 99-01	<b>2.</b>	<b>3. Recipient's Accession No.</b>
<b>4. Title and Subtitle</b> Tectonic Evolution and Midplate Volcanism in the South Pacific		<b>5. Report Date</b> February 1999		
		<b>6.</b>		
<b>7. Author(s)</b> Kelsey Allyn Jordahl		<b>8. Performing Organization Rept. No.</b>		
<b>9. Performing Organization Name and Address</b> MIT/WHOI Joint Program in Oceanography/Applied Ocean Science & Engineering		<b>10. Project/Task/Work Unit No.</b> MIT/WHOI 99-01		
		<b>11. Contract(C) or Grant(G) No.</b> (C) OCE-9012949 (G) OCE-9012529 (G) OCE-9415930		
<b>12. Sponsoring Organization Name and Address</b> National Science Foundation Massachusetts Institute of Technology		<b>13. Type of Report &amp; Period Covered</b> Ph.D. Thesis		
		<b>14.</b>		
<b>15. Supplementary Notes</b> This thesis should be cited as: Kelsey Allyn Jordahl, 1999. Tectonic Evolution and Midplate Volcanism in the South Pacific. Ph.D. Thesis. MIT/WHOI, 99-01.				
<b>16. Abstract (Limit: 200 words)</b> Changes in morphology of the Marquesas Fracture Zone are correlated with small changes in Pacific-Farallon relative motion. The simple flexural signal of a locked fracture zone may be obscured by tectonic effects, and there is no evidence for the release of shear stress on the fracture zone by vertical slip after leaving the active transform. One such small change in plate motion is documented in the Southern Austral Island region of the South Pacific. A twelve degree clockwise change in Pacific-Farallon relative motion occurred around fifty million years ago. This Eocene change in spreading direction and rate is locally constrained with observations of magnetic anomalies and spreading fabric orientation. At the southeastern end of the Cook-Austral Island chain, multiple episodes of volcanism have left a diverse population of seamounts. Volume estimates from geophysical data and modeling show that one-half to two-thirds of the volcanic material is over thirty million years old, while the remainder is less than five million years old. Seismic and bathymetric data imply the presence of abyssal basalt flows in the flexural moat of the Austral Islands, probably associated with Austral Islands volcanism, which may contribute a significant amount of material to the archipelagic apron.				
<b>17. Document Analysis</b> <b>a. Descriptors</b> tectonics volcanism flexure				
<b>b. Identifiers/Open-Ended Terms</b>				
<b>c. COSATI Field/Group</b>				
<b>18. Availability Statement</b> Approved for publication; distribution unlimited.		<b>19. Security Class (This Report)</b> UNCLASSIFIED	<b>21. No. of Pages</b> 139	
		<b>20. Security Class (This Page)</b>	<b>22. Price</b>	